MECHANICS OF MOLECULAR BOND CLUSTERS BETWEEN ELASTIC MEDIA: STOCHASTIC-ELASTIC COUPLING IN CELL-MATRIX ADHESION

BY

JIN QIAN

B.E., PEKING UNIVERSITY, 2000

M.S., CHINESE ACADEMY OF SCIENCES, 2003

SC.M., BROWN UNIVERSITY, 2009

A DISSERTATION SUBMITTED IN PARTIAL FULFILLMENT OF THE REQUIREMENTS FOR THE DEGREE OF DOCTOR OF PHILOSOPHY IN THE DIVISION OF ENGINEERING AT BROWN UNIVERSITY

PROVIDENCE, RHODE ISLAND

MAY 2010

This dissertation by Jin Qian is accepted in its present form

by the Division of Engineering as satisfying the

dissertation requirement for the degree of Doctor of Philosophy.

Date_____ _____

Huajian Gao, Advisor

Recommended to the Graduate Council

Date_____ _____

Lambert B. Freund, Reader

Date_____ _____

Christian Franck, Reader

Approved by the Graduate Council

Date_____ _____

Sheila Bonde, Dean of the Graduate School

Vita

Jin Qian was born in Jiangxi province of China on October 30, 1978. He received his B.E. degree from Peking University in 2000, and his M.S. degree from Institute of Mechanics, Chinese Academy of Sciences in 2003. He entered the solid mechanics group at Brown University for pursuing Ph.D. degree in March 2006. While at Brown he obtained an Sc.M. degree in Applied Mathematics in May 2009.

Acknowledgements

First and foremost, I would like to thank my advisor, Prof. Huajian Gao, for accepting me as his doctoral student and offering me the opportunity to work on some of the most interesting problems in biomechanics. All of the work in this thesis has been a very pleasant collaboration with him. I thank him for the support, guidance and patience throughout my Ph.D. study, which helped to make this learning experience the one I will always remember.

I am grateful to the members of the thesis committee, Prof. Freund and Prof. Franck, for their insightful comments and valuable suggestions making significant improvement to the work. Part of my research has benefited a lot from useful conversations and enjoyable collaborations with many post-docs and students during my stay at Brown. They are too numerous to list. Also, I would like to thank the faculty of Brown Solid Mechanics for providing high-quality courses that contributed to my education.

I want to express my deepest appreciation to my family, particularly to my wife Ling. This thesis could not have been completed without their constant encouragement and support.

Contents

List of Tables

List of Figures

Chapter 1

Introduction

1.1 Overview of cell-matrix adhesion

Most biological cells must adhere to other cells or extracellular matrix (ECM, also termed as “substrate”) in performing normal physiological functions such as migration, spreading, differentiation, growth and healing [1]. The feature that distinguishes cell adhesion from the adhesive contact in engineering systems is the specific binding between cell surface proteins (receptors) and complementary molecules (ligands) on other cells or substrates. The specific receptor-ligand recognition is often considered a lock-and-key mechanism, while the various non-specific interactions including electrostatic, van der Waals, etc. are usually negligible due to a layer of polymer brush surrounding cell surface called glycocalyx [2]. There are literally hundreds of receptors that participate in cell adhesion, which are grouped in several main families: integrin, immunoglobulin, selectin and cadherin. Each of these families is accompanied by an equally diverse family of ligands [3].

An early theory for describing cell adhesion was established by Bell in a thermodynamic framework [4]. The process of adhesion or de-adhesion of cells from

substrates was subsequently modeled via peeling tests that are familiar in engineering design but is made more complicated by the biological interface and geometry involved [5,6]. More recent progresses have been made in modeling curved biological membranes spreading on a flat substrate mediated by binder diffusion [7,8], as well as receptor-mediated cellular uptake and release of viruses or nanoparticles [9].

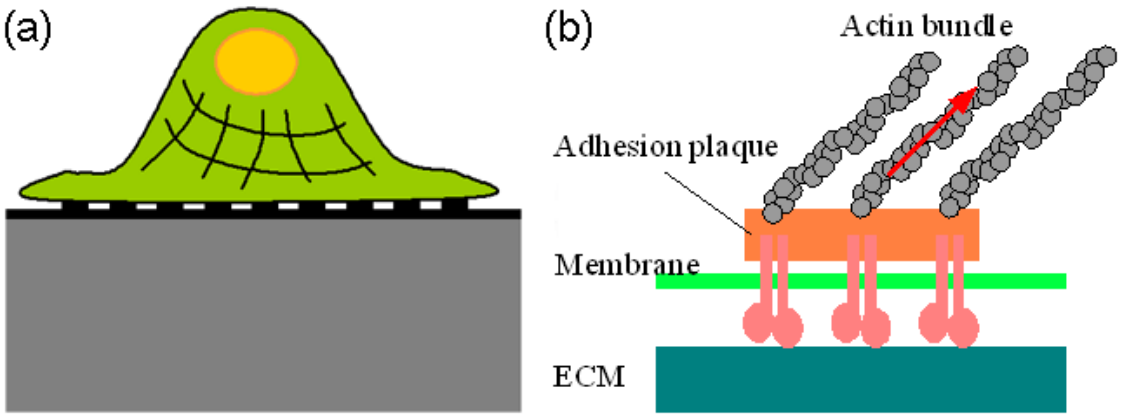

Figure 1.1: Schematic representation of focal contacts in cell-ECM adhesion based on specific binding between receptors and complementary ligands. (a) Cell-ECM adhesion localized to discrete focal contacts. (b) Actin bundles anchored into an adhesion plaque that connects ECM through molecular bonds.

Interestingly, experiments [10] have revealed that cell-matrix adhesion is often localized to discrete contact regions called focal adhesions (FAs) that consist of multiple transmembrane receptor-ligand bonds connecting the actin cytoskeleton of cell to ECM, as schematically represented in Figure 1.1. Focal adhesions are usually micron-sized dense clusters of molecular bonds linked to a complex assembly of a variety of associated proteins called an adhesion plaque. Also, FAs are constantly exposed to mechanical stress induced by different physical interactions such as those due to blood flow or other external environments, as well as those generated by cell's own contractile machinery.

These forces act at the interface between cell and ECM, and are known to exert significant influences on cell shape, cytoskeleton organization and intracellular processes. It is therefore interesting to study the collective behavior of a cluster of receptor-ligand bonds under mechanical forces.

A single molecular bond in cell adhesion has a binding energy of only 10-25 k_BT [11], which leads to a finite lifetime due to thermally activated bond dissociation even in the absence of an external force. In the past two decades, intensive studies, including the experiments based on dynamic force spectroscopy [12-14] and the theoretical work by Evans and Ritchie [15], and more recently by Freund [16], have been carried out to understand the behavior of single molecular bonds under an applied force. The process of bond dissociation is regarded as thermally assisted escape over a potential energy barrier [17,18]. Application of an external force changes the energy landscape and therefore influences the rupture process. For time-independent loading, both theories and experiments [12-18] have indicated that the average survival time of a single molecular bond decreases exponentially with increasing force, irrespective of the specific types of molecular bonds.

Although such a statistical description of single molecular bonds is by now well accepted, the collective behavior of multiple molecular bonds, such as those in focal adhesions, can be much more complex and less understood. A single molecular bond only has a limited lifetime while a cluster of bonds can survive for much longer time due to the cooperative effects in a stochastic ensemble. How can this transition be modeled and can this tell us something about the mechanics of cell adhesion? The pioneering theoretical effort to address this question was performed by Bell [4] who applied the

kinetic theory of chemical reactions to predict the thermodynamic competition between bond breaking and reforming. Subsequently, Seifert [19] studied the dynamic behavior of a molecular bond cluster subjected to ramping forces. Erdmann and Schwarz [20,21] developed a more rigorous theory of cluster lifetime based on the one-step master equation in stochastic dynamics.

A common assumption of the existing models on cluster adhesion is “equal load sharing”, which means that the applied load is equally shared among all closed bonds. Based on this assumption, the deterministic equation of Bell’s framework predicts that molecular clusters remain stable and have infinite lifetime up to a critical load [4]; the theory of Erdmann and Schwarz indicates that the cluster lifetime is always finite and it monotonically increases as the cluster size grows: the larger the cluster, the more stable it is [20,21]. In contrast, experimental observations have shown in general that FAs cannot grow unboundedly and are usually subjected to a size limit up to a few microns [22,23], and recent analysis by Lin and Freund shows an optimum cluster size for maximum adhesion strength based on an analogy between focal adhesions and periodic cracks [24]. Also, the elastic properties of cell and substrate were found to play an essential role in FA growth and maintenance. Stable FAs only form on sufficiently rigid substrates, and cells tend to migrate toward stiffer region when cultured on an elastically nonhomogeneous substrate [25,26]. In addition, the elastic modulus of cytoskeleton can change over several orders of magnitude in response to different levels of myosin-II-driven contractility [27-29], while inhibition of the contractile stress leads to dissolution of cytoskeleton and disappearance of FAs [30]. When myosin II activity is suppressed, application of an external force, irrespective of its physical origin, is found to stimulate

growth of FAs in the direction of the force [31]. Experiments have also shown that the size of mature FAs can reversibly increase or decrease in response to the magnitude of applied force, with force per unit area (stress) maintained near a constant value around 5.5 KPa irrespective of the cell type [32,33].

Why is there a micron-scale size limit on FAs? Why do cells prefer rigid substrates? Why is cell stiffness due to cytoskeletal contractility necessary to stabilize FAs? Can we model the lifetime and strength of FAs taking cell/ECM elasticity into account? Motivated by the existing experimental observations and seemingly complex interplay between adhesion size, cell/ECM stiffness and receptor-ligand rupture/rebinding, in this thesis we build upon the previous framework of Bell [4] and its recent extension by Erdmann and Schwarz [20,21] to develop a coupled stochastic-elasticity model that aims to seamlessly unify stochastic descriptions of individual molecular bonds and elastic descriptions of interfacial adhesion. To avoid complications of modeling at this stage, we consider an idealized theoretical model involving clusters of molecular bonds between two semi-infinite elastic media under a tensile load. Of special interest is how the distributed interfacial traction governed by the system elasticity influences the cluster lifetime and strength. The approach here can be extended to a broad range of situations involving spatially dependent bond traction and/or nonhomogeous bond density. For example, when leukocytes tether to and roll on vessel walls under blood flow, the molecular bonds near the periphery of the contact region are expected to be more stretched than those at the center [34,35]. In cell-cell adhesion, the formation of an immunological synapse involves multiple types of receptor-ligand bonds with different rest lengths, and the adhesion complex is often organized into patterns with spatially

varying bond density [36,37]. The current approach could serve as a basis for further study of such problems.

1.2 Organization of this thesis

The remainder of this work is organized as follows. In Chapter 2, we first present stochastic models for rupture and rebinding of single molecular bonds. The master equation for the temporal evolution of a cluster of parallel adhesion bonds is discussed under the assumption of equal load sharing. In Chapter 3, we derive a fundamental scaling law which controls the interfacial traction distribution based on the elastic equations of classical contact mechanics. We demonstrate that, depending on the adhesion size and the relative stiffness of the surrounding elastic media with respect to the adhesion cluster, there is a transition between uniform and crack-like singular distributions of interfacial traction. Recognizing the discrete configuration of molecular bonds and the effects of stochastic bond breaking/reforming, we then adopt a discrete elastic Green's function approach to solve the interfacial adhesion problem. In Chapter 4, the stochastic descriptions of molecular reactions and the elastic descriptions of bond force and surface separation are coupled through a Monte Carlo scheme based on Gillespie's algorithm. The stochastic dynamics of cluster evolution is described according to spatially dependent rupture and rebinding rates, with each bond (closed or open) considered as an independent reaction site. A series of Monte Carlo simulations are performed to investigate the effects of cluster size, cell/ECM modulus, rebinding rate, as well as loading direction on the cluster lifetime and strength for a single adhesion patch and periodic adhesion clusters in Chapters 5 and 6, respectively. Receptor diffusion is

then considered in the simulations on tension-induced clustering of molecular bonds and growth of focal adhesions. Chapter 7 of this thesis discusses a scaling law associated with the capillary adhesion in insects like beetles and blowflies. We show that size reduction down to a critical value results in optimization of the adhesion strength. The most important results of this thesis are briefly summarized and an outlook to possible future research is provided in the final chapter.

Chapter 2

Stochastic model of molecular bonds

Unlike the conventional concept of nonspecific adhesion between elastic bodies, the specific molecular bonds between receptors and ligands behave more like chemical reactions and they can transit stochastically between a "closed" (binding) state and an "open" (broken) state.

2.1 Force-dependent rupture of a closed bond

A single closed receptor-ligand bond can undergo a transition from the original closed state to an open state, as shown in Figure 2.1. According to Kramer's theory [38], the process can be viewed as a thermally activated escape over a transition state barrier. The rate of spontaneous dissociation in the absence of applied force can be expressed as

$$k_0 = \frac{1}{\tau_0}\exp\left(-\frac{E_b}{k_B T}\right), \tag{2.1}$$

where τ_0 is the attempt time, E_b is the height of the energy barrier and $k_B T \approx 4.1\,\mathrm{pN\cdot nm}$ is the thermal energy at physiological temperature. For non-covalent molecular bonds in

cell-matrix adhesion, τ_0 is on the order of nanoseconds and E_b is around 10-25 k_BT [11]. According to the seminal model of Bell [4], when a static force F_0 is applied, the energy barrier is modified to $E_b - F_0 x_b$, where x_b is the distance between the minimum of binding potential and the transition state barrier. The rupture rate then becomes

$$k_{\text{off}} = \frac{1}{\tau_0}\exp\left(-\frac{E_b - F_0 x_b}{k_B T}\right) = k_0 \exp\left(\frac{F_0}{F_b}\right), \tag{2.2}$$

where k_0 is the spontaneous dissociation rate in the absence of an applied load. For molecular bonds in focal adhesions, $1/k_0$ falls in the range from a fraction of a second to around 100 seconds [18]. $F_b = k_B T / x_b$ is an intrinsic force scale. With a typical value $x_b = 1\,\text{nm}$, we estimate that $F_b \approx 4\,\text{pN}$.

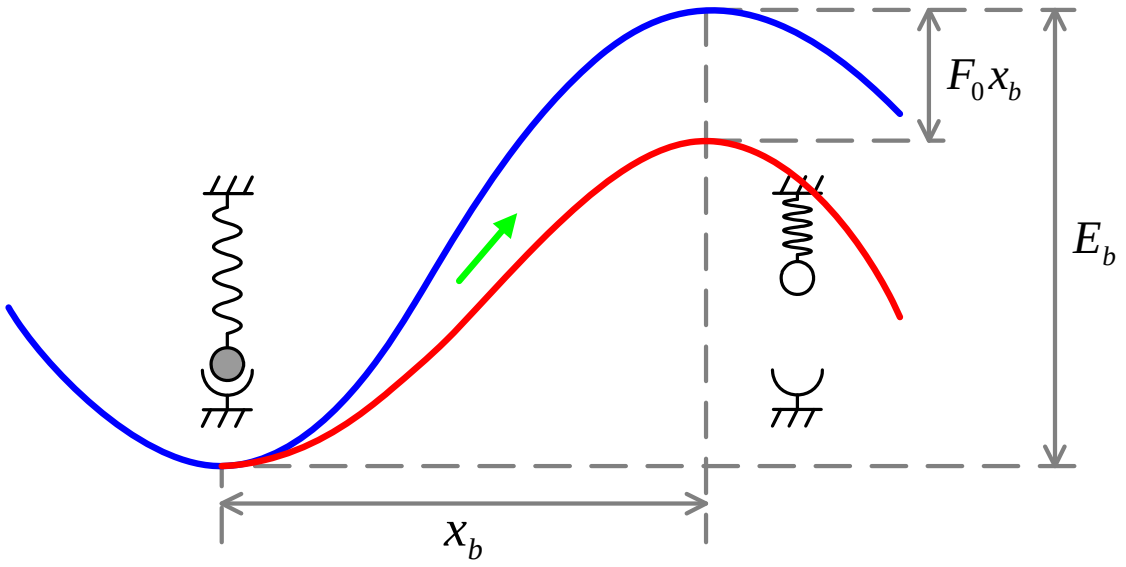

Figure 2.1: Schematic representation of the energy landscape for receptor-ligand interaction. The "closed" (binding) state to the left is separated by a transition state barrier from the "open" (broken) state. The transition state barrier is characterized by the height E_b and the separation x_b to the closed state. An applied force tends to tilt the energy landscape, resulting in a lower barrier.

The dimensionless lifetime $T = k_0 t$, where t is the real time, of a single closed bond is therefore

$$T(1) = \exp\left(-\frac{F_0}{F_b}\right), \tag{2.3}$$

which is plotted as a function of an applied force in Figure 2.2. The open circles in the figure are the Monte Carlo simulation results based on the numerical scheme described in Chapter 4. A single molecular bond is unstable over long term even without an applied force.

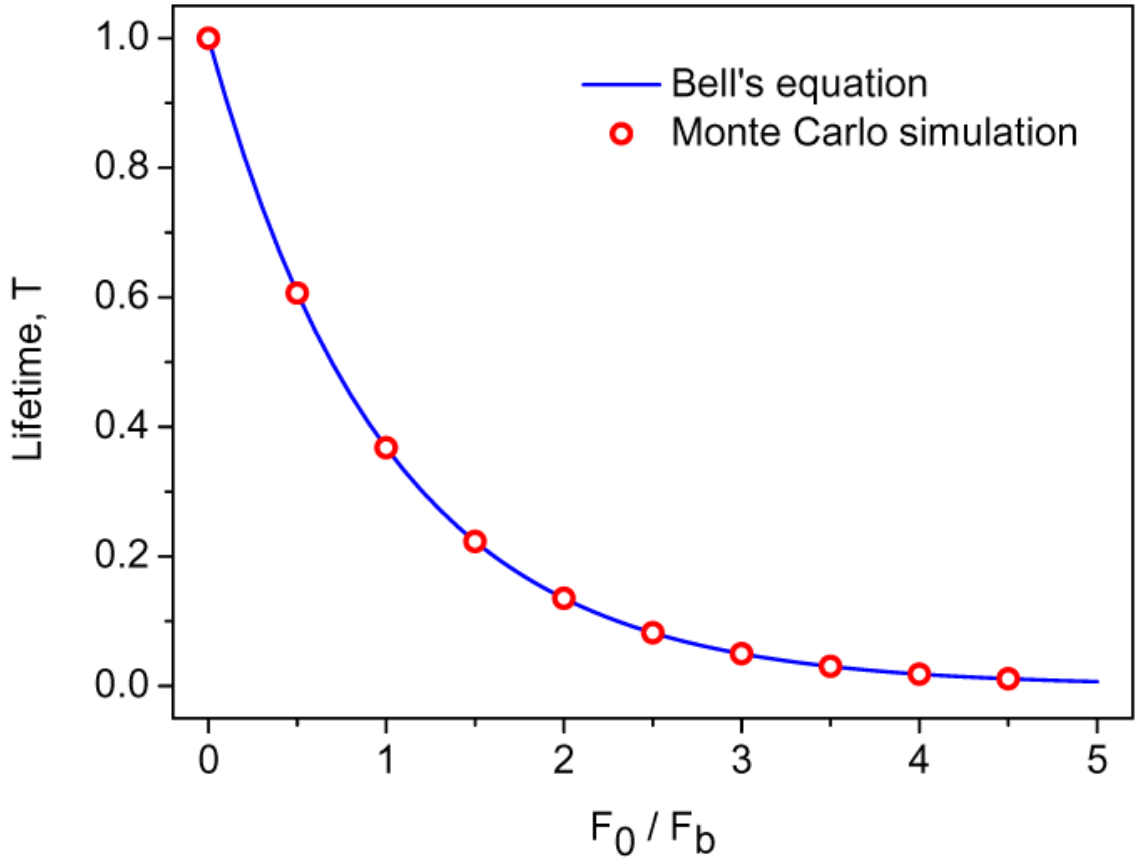

Figure 2.2: Survival time ($T = k_0 t$) of a single molecular bond as a function of an applied force F_0/F_b. The open circles are the Monte Carlo simulation results based on Gillespie's algorithm (described in Chapter 4).

2.2 Separation-dependent rebinding of an open bond

Rebinding of an open bond can occur as long as the broken receptor and ligand pairs are held in proximity for sufficient amount of time. In modeling bond association, the whole process is regarded as consisting of two steps: firstly, the receptor and complementary ligand have to come sufficiently close within a binding radius l_{bind} to form a complex; secondly, the complex reacts at a rate k_{on}^{0} to form the final receptor-ligand bond [39-41].

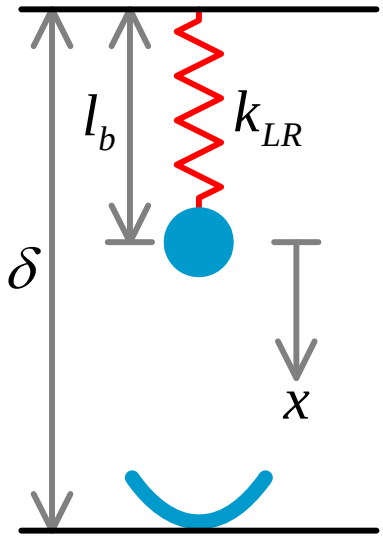

Figure 2.3: A tethered receptor approaching and reacting with a ligand. The two surfaces are separated by a distance δ. The receptor is modeled as a binding site tethered to cell by a linear spring with stiffness k_{LR} and rest length l_b.

In a simplified 1D model, the rebinding reaction of an open receptor-ligand bond is viewed as a receptor molecule with sticky end approaching and reacting with an opposing ligand, as schematically shown in Figure 2.3. The ligand is fixed on a substrate surface and the receptor is modeled as a binding site tethered to the cell surface by a linear spring

with stiffness k_{LR} and rest length l_b. Suppose that the separation between the two surfaces is δ. The energy of an arbitrary state with spring deformation x is

$$U(x)=\frac{1}{2}k_{LR}x^2,\ -l_b \le x \le \delta - l_b. \tag{2.4}$$

According to Maxwell-Boltzmann distribution, the position of the sticky end of the receptor should obey the following probability density function

$$P(x)=\frac{1}{Z}\exp\left(-\frac{k_{LR}x^2}{2k_BT}\right), \tag{2.5}$$

where Z is the partition function of the receptor confined in a harmonic potential between $-l_b$ and $\delta - l_b$. Z has to satisfy the normalization condition

$$\int_{-l_b}^{\delta-l_b} P(x)\mathrm{d}x = 1, \tag{2.6}$$

which leads to

$$Z=\sqrt{\frac{\pi k_BT}{2k_{LR}}}\cdot\left(\mathrm{erf}\left((\delta-l_b)\sqrt{\frac{k_{LR}}{2k_BT}}\right)+\mathrm{erf}\left(l_b\sqrt{\frac{k_{LR}}{2k_BT}}\right)\right). \tag{2.7}$$

Here $\mathrm{erf}(\cdot)$ is the error function.

The probability of forming a receptor-ligand complex is that the binding site falls within the reaction range $\delta - l_b - l_{\mathrm{bind}} \le x \le \delta - l_b$, which can be approximated as $P(\delta - l_b)\cdot l_{\mathrm{bind}}$. Thus, the association rate k_{on} between a ligand site on the substrate surface and a receptor tethered to the cell surface is dependent on the cell-substrate separation δ as [39-41]

$$k_{\mathrm{on}}=k_{\mathrm{on}}^0\frac{l_{\mathrm{bind}}}{Z}\exp\left(-\frac{k_{LR}(\delta-l_b)^2}{2k_BT}\right). \tag{2.8}$$

In dimensionless form, the dissociation and association rates in Equations (2.2) and (2.8) can be rewritten in

$$r = k_{\text{off}}/k_0 = \exp\left(F_0/F_b\right), \tag{2.9a}$$

$$g = k_{\text{on}}/k_0 = 2\gamma\sqrt{\frac{\beta}{\pi}}\frac{\exp\left(-\beta(\Delta - L_b)^2\right)}{\text{erf}\left((\Delta - L_b)\sqrt{\beta}\right) + \text{erf}\left(L_b\sqrt{\beta}\right)}, \tag{2.9b}$$

where $\beta = k_{LR}b^2/(2k_BT)$ and $\gamma = \left(k_{\text{on}}^0/k_0\right)\left(l_{\text{bind}}/b\right)$ is a prefactor for rebinding rate. $\Delta = \delta/b$ and $L_b = l_b/b$ are the surface separation and bond rest length after normalization. Here we have chosen the bond spacing b as the basic length scale for normalization purpose.

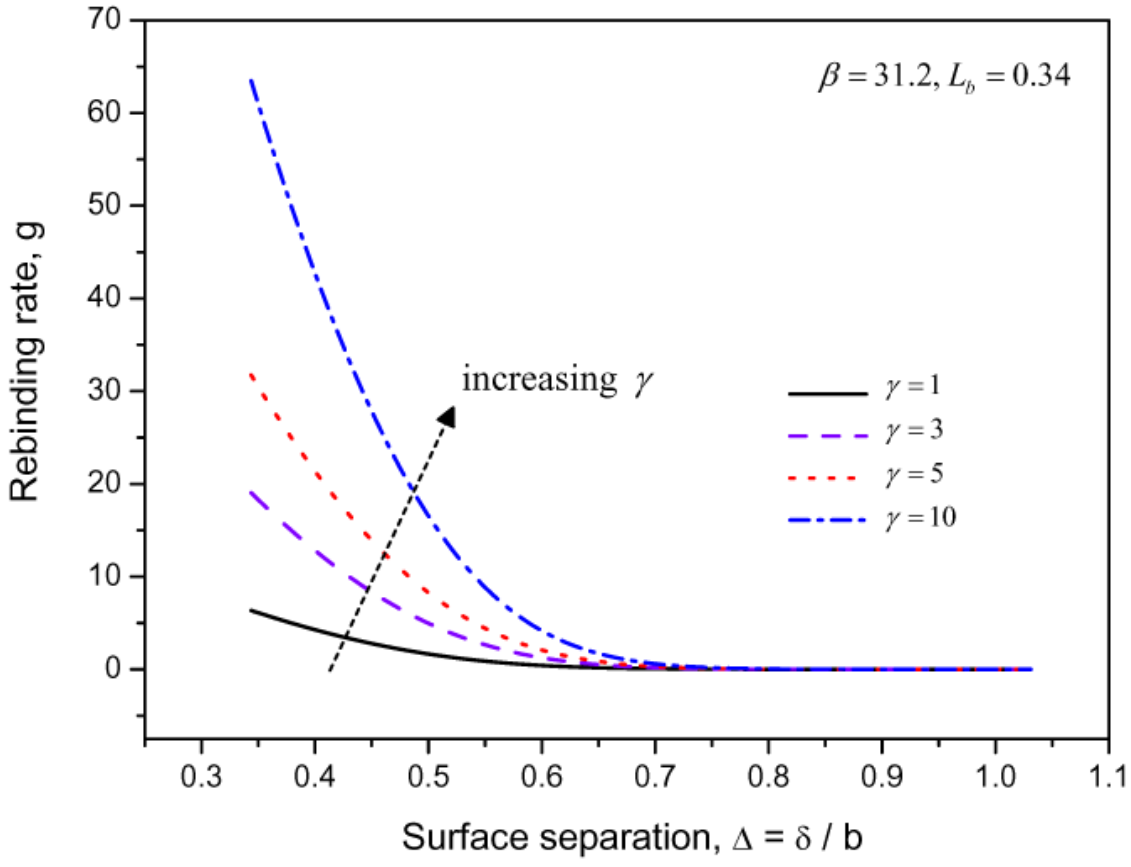

Figure 2.4: The rebinding rate g of an open molecular bond anchored on two surfaces as a function of the surface separation Δ.

Note that the rebinding rate described above depends strongly on the surface separation. The dimensionless parameters $\beta = 31.2$ and $L_b = 0.34$ are estimated from typical values of the relevant parameters: $k_{LR} = 0.25\,\mathrm{pN/nm}$, $b = 32\,\mathrm{nm}$, $l_b = 11\,\mathrm{nm}$. Figure 2.4 plots the rebinding rate g for different values of γ as the normalized surface separation Δ varies between 1 and 3. Interestingly, for the range of γ under consideration, we see that g decays in a similar manner and it becomes nearly zero when the opposing surfaces are separated beyond about two times of the bond rest length. This means that the chance of rebinding is very low once the surface separation exceeds $2l_b$. We expect that this strongly decaying behavior of rebinding rate will play a very important role in the stability of molecular bond clusters when the elasticity of the system is considered. As an example of an adhesion cluster under remote tensile force, the surface separation is generally larger at the cluster edges than at the center and, consequently, rebinding is less likely to occur at the edges. Once the opposing surfaces are separated by more than a critical distance (about $2l_b$ at our prescribed parameters), rebinding becomes impossible and the cluster is expected to undergo a crack-like failure from its adhesion edges.

2.3 A cluster of molecular bonds: mean field theory

Erdmann and Schwarz [20,21] considered the case that a pulling force F is applied on a molecular cluster consisting of a total number N_t of receptor-ligand bonds which undergo stochastic rupture and rebinding, as shown in Figure 2.5. Suppose that k bonds

are closed and $(N_t - k)$ bonds are open at a time t ($0 \le k \le N_t$). The applied force is assumed to be equally shared among the k closed bonds. It is convenient to use the dimensionless time $\tau = k_0 t$ and the dimensionless force $f = F/F_b$. According to Equation (2.9a), a closed bond bears a force f/k and will rupture at the rate $e^{f/k}$. On the other hand, Erdmann and Schwarz [20,21] assumed that the $(N_t - k)$ open bonds would rebind individually at a separation-independent rate γ.

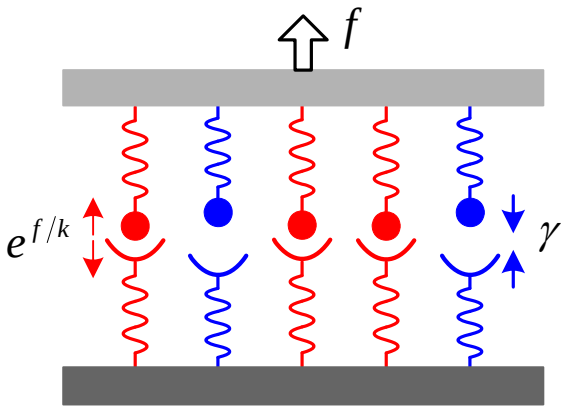

Figure 2.5: A cluster of molecular bonds under a constant applied force, investigated by Erdmann and Schwarz [20,21]. There are N_t receptor-ligand bonds, k of which are closed and share the applied force f equally. A closed bond ruptures at the rate $e^{f/k}$, and an open bond rebinds at a constant rate γ independent of surface separation.

In such a setting, the dynamics of the cluster evolution can be described by a one-step master equation as follows [42]:

$$\frac{dp_k}{d\tau} = r_{k+1} p_{k+1} + g_{k-1} p_{k-1} - (r_k + g_k) p_k , \tag{2.10}$$

where p_k is the probability that there exists k closed bonds at time τ, r_k is the reverse rate of transition from k to $k-1$ closed bonds, and g_k is the forward rate of transition from k to $k+1$ closed bonds. The reverse and forward rates between the different states

are

$$r_k = k\exp(f/k),\ g_k = (N_t - k)\cdot\gamma\,. \tag{2.11}$$

From Equation (2.11), $g_{N_t} = 0$ implies that bond rebinding is impossible when $k = N_t$, which naturally sets the upper boundary of the number of closed bond k. In the terminology of stochastic processes, $k = N_t$ is called a "reflecting" boundary. Because bond breaking is impossible when $k = 0$, one should artificially let $r_0 = 0$. Moreover, $k = 0$ is the failure state of adhesion, therefore $g_0 = 0$ should be set to form an "absorbing" boundary.

The master equation is fairly easy to write. However, solving it is quite difficult except for very few simple cases. In the mean field theory considered by Erdmann and Schwarz [21], the quantities of great interest are the mean and variance of the number of closed bonds, which are calculated to be

$$N(\tau) = \langle k\rangle = \sum_{k=1}^{N_t} k\cdot p_k(\tau), \tag{2.12a}$$

$$V(\tau) = \left\langle (k-N)^2\right\rangle = \sum_{k=1}^{N_t} k^2\cdot p_k(\tau) - N^2\,. \tag{2.12b}$$

Substituting Equation (2.12a) into the master equation leads to

$$\frac{\mathrm{d}N}{\mathrm{d}\tau} = \sum_{k=1}^{N_t} k\cdot\frac{\mathrm{d}p_k}{\mathrm{d}\tau} = -\langle r_k\rangle + \langle g_k\rangle - (1+N_t)g_{N_t}p_{N_t} + r_0 p_0\,. \tag{2.13}$$

One should let $g_{N_t} = r_0 = 0$, which means no rebinding when all bonds are closed and no rupture when all bonds are open. Thus

$$\frac{\mathrm{d}N}{\mathrm{d}\tau} = -\langle r_k \rangle + \langle g_k \rangle . \tag{2.14}$$

Similarly, the evolution of the variance V can be calculated as

$$\frac{\mathrm{d}V}{\mathrm{d}\tau} = \langle 2(k-N)(g_k - r_k) \rangle + \langle g_k + r_k \rangle . \tag{2.15}$$

In the case considered by Erdmann and Schwarz, the rebinding rate is a constant γ independent of the surface separation so that the forward rate g_k is a linear function of k and

$$\langle g_k \rangle = (N_t - N)\cdot\gamma . \tag{2.16}$$

However, the reverse rate r_k is nonlinear in k and its average in Equations (2.14) and (2.15) cannot be taken. As an approximate treatment, Erdmann and Schwarz expanded r_k in a Taylor series to the second order around N. The average of r_k is then

$$\langle r_k \rangle \approx Ne^{f/N} + Ve^{f/N} f^2 / 2N^3 , \tag{2.17}$$

which leads to the following ordinary differential equations in N and V as follows [21]:

$$\frac{\mathrm{d}N}{\mathrm{d}\tau} = -Ne^{f/N} - Ve^{f/N}\frac{f^2}{2N^3} + \gamma(N_t - N), \tag{2.18a}$$

$$\frac{\mathrm{d}V}{\mathrm{d}\tau} = Ne^{f/N} + \gamma(N_t - N) - V\left[e^{f/N}\left(2 - 2\frac{f}{N} - \frac{f^2}{2N^3}\right) + 2\gamma\right]. \tag{2.18b}$$

The initial condition is set that all bonds are closed at $\tau = 0$, i.e.

$$N(0) = N_t ,\ V(0) = 0 . \tag{2.19}$$

The equations can be solved by numerical integration for given N_t, f and γ.

For the simplest version of the mean field theory, the variance V is neglected. Letting

$V = 0$ in Equation (2.18), one obtain

$$\frac{\mathrm{d}N}{\mathrm{d}\tau} = -Ne^{f/N} + \gamma\left(N_t - N\right),\ N(0) = N_t, \tag{2.20}$$

which is just Bell's equation to model cell adhesion [4]. In this framework, a molecular bond cluster remains stable up to a critical force

$$f_{cr} = N_t \,\mathrm{plog}\left(\frac{\gamma}{e}\right), \tag{2.21}$$

where the product logarithm $\mathrm{plog}(a)$ is defined as the solution x to the equation $xe^x = a$. For $f > f_{cr}$, the cluster is unstable, while for $f < f_{cr}$, the cluster survives for infinitely long time.

2.4 Lifetime of a molecular bond cluster under equal load sharing

Experiments have shown that the size of mature focal contacts in cell-matrix adhesion can reversibly increase or decrease in response to the applied force, with force per unit area maintained near a constant value [32,33]. In this sense, it will be instructive to study the behavior of molecular bond clusters subjected to a constant average force per bond, i.e. a force proportional to cluster size. Consider the case that a pulling force $f \cdot N_t$ is applied on a molecular cluster consisting of a total number N_t of receptor-ligand bonds, as indicated in Figure 2.6. The nominal force sustained by individual bonds is f. Again, suppose that k bonds are closed and $\left(N_t - k\right)$ bonds are open at a time τ $(0 \le k \le N_t)$, and the k closed bonds share the total applied force equally. The actual force acting on each closed bond is $f \cdot N_t / k$, and each of the $\left(N_t - k\right)$ open bonds is assumed to rebind

at a separation-dependent rate g described in Equation (2.9b).

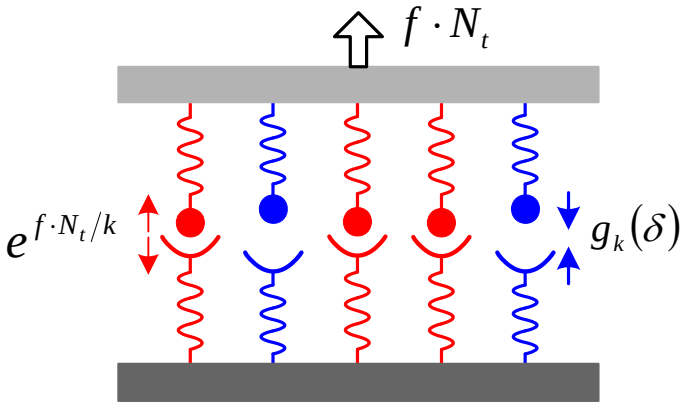

Figure 2.6: A cluster of molecular bonds subjected to a force proportional to its size. There are N_t receptor-ligand bonds, k of which are closed and share the load $f \cdot N_t$ equally. The $N_t - k$ open bonds rebind at a separation–dependent rate g described in Equation (2.9b).

For initial condition $k(0) = N_t$, the average lifetime of a molecular bond cluster, defined as the mean first passage time reaching the failure state $k = 0$, can be calculated analytically by [43]

$$T(N_t) = \sum_{k=1}^{N_t} \frac{1}{r_k} + \sum_{i=1}^{N_t - 1} \sum_{j=i+1}^{N_t} \frac{\prod_{k=j-i}^{j-1} g_k}{\prod_{k=j-i}^{j} r_k} \tag{2.22}$$

for the reflecting boundary condition at $k = N_t$ and absorbing boundary condition at $k = 0$. The idea here is to sum the average time for all possible pathways transiting from the initial cluster size N_t towards the absorbing boundary $k = 0$ with their statistical weights. Under the present setting,

$$r_k = k \exp(f N_t / k), \tag{2.23a}$$

$$g_k = (N_t - k) \cdot 2\gamma \sqrt{\frac{\beta}{\pi}} \frac{\exp\left(-\beta(\Delta - L_b)^2\right)}{\operatorname{erf}\left((\Delta - L_b)\sqrt{\beta}\right) + \operatorname{erf}\left(L_b \sqrt{\beta}\right)}. \tag{2.23b}$$

The surface separation Δ in Equation (2.23b) is also a function of k as

$$\Delta = L_b + \frac{f \cdot N_t}{k} \frac{F_b}{k_{LR} b}. \tag{2.24}$$

If $N_t = 1$, Equation (2.22) reduces to

$$T(1) = e^{-f}, \tag{2.25}$$

which is the lifetime of single molecular bonds. In the case of zero rebinding, the second term of Equation (2.22) vanishes and the lifetime becomes

$$T(N_t) = \sum_{k=1}^{N_t} \frac{1}{r_k}, \tag{2.26}$$

which, in the absence of an applied force, is further reduced to

$$T(N_t) = \sum_{k=1}^{N_t} \frac{1}{k}, \tag{2.27}$$

which is the N_t-th harmonic number.

For typical values: $k_{LR} = 0.25\,\mathrm{pN/nm}$, $b = 32\,\mathrm{nm}$, $l_b = 11\,\mathrm{nm}$, $F_b = 4\,\mathrm{pN}$, we plot the lifetime T of a molecular bond cluster as a function of its size for various load levels. The rebinding prefacer, γ, is taken to be 100 in Figure 2.7a, 10 in 2.7b and 1.0 in 2.7c. We observe that a single bond is always unstable, and bond clustering prolongs the lifetime by orders of magnitude through the rebinding mechanism. Each molecular bond is very weak but collectively many bonds together result in long term stability. Moreover, the lifetime T increases monotonically with growing cluster size N_t under the assumption of equal load sharing, which is similar to the results of Erdmann and Schwarz based on the separation-independent rebinding rate [20,21].

We note that, in the presence of elastic deformation of cell and ECM, the reverse and forward rates in Equation (2.9) would also depend on the local force and surface

separation at a bond location within the adhesion domain. It can be shown that any spatial variation of force and separation distributions from uniformity would increase the total rupture rate and decrease the rebinding probability, thereby causing the cluster to be less stable. In other words, the assumption of equal load sharing tends to overestimate the cluster lifetime. We will include the effects of cell/ECM elasticity on cluster lifetime through a coupled stochastic-elasticity model in the following chapters.

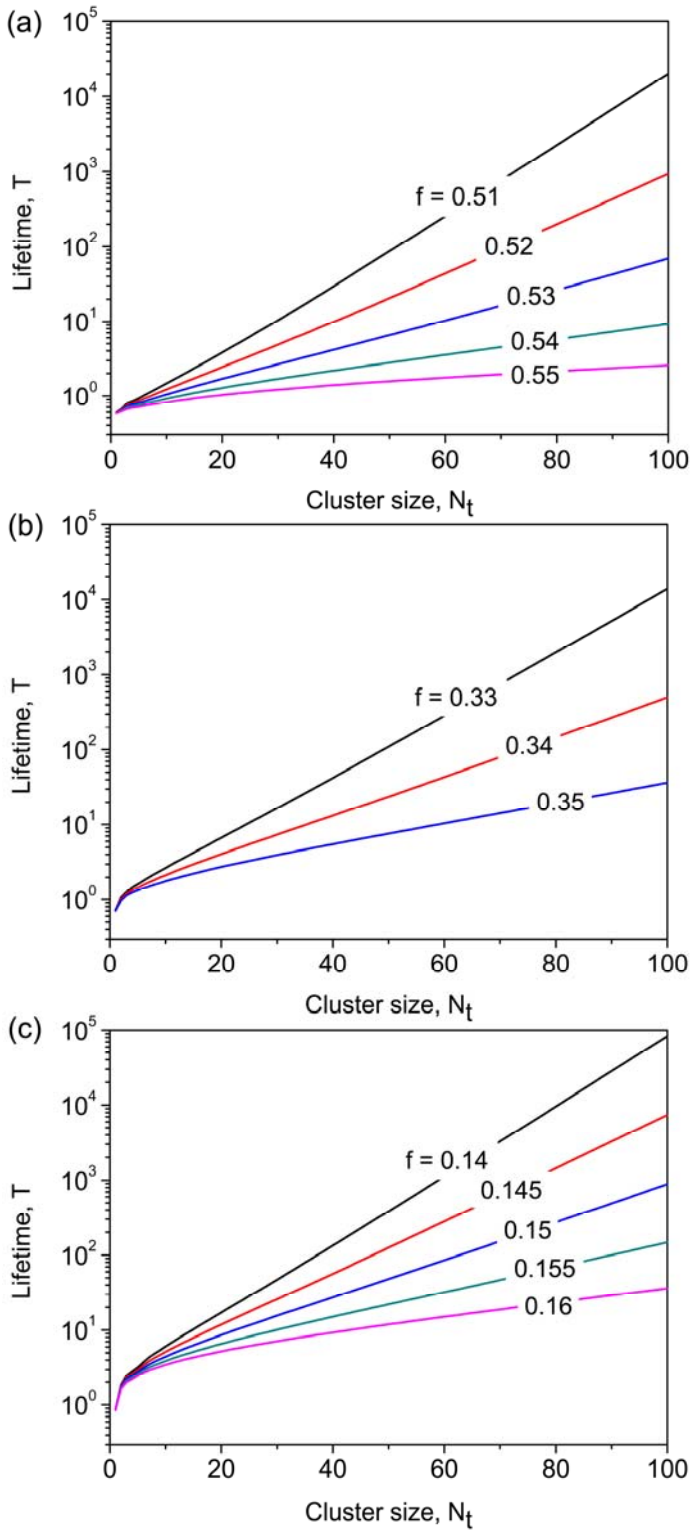

Figure 2.7: The lifetime T of a molecular bond cluster between rigid bodies as a function of the cluster size N_t at various load levels f. The prefactor for rebinding is taken to be (a) $\gamma = 100$; (b) $\gamma = 10$; (c) $\gamma = 1.0$.

Chapter 3

Elastic model of interfacial adhesion

3.1 General formulation

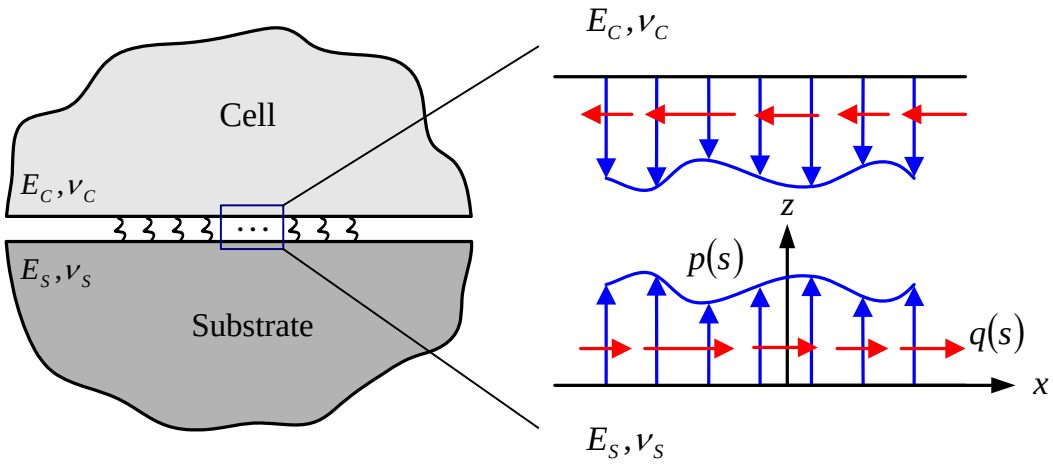

Figure 3.1: A bi-material (cell-ECM) interface subjected to distributed normal and tangential tractions.

The theoretical model under consideration is shown in Figure 3.1, where a number of receptor-ligand bonds establish a colony of adhesion between two dissimilar elastic media under an applied load. To account for the elasticity of the system in a simple way, we consider a slice of the system with out-of-plane thickness b as a plane strain problem. The molecular bonds are uniformly distributed within the adhesion domain at an equal

spacing of b, which corresponds to a bond density of $\rho_{LR} = 1/b^2$. Only specific adhesion via receptor-ligand linkages is considered and secondary non-specific interactions are ignored. Each bond is modeled as a Hookean spring with rest length l_b and stiffness k_{LR} until rupture.

One side of the adhesion is an elastic medium mimicking the body of a cell and the other side represents an elastic substrate (ECM). The Young's modulus and Poisson's ratio are E_C, ν_C for the cell and E_S, ν_S for the substrate. In such a bi-material contact problem, it is usually convenient to introduce the so-called reduced elastic modulus E^* defined as [44]

$$\frac{1}{E^*} = \frac{1-\nu_C^2}{E_C} + \frac{1-\nu_S^2}{E_S}. \tag{3.1}$$

We adopt a set of coordinates (x, z) with directions shown in Figure 3.1. The surface displacement u of the cell body, approximated as an elastic half-space, in terms of the distributed normal and shear tractions at the interface, $p(x)$ and $q(x)$ respectively, is given by [44]

$$\frac{\partial u_x^C}{\partial x} = \frac{2(1-\nu_C^2)}{\pi E_C}\int_{-\infty}^{\infty}\frac{q(s)}{x-s}\mathrm{d}s + \frac{(1-2\nu_C)(1+\nu_C)}{E_C}p(x), \tag{3.2a}$$

$$\frac{\partial u_z^C}{\partial x} = \frac{2(1-\nu_C^2)}{\pi E_C}\int_{-\infty}^{\infty}\frac{p(s)}{x-s}\mathrm{d}s - \frac{(1-2\nu_C)(1+\nu_C)}{E_C}q(x). \tag{3.2b}$$

Similarly for the substrate,

$$\frac{\partial u_x^S}{\partial x} = -\frac{2(1-\nu_S^2)}{\pi E_S}\int_{-\infty}^{\infty}\frac{q(s)}{x-s}\mathrm{d}s + \frac{(1-2\nu_S)(1+\nu_S)}{E_S}p(x), \tag{3.3a}$$

$$\frac{\partial u_z^S}{\partial x} = -\frac{2\left(1-\nu_S^2\right)}{\pi E_S}\int_{-\infty}^{\infty}\frac{p(s)}{x-s}\mathrm{d}s - \frac{(1-2\nu_S)(1+\nu_S)}{E_S}q(x). \tag{3.3b}$$

Consider the tangential and normal components of displacement discontinuities across the interface

$$\Delta u_x = u_x^C - u_x^S, \tag{3.4a}$$

$$\Delta u_z = u_z^C - u_z^S. \tag{3.4b}$$

Equations (3.2) and (3.3) are combined into

$$\frac{\partial \Delta u_x}{\partial x} = \frac{2}{\pi}\frac{1}{E^*}\int_{-\infty}^{\infty}\frac{q(s)}{x-s}\mathrm{d}s + \frac{2D}{E^*}p(x), \tag{3.5a}$$

$$\frac{\partial \Delta u_z}{\partial x} = \frac{2}{\pi}\frac{1}{E^*}\int_{-\infty}^{\infty}\frac{p(s)}{x-s}\mathrm{d}s - \frac{2D}{E^*}q(x), \tag{3.5b}$$

where

$$D = \frac{1}{2}\left\{\frac{(1-2\nu_C)(1+\nu_C)/E_C - (1-2\nu_S)(1+\nu_S)/E_S}{\left(1-\nu_C^2\right)/E_C + \left(1-\nu_S^2\right)/E_S}\right\} \tag{3.6}$$

is recognized as one of the Dundurs' constants [45]. It has been pointed out before that D plays a rather minor role in interfacial crack problems [46]. Since biological materials are often modeled as incompressible, the Poisson's ratio would be near $1/2$, in which case $D \approx 0$. Taking $D = 0$, we observe that the tangential and normal components of the interfacial traction become decoupled, and the displacement discontinuity is related to the interfacial traction through the same integral equation in tangential and normal directions.

For molecular bonds modeled as Hookean spring with stiffness k_{LR} and in density ρ_{LR}, the tangential and normal components of the traction within the adhesion region, denoted as $\tau(x)$ and $\sigma(x)$ respectively, are related to the displacement discontinuities

across the interface as

$$\frac{\partial \tau(x)}{\partial x} = \rho_{LR} k_{LR} \frac{\partial \Delta u_x}{\partial x}, \tag{3.7a}$$

$$\frac{\partial \sigma(x)}{\partial x} = \rho_{LR} k_{LR} \frac{\partial \Delta u_z}{\partial x}. \tag{3.7b}$$

3.2 Stress concentration index

If a tensile load is applied far from the interface, as indicated in Figure 3.2 for a single adhesion patch and periodic adhesion clusters, the shear and normal tractions at the interface, $q(x)$ and $p(x)$, are equal to those on the molecular bonds, i.e.

$$\tau(x) = q(x), \tag{3.8a}$$

$$\sigma(x) = p(x). \tag{3.8b}$$

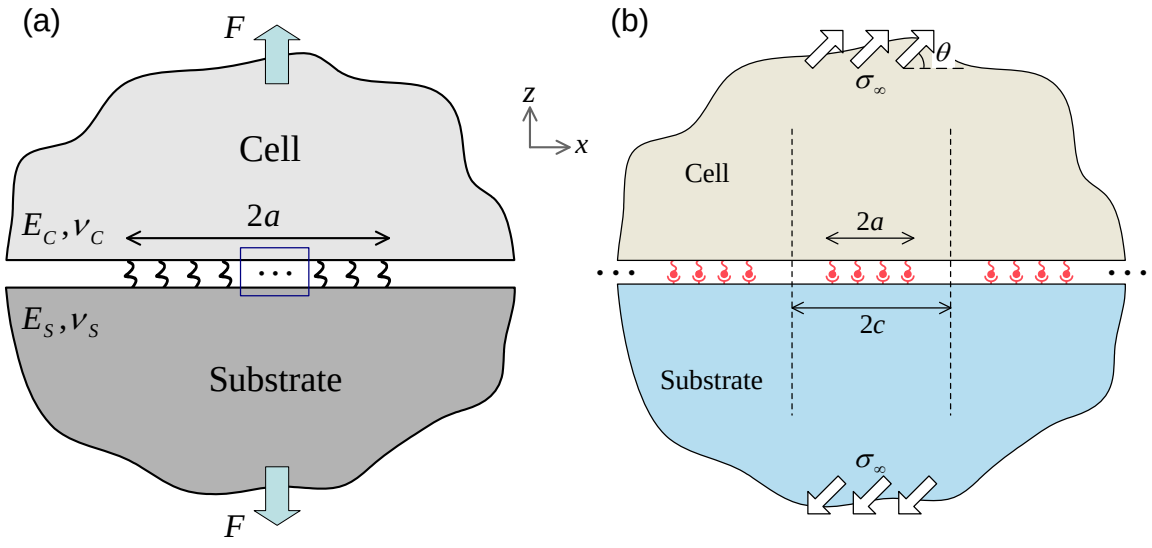

Figure 3.2: (a) A single adhesion patch of size $2a$ subjected to a remote tensile force F. (b) An array of periodic adhesion clusters of size $2a$ distributed at a period $2c$. A remote tensile stress σ_∞ is applied at an inclined angle θ with respect to the cell-substrate interface.

3.2.1 A single adhesion patch

For a single adhesion patch ($-a \le x \le a$) under a remote tensile load F, as shown in Figure 3.2a, combining Equations (3.5b), (3.7b) and (3.8b) gives the following governing equation

$$\frac{\partial \sigma(\hat{x})}{\partial \hat{x}} = \frac{2\alpha}{\pi} \int_{-1}^{1} \frac{\sigma(\hat{s})\mathrm{d}\hat{s}}{\hat{x} - \hat{s}}, \tag{3.9}$$

where $\hat{x}$, $\hat{s}$ are coordinates normalized by the adhesion half-width a and

$$\alpha = a\rho_{LR}k_{LR}\left(\frac{1-\nu_C^2}{E_C} + \frac{1-\nu_S^2}{E_S}\right) \tag{3.10}$$

is identified as a controlling parameter to determine how interfacial traction $\sigma(x)$ is distributed within the adhesion domain.

On the other hand, the global force balance requires that

$$\int_{-a}^{a} \sigma(x)\mathrm{d}x = \frac{F}{b}, \tag{3.11}$$

where F has the usual dimension of Newton.

In the limit $\alpha \to 0$, we have the solution

$$\sigma(x) = \frac{F}{2ab} = \text{constant}, \tag{3.12}$$

indicating that the applied force F is equally shared among all bonds within the adhesion patch, as in the assumption adopted by Erdmann and Schwarz [20,21]. However, in the opposite limit $\alpha \to \infty$, the solution becomes

$$\sigma(x) = \frac{F}{\pi ab}\frac{1}{\sqrt{1-x^2/a^2}}, \tag{3.13}$$

corresponding to the interfacial traction distribution for a 2D external crack [47]. In this case, the stress distribution at the edges of adhesion is actually singular. For the

intermediate range $0 < \alpha < \infty$, the maximum stress generally occurs at the edges of the patch and the minimum stress appears at the center. The numerical results (see Appendix A for detailed descriptions of our numerical formulation) in Figure 3.3 show that, for α values smaller than 0.1, the interfacial stress is nearly uniformly distributed within the adhesion patch, while for α values larger than 1, stress concentration emerges near the patch edges, similar to the crack solution in Equation (3.13). We shall refer to α as the stress concentration index (SCI).

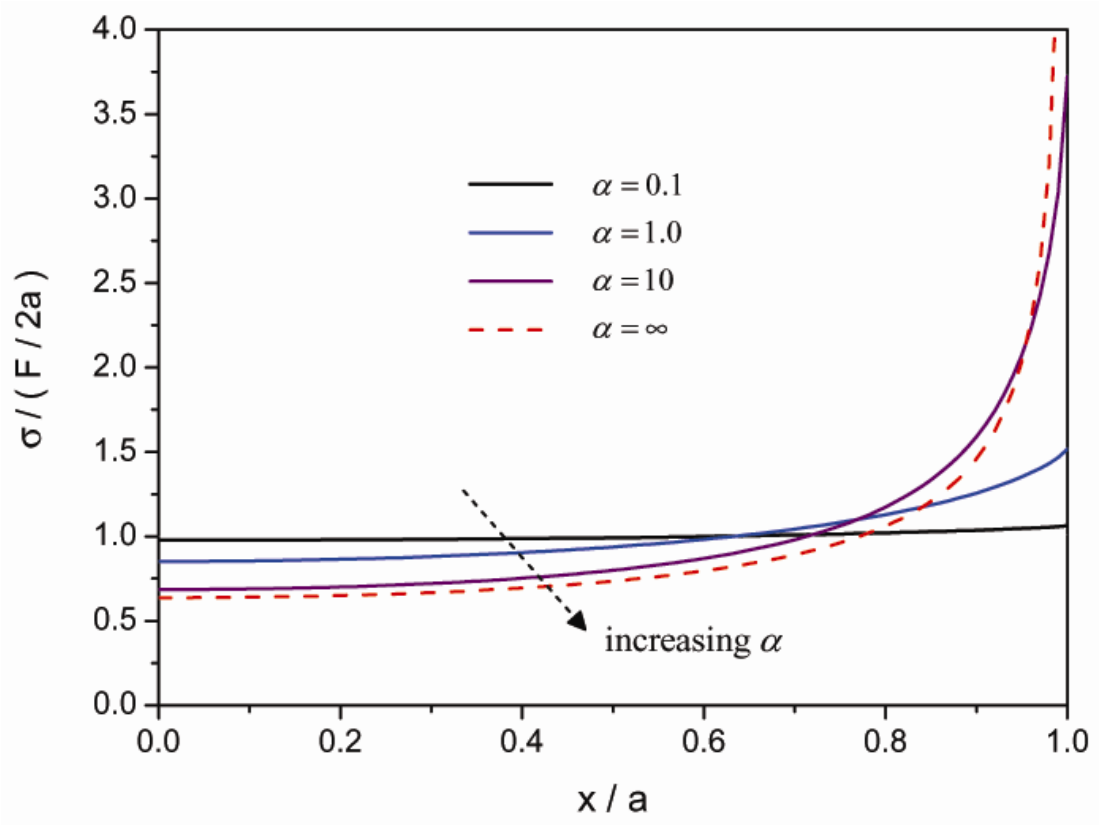

Figure 3.3: The distributions of interfacial traction within a single adhesion patch for different values of the stress concentration index $\alpha = a\rho_{LR}k_{LR} / E^*$.

3.2.2 Periodic adhesion clusters

For periodic adhesion clusters of size $2a$ which are distributed at a period of $2c$ along

the interface subjected to a remote tensile stress σ_∞ applied at an inclined angle θ with respect to the cell-substrate interface, as shown in Figure 3.2b, the governing equations are (see Appendix B for derivations)

$$\frac{\partial \tau(\hat{x})}{\partial \hat{x}} = \overline{\alpha} \int_{-1}^{1} \tau(\hat{s}) \cot\left(\frac{\pi(\hat{x}-\hat{s})}{2\hat{c}} \right) \mathrm{d}\hat{s}, \tag{3.14a}$$

$$\frac{\partial \sigma(\hat{x})}{\partial \hat{x}} = \overline{\alpha} \int_{-1}^{1} \sigma(\hat{s}) \cot\left(\frac{\pi(\hat{x}-\hat{s})}{2\hat{c}} \right) \mathrm{d}\hat{s}, \tag{3.14b}$$

where

$$\overline{\alpha} = a\overline{\rho}_{LR} k_{LR} \left(\frac{1-\nu_C^2}{E_C} + \frac{1-\nu_S^2}{E_S} \right) \tag{3.15}$$

emerges as the only controlling parameter. Here $\overline{\rho}_{LR}$ is the average bond density along the interface defined by the relation $c\overline{\rho}_{LR} = a\rho_{LR}$.

The global force balance requires that

$$\int_{-a}^{a} \tau(x) \mathrm{d}x = 2c\sigma_\infty \sin\theta\cos\theta, \tag{3.16a}$$

$$\int_{-a}^{a} \sigma(x) \mathrm{d}x = 2c\sigma_\infty \sin^2\theta. \tag{3.16b}$$

The effect of $\overline{\alpha}$ on the distribution of interfacial traction can be immediately understood from the solutions to Equations (3.14) and (3.16) in extreme cases. In the limiting case $\overline{\alpha} \to 0$, the solution is

$$\tau(x) = \frac{\sigma_\infty \sin\theta\cos\theta}{a/c}, \sigma(x) = \frac{\sigma_\infty \sin^2\theta}{a/c} \quad (-a \le x \le a) \tag{3.17}$$

within the adhesion domain, indicating a uniform distribution of interfacial traction independent of the bond location x. In this limit, the interfacial traction is equally shared among all bonds. In the opposite limit when $\overline{\alpha} \to \infty$, the solution becomes

$$\tau(x)=\frac{\sigma_\infty \sin\theta\cos\theta}{\sqrt{1-\cos^2\frac{\pi a}{2c}\Big/\cos^2\frac{\pi x}{2c}}},\ \sigma(x)=\frac{\sigma_\infty \sin^2\theta}{\sqrt{1-\cos^2\frac{\pi a}{2c}\Big/\cos^2\frac{\pi x}{2c}}}\ \ (-a\le x\le a). \tag{3.18}$$

This is the classical singular solution for a periodic array of interfacial cracks [47]. The numerical results in Figure 3.4 show that the interfacial traction is nearly uniform for $\overline{\alpha}$ values smaller than 0.1 while a crack-like stress concentration emerges near the adhesion edges for $\overline{\alpha}$ values larger than 1, which is similar to the results for a single adhesion patch discussed in the previous section.

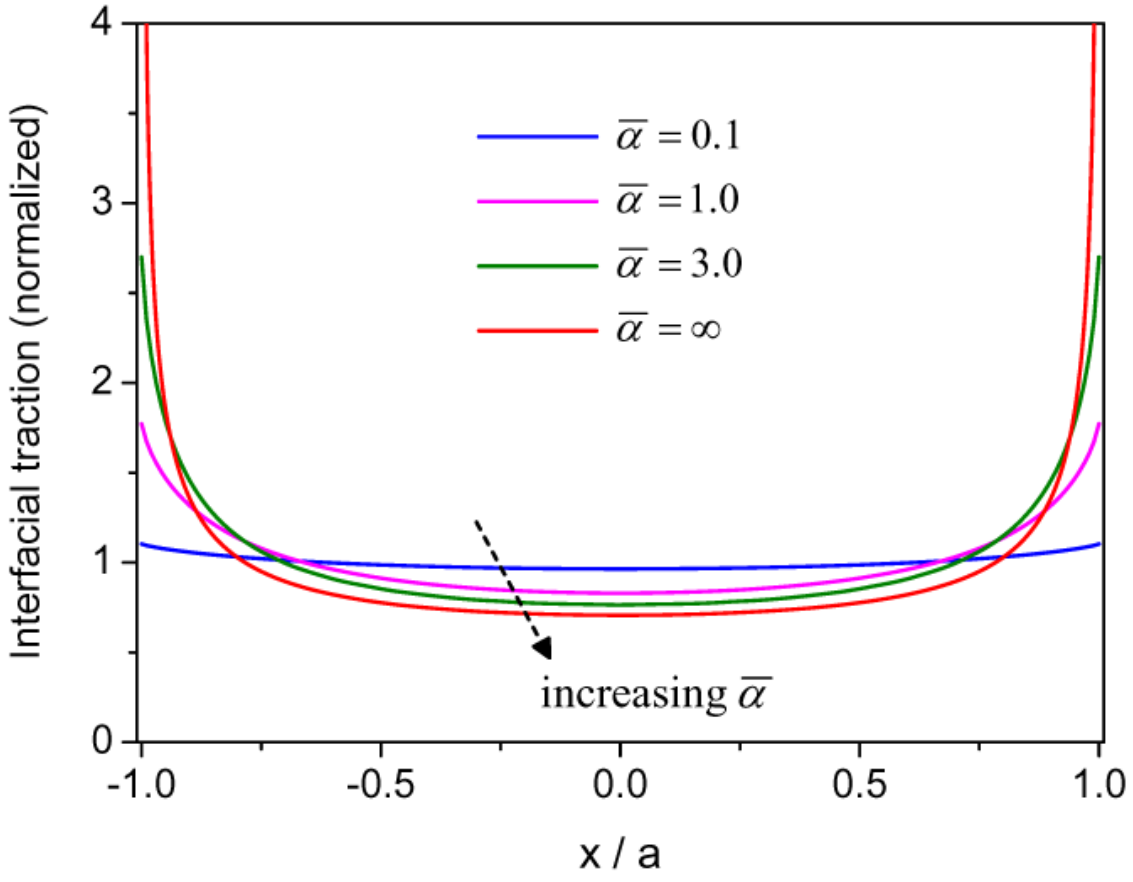

Figure 3.4: The distributions of normalized interfacial traction within periodic adhesion clusters at different values of the stress concentration index $\overline{\alpha}=a\overline{\rho}_{LR}k_{LR}/E^*$. The results indicate a transition between uniform and crack-like singular distributions ($D=0$ and $c/a=2$).

3.3 Green's function approach for discrete bonds

3.3.1 A single adhesion patch

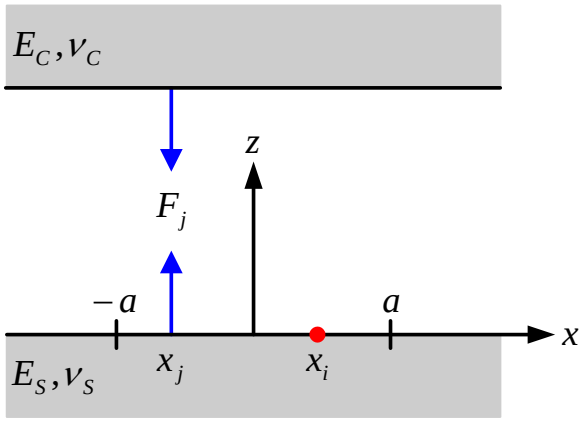

Figure 3.5: Discontinuity of surface displacement induced by a normal concentrated force at a bi-material interface.

Since we will consider the random events of dissociation and association in a group of discrete molecular bonds, it will be convenient to discretize the elastic equations to facilitate the determination of bond forces and surface separations. A set of coordinates (x, z) are adopted with directions defined in Figure 3.5. The normal displacement u_z of the cell surface at a bond location x_i induced by a different bond at location x_j $(i \neq j)$ is given by [44]

$$u_z^C(x_i, x_j) = -\frac{2(1-\nu_C^2)}{\pi E_C}\frac{F_j}{b}\left(\ln|x_\infty - x_j| - \ln|x_i - x_j|\right), \tag{3.19}$$

where F_j is the bond force at x_j, and x_∞ is an arbitrary reference point that will not influence the solution. Similarly for the substrate,

$$u_z^S(x_i, x_j) = \frac{2(1-\nu_S^2)}{\pi E_S}\frac{F_j}{b}\left(\ln|x_\infty - x_j| - \ln|x_i - x_j|\right). \tag{3.20}$$

Combining Equations (3.19) and (3.20) gives the discontinuity of the normal displacement at x_i induced by the force at x_j, i.e.

$$\Delta u_z\left(x_i, x_j\right) = u_z^C - u_z^S = G_{ij} F_j, \tag{3.21}$$

where G_{ij} is the elastic Green's function given as

$$G_{ij} = -\frac{2}{\pi E^* b}\left(\ln\left|x_\infty - x_j\right| - \ln\left|x_i - x_j\right|\right). \tag{3.22}$$

Notice that Equation (3.22) is actually singular when $i = j$. To avoid this singularity, the self displacement discontinuity at x_i induced by the force F_i, which is modeled as an equivalent uniform pressure with half-width a_0, is given by [44]

$$\Delta u_z\left(x_i, x_i\right) = \frac{1}{\pi E^*}\frac{F_i}{2a_0 b}\left(2a_0 \ln 4 + C_i\right) = G_{ij} F_j \quad \left(\text{for } i = j\right), \tag{3.23}$$

where a_0 denotes the radius of individual molecular bonds with its typical value on the order of a few nanometers [48] and C_i is a length constant chosen to satisfy the condition that F_i causes zero displacement at the reference point x_∞.

The compatibility condition at the cell-substrate interface is that the bond length after deformation is equal to the displacement discontinuity Δu_z plus a constant separation h, i.e.

$$h + \Delta u_z\left(x_i\right) = \frac{F_i}{k_{LR}} + l_b, \tag{3.24}$$

where k_{LR} and l_b are the stiffness and rest length of a receptor-ligand bond, respectively. Equation (3.24) can be rearranged into

$$\sum_{j=1}^{k} G_{ij} F_j - \frac{F_i}{k_{LR}} + h = l_b \,, \tag{3.25}$$

where

$$G_{ij} = \begin{cases} -\dfrac{2}{\pi E^* b}\left(\ln\left|x_\infty - x_j\right| - \ln\left|x_i - x_j\right|\right) & (\text{for } i \neq j) \\ \dfrac{1}{\pi E^* \cdot 2a_0 b}\left(2a_0 \ln 4 + C_i\right) & (\text{for } i = j) \end{cases} . \tag{3.26}$$

The k in Equation (3.25) is the current number of closed bonds within the adhesion region. The $k+1$ unknowns $\left(F_1, F_2, \cdots, F_k, h\right)$ are solved from the above k equations together with the global force balance

$$\sum_{i=1}^{k} F_i = F \,. \tag{3.27}$$

Once the solution of $k+1$ unknowns is obtained, the surface separation δ_i between the two elastic media at x_i where an open bond locates can be calculated from

$$\delta_i = \sum_{j=1}^{k} G_{ij} F_j + h \,. \tag{3.28}$$

3.3.2 Periodic adhesion clusters

Consider a periodic array of concentrated forces with period $2c$ along the interface. We focus on an arbitrary period and adopt (x, z) coordinates with origin located at the center and directions shown in Figure 3.6. The discontinuities of tangential and normal displacements at a bond location x_i caused by a different bond at location x_j ($i \neq j$) are given by [49]

$$\Delta u_x\left(x_i, x_j\right) = \frac{2F_j^{//}}{\pi E^* b} \ln\left|\sin\frac{\pi\left(x_i - x_j\right)}{2c}\right|, \tag{3.29a}$$

$$\Delta u_z(x_i, x_j) = \frac{2F_j^{\perp}}{\pi E^* b} \ln\left|\sin\frac{\pi(x_i - x_j)}{2c}\right|, \tag{3.29b}$$

where $F_j^{//}$ and $F_j^{\perp}$ are the tangential and normal components of the bond force at x_j.

To avoid singularity, the self displacement discontinuities at x_i induced by the force array F_i, which is modeled as an array of equivalent uniform pressure with half-width a_0, are given as

$$\Delta u_x(x_i, x_i) = \frac{2F_i^{//}}{\pi E^* b} \ln\left|\sin\frac{\pi b}{2c}\right| + \frac{F_i^{//}}{\pi E^* a_0 b}\int_{-b}^{0} \ln\left|\frac{\sin(\pi(x + a_0)/2c)}{\sin(\pi(x - a_0)/2c)}\right| dx, \tag{3.30a}$$

$$\Delta u_z(x_i, x_i) = \frac{2F_i^{\perp}}{\pi E^* b} \ln\left|\sin\frac{\pi b}{2c}\right| + \frac{F_i^{\perp}}{\pi E^* a_0 b}\int_{-b}^{0} \ln\left|\frac{\sin(\pi(x + a_0)/2c)}{\sin(\pi(x - a_0)/2c)}\right| dx. \tag{3.30b}$$

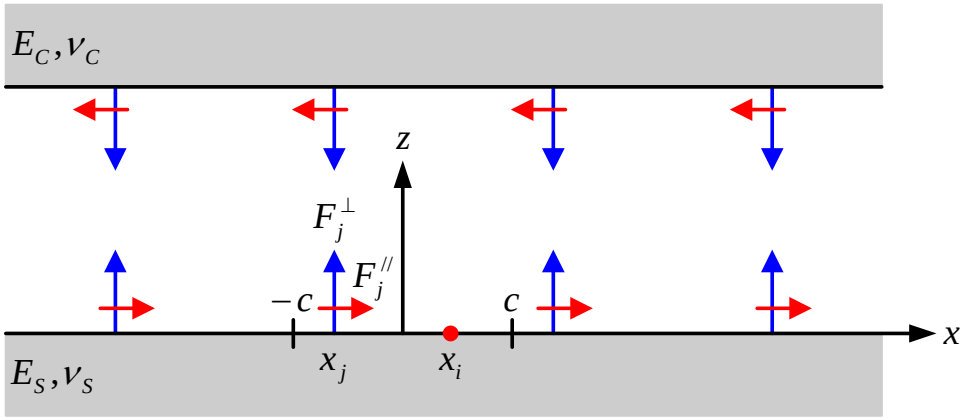

Figure 3.6: Surface displacement discontinuities induced by an array of concentrated forces with period $2c$.

The compatibility condition at the interface is

$$\sum_{j=1}^{k} G_{ij} F_j - \frac{F_i}{k_{LR}} + h = l_b, \tag{3.31}$$

where $F_j = \sqrt{F_j^{//2} + F_j^{\perp 2}}$, h is the cell-substrate separation in the absence of elastic

deformation and

$$G_{ij}=\begin{cases}\dfrac{2}{\pi E^{*}b}\ln\left|\sin\dfrac{\pi\left(x_i-x_j\right)}{2c}\right| & \left(\text{for } i\neq j\right)\\ \dfrac{2}{\pi E^{*}b}\ln\left|\sin\dfrac{\pi b}{2c}\right|+\dfrac{1}{\pi E^{*}a_0 b}\displaystyle\int_{-b}^{0}\ln\left|\frac{\sin\left(\pi\left(x+a_0\right)/2c\right)}{\sin\left(\pi\left(x-a_0\right)/2c\right)}\right|\mathrm{d}x & \left(\text{for } i=j\right)\end{cases} \tag{3.32}$$

is the elastic Green's function for a periodic array of forces.

The global force balance requires that

$$\sum_{i=1}^{k}F_i=2bc\sigma_{\infty}\sin\theta\,. \tag{3.33}$$

Once the $k+1$ unknowns $\left(F_1,F_2,\cdots,F_k,h\right)$ are solved, the surface separation δ_i between the two elastic media at an open bond location x_i can be calculated through

$$\delta_i=\sum_{j=1}^{k}G_{ij}F_j+h\,. \tag{3.34}$$

3.4 Molecular bond clusters subjected to uniform tensile stress

In addition to the remotely applied loading, it will also be interesting to study the behavior of molecular bond clusters subjected to a uniform tension applied directly along the interface. For a single adhesion patch under a uniform tensile stress P over the adhesion domain $-a\le x\le a$, as indicated in Figure 3.7, we have

$$p\left(x\right)=\sigma\left(x\right)-P\,. \tag{3.35}$$

The governing equation is

$$\frac{\partial\sigma\left(x\right)}{\partial x}=\frac{2}{\pi}\frac{1}{E^{*}}\int_{-a}^{a}\frac{\sigma\left(s\right)-P}{x-s}\mathrm{d}s\,, \tag{3.36}$$

whose solution is simply

$$\sigma(x) = P\,. \tag{3.37}$$

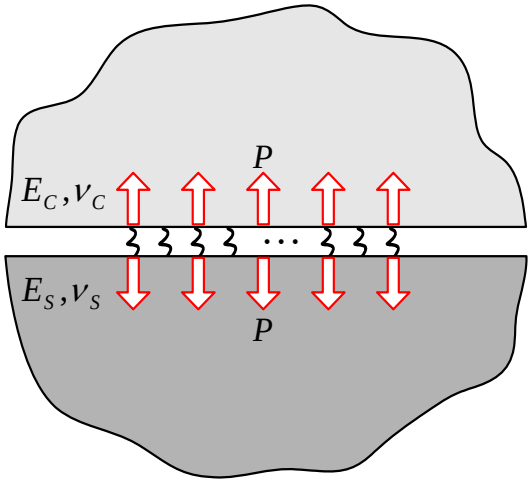

Figure 3.7: A single adhesion patch between two elastic media subjected to a tensile stress P directly applied along the interface.

In this case, the applied load is initially equally shared among all bonds, independent of the system elasticity. However, the behavior of individual molecular bonds is dynamic and the density of closed bonds, ρ_{LR}, is constantly subjected to perturbations due to the stochastic events of rupture and rebinding. Consider a sinusoidal profile of bond density

$$\rho_{LR}(x) = \rho_0\left(1 + \rho\sin(\pi x/a)\right). \tag{3.38}$$

The governing equation becomes

$$\frac{\partial\hat{\sigma}(\hat{x})}{\partial\hat{x}} = \left(1+\rho\sin(\pi\hat{x})\right)\frac{2\alpha}{\pi}\int_{-1}^{1}\frac{\hat{\sigma}(\hat{s})-1}{\hat{x}-\hat{s}}\mathrm{d}\hat{s} + \hat{\sigma}(\hat{x})\frac{\pi\rho\cos(\pi\hat{x})}{1+\rho\sin(\pi\hat{x})}, \tag{3.39}$$

where $\hat{x}$, $\hat{s}$ are coordinates normalized by the adhesion half-width a, $\hat{\sigma} = \sigma/P$ and α is the stress concentration index given in Equation (3.10). Equation (3.39) can be numerically solved with the global force balance

$$\int_{-1}^{1} \hat{\sigma}(\hat{s})\mathrm{d}\hat{s} = 2\,. \tag{3.40}$$

Figure 3.8 plots the distributions of force per bond (normalized by P/ρ_0) within the adhesion patch for different values of α in the presence of density perturbations. For the same perturbation in bond density, the distribution of force per bond becomes increasingly non-uniform with increasing α. Therefore, the stress concentration index α still serves as a governing parameter to determine the distribution of bond force during cluster evolution, even though the cluster is subjected to uniform traction initially.

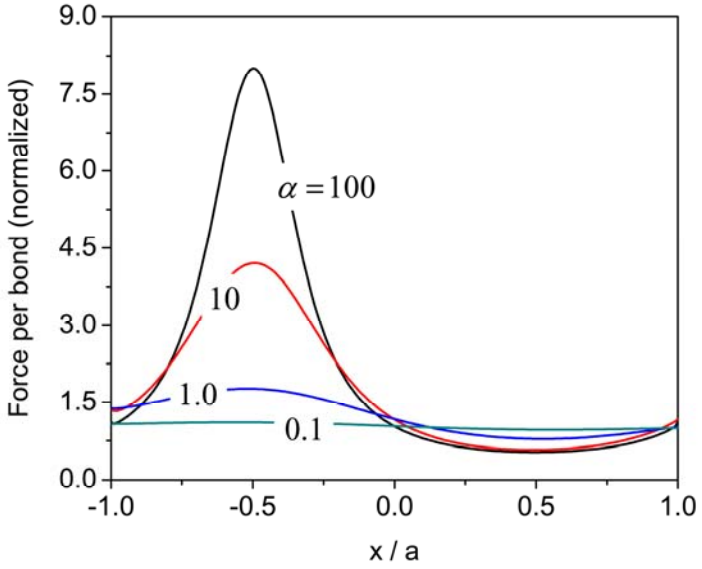

Figure 3.8: The distributions of force per bond (normalized by P/ρ_0) within a single adhesion patch with sinusoidal bond density for different values of the stress concentration index $\alpha = a\rho_{LR}k_{LR}/E^*$ ($\rho = 0.9$).

Now let us discuss the situation of equal load sharing in the presence of elastic deformation for a series of discrete molecular bonds. The displacement discontinuity Δu_z due to all the closed bonds is

$$\Delta u_z(x_i) = \sum_{j=1}^{k} G_{ij} F_j \,, \tag{3.41}$$

where F_j is the bond force and G_{ij} is the elastic Green's function in Equation (3.26). On the other hand, the tensile stress P applied at the interface also causes displacement discontinuity at x_i, which is given by [44]

$$\Delta u_z(x_i, P) = -\frac{P}{\pi E^*}\left((a + x_i)\ln\left(\frac{a + x_i}{a}\right)^2 + (a - x_i)\ln\left(\frac{a - x_i}{a}\right)^2 + C_P \right), \tag{3.42}$$

where C_P is to satisfy the condition that P causes zero displacement at the same reference point x_∞.

The conditions of interface compatibility and global force balance are

$$\sum_{j=1}^{k} G_{ij} F_j + \Delta u_z(x_i, P) - \frac{F_i}{k_{LR}} + h = l_b \,, \tag{3.43a}$$

$$\sum_{i=1}^{k} F_i = P \cdot 2ab \,. \tag{3.43b}$$

Once the $k+1$ unknowns $(F_1, F_2, \cdots, F_k, h)$ are solved from Equation (3.43), the surface separation δ_i between the two elastic media can be calculated by

$$\delta_i = \sum_{j=1}^{k} G_{ij} F_j + \Delta u_z(x_i, P) + h \tag{3.44}$$

for any open bond location x_i.

The bond forces on closed bonds and surface separations at open bonds are used to compute the reaction rates (rupture or rebinding) of a bond cluster for any instantaneous bond configurations during the cluster evolution. The next chapter will discuss how the cluster evolves according to the calculated reaction rates.

Chapter 4

Stochastic-elasticity model

According to the elasticity formulation described in Chapter 3, one can determine bond force and surface separation using the appropriate elastic Green's functions for any instantaneous bond configuration during the stochastic process. The analytical solution of the original master equation seems hardly possible for the present case with spatially dependent rupture and rebinding rates. Therefore, we develop a Monte Carlo scheme based on Gillespie's algorithm [50,51] to numerically solve the spatio-temporal process governed by the master equation.

The basic idea of our approach is to cast stochastic trajectories of cluster evolution in accordance with the above described reaction rates and average over many independent trials to obtain useful statistical information. At any step during the cluster evolution, random numbers are generated to determine whether the next activity is bond breaking or rebinding, and how long it takes for the next reaction to occur. For our modeling with spatial degrees of freedom, it is also necessary to determine where the next event should occur. Previously, a number of numerical algorithms have been developed for studying bond kinetics in cell adhesion [52,53]. In the present study, we apply the so-called "first-

reaction" method [50,51] of Gillespie's algorithm, which was also adopted by Erdmann and Schwarz in their simulations under the assumption of equal load sharing [20,21].

4.1 Probability distribution of bond reactions

We consider each bond, open or closed, as an independent reaction site. At an instantaneous time, suppose that there exist a set of bond reactions, labeled by $\mu = 1, 2, \cdots, N_t$, and we know all of the reaction rates a_μ, which are calculated from the force among closed bonds and surface separation at open bonds in the elasticity analysis (Figure 4.1), i.e.

$$a_\mu = \begin{cases} r(F_\mu), \text{ if bond } \mu \text{ is closed} \\ g(\delta_\mu), \text{ if bond } \mu \text{ is open} \end{cases}, \tag{4.1}$$

where r and g are the dissociation and association rates given in Equation (2.9).

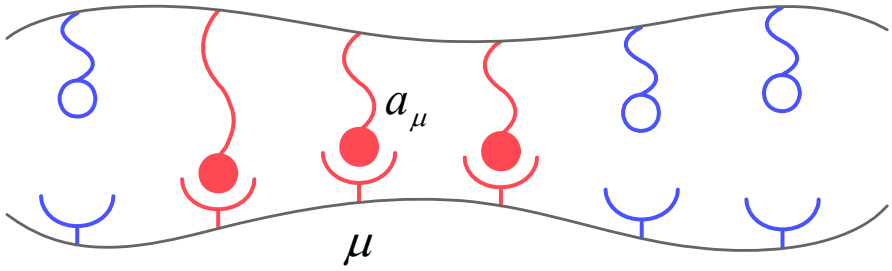

Figure 4.1: A cluster of molecular bonds in space with different reaction rates at an instantaneous time during the cluster evolution.

To advance the bond evolution, one needs to answer the following questions:

i) When does the next reaction occur?

ii) Where does the next reaction occur?

iii) Which type of reaction is it?

We define $P(\mu,\tau)\mathrm{d}\tau$ as the probability at an instantaneous time (set as the zero point hereafter) that the next event will be reaction μ and will occur in the time interval $(\tau,\tau+\mathrm{d}\tau)$. According to the probability theory,

$$P(\mu,\tau)\mathrm{d}\tau = P_0(\tau)\cdot a_\mu \mathrm{d}\tau\,, \tag{4.2}$$

where $P_0(\tau)$ is the probability that no reaction will occur in the time interval $(0,\tau)$. Thus $P_0(\tau+\mathrm{d}\tau)$, the probability that no reaction will occur up to $\tau+\mathrm{d}\tau$, is given by

$$P_0(\tau+\mathrm{d}\tau) = P_0(\tau)\cdot(1-a_{total}\mathrm{d}\tau), \tag{4.3}$$

where $a_{total}=\sum_\mu a_\mu$ is the sum of all reaction rates at the current time. We shall rearrange Equation (4.3) into

$$\frac{\mathrm{d}P_0(\tau)}{\mathrm{d}\tau} = -a_{total}P_0(\tau), \tag{4.4}$$

which has the simple solution $P_0(\tau)=P_0(0)\exp(-a_{total}\tau)$. Obviously, the initial condition is $P_0(0)=1$ and we obtain

$$P_0(\tau)=\exp(-a_{total}\tau). \tag{4.5}$$

Equation (4.2) then shows that $P(\mu,\tau)$ obeys the following distribution [50,51]:

$$P(\mu,\tau)=a_\mu\exp(-a_{total}\tau)\,, \tag{4.6}$$

where $a_{total}=\sum_\mu a_\mu$. One can immediately check that this probability density function is properly normalized since

$$\int_0^\infty \mathrm{d}\tau \sum_\mu P(\mu, \tau) = 1 . \tag{4.7}$$

The time space for the formula is $0 \le \tau < \infty$. With the probability density function in Equation (4.6), we have answered when and where the next reaction will occur. The type of next reaction will be bond rupture if the bond is currently closed, and bond rebinding if the bond is currently open.

4.2 The "first-reaction" method

To determine μ and τ for the next reaction according to the probability distribution $P(\mu, \tau) = a_\mu \exp(-a_{total}\tau)$, the "first-reaction" method [50,51] is to generate a series of independent random numbers ξ_ν, $\nu = 1, 2, \cdots, N_t$, which are uniformly distributed over the interval [0, 1], and calculate the reaction time for individual reaction sites according to

$$\tau_\nu = -\frac{\ln \xi_\nu}{a_\nu} . \tag{4.8}$$

The time for the next reaction is chosen to be the smallest among τ_ν, and the corresponding site is the actual reaction to occur, i.e.

$$\tau_\mu = \min(\tau_\nu) . \tag{4.9}$$

The proof of the algorithm is given as follows. Suppose that the "first-reaction" method generates a random pair (μ, τ) obeying the probability distribution $P'(\mu, \tau)$, we want to show that $P'(\mu, \tau) = P(\mu, \tau)$. The "first-reaction" method states that [50,51]

$$P'(\mu,\tau)\mathrm{d}\tau = \mathrm{Prob}(\tau < \tau_\mu < \tau + \mathrm{d}\tau)\cdot \mathrm{Prob}(\tau_\nu > \tau, \mathrm{all}\,\nu \neq \mu). \tag{4.10}$$

The first factor on the right-hand side is the probability that reaction μ occurs in the time interval $(\tau, \tau+\mathrm{d}\tau)$, so that

$$\mathrm{Prob}(\tau < \tau_\mu < \tau + \mathrm{d}\tau) = a_\mu \exp(-a_\mu\tau)\mathrm{d}\tau\,. \tag{4.11}$$

The second factor $\mathrm{Prob}(\tau_\nu > \tau, \mathrm{all}\,\nu \neq \mu)$ is the probability that all other reactions occur later than μ. According to the "first-reaction" method,

$$\begin{aligned}
&\mathrm{Prob}(\tau_\nu > \tau, \mathrm{all}\,\nu \neq \mu) = \mathrm{Prob}\left(-\frac{\ln\xi_\nu}{a_\nu} > \tau, \mathrm{all}\,\nu \neq \mu\right) \\
&= \mathrm{Prob}(\xi_\nu < \exp(-a_\nu\tau), \mathrm{all}\,\nu \neq \mu) = \prod_{\mathrm{all}\,\nu\neq\mu} \mathrm{Prob}(\xi_\nu < \exp(-a_\nu\tau)). \\
&= \prod_{\mathrm{all}\,\nu\neq\mu} \exp(-a_\nu\tau)
\end{aligned} \tag{4.12}$$

Thus,

$$\begin{aligned}
&P'(\mu,\tau)\mathrm{d}\tau = a_\mu \mathrm{d}\tau \exp(-a_\mu\tau)\cdot \prod_{\mathrm{all}\,\nu\neq\mu} \exp(-a_\nu\tau) \\
&= a_\mu \mathrm{d}\tau \exp\left(-\sum_\mu a_\mu\tau\right) = a_\mu \mathrm{d}\tau\cdot\exp(-a_{total}\tau) \quad . \\
&= P(\tau,\mu)\mathrm{d}\tau
\end{aligned} \tag{4.13}$$

The "first-reaction" method [50,51], as defined through Equations (4.8) and (4.9), is indeed a legitimate way to implement the probability distribution in Equation (4.6).

4.3 Monte Carlo scheme for the stochastic-elasticity model

For a molecular bond cluster, we need to determine a series of reaction rates denoted as a_μ, μ referring to a bond location, from the calculated dissociation or association rates

depending on the current bond state. We generate a series of independent random numbers, which are uniformly distributed over the interval [0, 1], for individual reaction sites. The time for the next reaction is chosen to be the smallest among a series of values calculated from Equation (4.8). At the same time, the location for the next event is identified to be the reaction site μ where τ is chosen. The event type for the next reaction is "rupture" if the bond at site μ is currently closed and "rebinding" if it is currently open. Any change of bond state requires an update of bond force and surface separation in the elasticity part of the model, which is then used to determine the subsequent reaction rates. This coupling starts with the initial condition that all of the bonds within the adhesion domain are closed, and proceeds until all of the bonds are open. The total elapsed time is recorded as the cluster lifetime. The Monte Carlo simulation based on the above algorithm is equivalent to the original master equation as long as the number of trajectories is sufficiently large. To investigate the stability of molecular bond clusters in the presence of non-uniform bond force and surface separation, we adopt the following procedure:

1) Create an adhesion domain consisting of N_t uniformly distributed bonds. Record bond locations x_μ (reaction sites). All bonds are set to be "closed" at $\tau = 0$.
2) Solve for interfacial force distribution based on the discrete elastic equations in Chapter 3. Record forces F_i acting on each closed bond, and calculate surface separation δ_i at each open bond.
3) Calculate reaction rates a_μ for all reaction sites; $a_\mu = r_i$ for closed bonds and $a_\mu = g_i$ for open bonds.

4) Generate a set of independent random numbers ξ_ν , which are uniformly distributed over [0, 1], for individual reaction sites and insert them into Equation (4.8).

5) Read the smallest τ_ν and the corresponding site as the time and location of the next bond reaction.

6) Change bond state at selected site μ. The bond status at site μ is changed to "open" if it is currently "closed" and to "closed" if it is "open". Set $\tau = \tau + \mathrm{d}\tau$.

7) Go to step (2) and loop until all the bonds within the adhesion area are "open". Record the final τ for the lifetime of current trajectory.

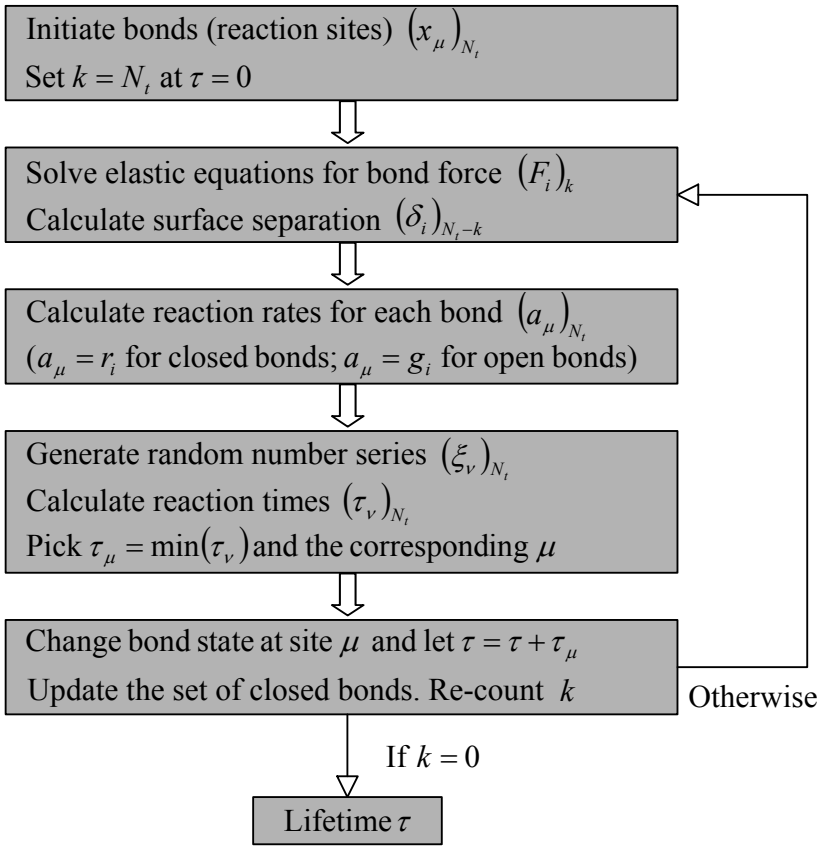

Figure 4.2: The flow chart of a Monte Carlo scheme coupling stochastic descriptions of molecular bonds and elastic descriptions of cell-substrate adhesion.

The flow chart of this coupled numerical procedure is illustrated in Figure 4.2. Many such trajectories are calculated to obtain the average lifetime of a bond cluster, denoted as T. We will discuss in the following chapters how the cluster lifetime is influenced by the applied load and will develop a strength theory of molecular bond clusters based on the simulation results.

4.4 Illustrative examples

We shall now present some applications of the Monte Carlo scheme. Let us begin with a molecular cluster under the assumption of equal load sharing, where the analytical solution of cluster lifetime is available. The selected model system has the following parameters:

$$k_{LR} = 0.25\,\text{pN/nm},\ b = 32\,\text{nm},\ l_b = 11\,\text{nm},\ F_b = 4\,\text{pN},\ \gamma = 100. \tag{4.14}$$

The validity of our numerical scheme is verified with some of the most fundamental theorems in probability theory.

Test 1: the law of large numbers (LLN)

The law of large numbers (LLN) [54] is a theorem in probability that describes the long-term stability of the mean of a random variable. Given a random variable with a finite expected value, such as the cluster lifetime T in our simulation, if its value is repeatedly sampled, as the number of these observations increases, the average will tend to approach and stay close to the expected value.

Consider a molecular cluster with $N_t = 20$ bonds subjected to a tensile load of $f = 0.52$. Here f is the nominal force sustained by individual bonds so that the total

applied force is $f \cdot N_t$ (after the normalization by F_b). Equation (2.22) predicts an analytical lifetime $T = 2.434$. The average cluster lifetime T from numerous Monte Carlo simulations is plotted as a function of the number of samples in Figure 4.3a. We see that the numerical average approaches and stays close to the analytical result (dashed line in the figure) as the number of samples increases. In Figure 4.3b, we report a series of cluster lifetimes for various cluster sizes and load levels. All of the lifetime values are based on the average of 1,000 independent trials. The results show excellent agreement with the analytical predictions.

Test 2: the central limit theorem (CLT)

The central limit theorem (CLT) [54] states that the distribution of the mean of many independent, identically distributed random variables tends towards the Gaussian distribution. In our case, the cluster lifetime T is a random variable following some unknown probability distribution (Figure 4.4a). Suppose that T has the mean μ_T and variance σ_T^2. According to the central limit theorem, if we consider $\overline{T}(n)$ to be the average of n independent numerical measurements of the cluster lifetime T, then as $n \to \infty$, $\overline{T}$ should obey a Gaussian distribution with the same mean μ_T and the variance σ_T^2/n.

Again for $N_t = 20$ and $f = 0.52$, the histogram of $\overline{T}(n)$ ($n = 200$) indeed shows a Gaussian-like distribution, as given in Figure 4.4b. We also plot the standard deviation (std) of $\overline{T}$ as a function of the averaging number n in Figure 4.4c. The linear fitting of $\log(\text{std})$ versus $\log(n)$ gives a negative slop of -0.49, which agrees well with the CLT prediction that $\text{std} \sim \sigma_T/\sqrt{n}$.

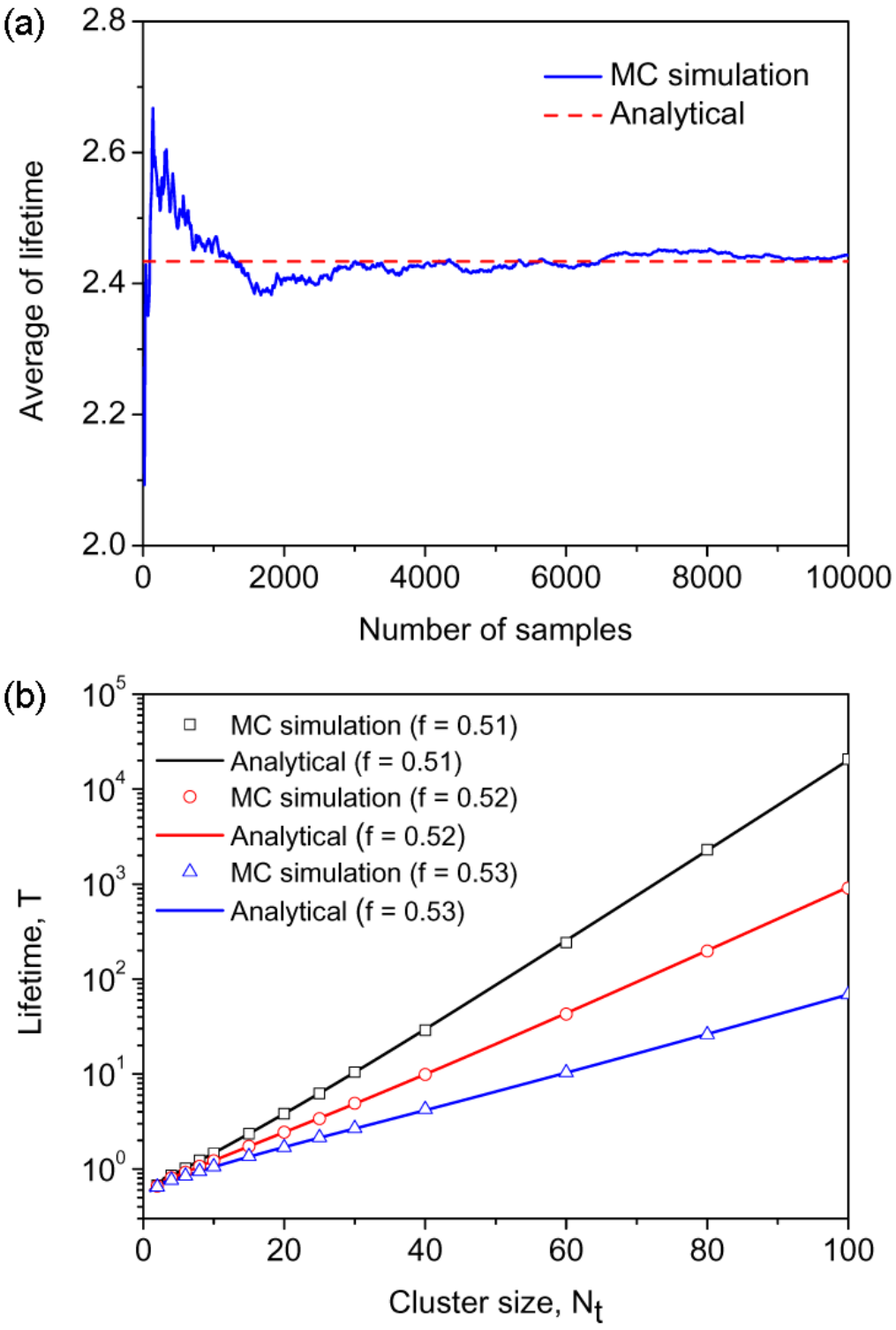

Figure 4.3: (a) The average cluster lifetime T as a function of the number of samples ($N_t = 20$ and $f = 0.52$). (b) The lifetime T of molecular bond clusters at various values of cluster size and load.

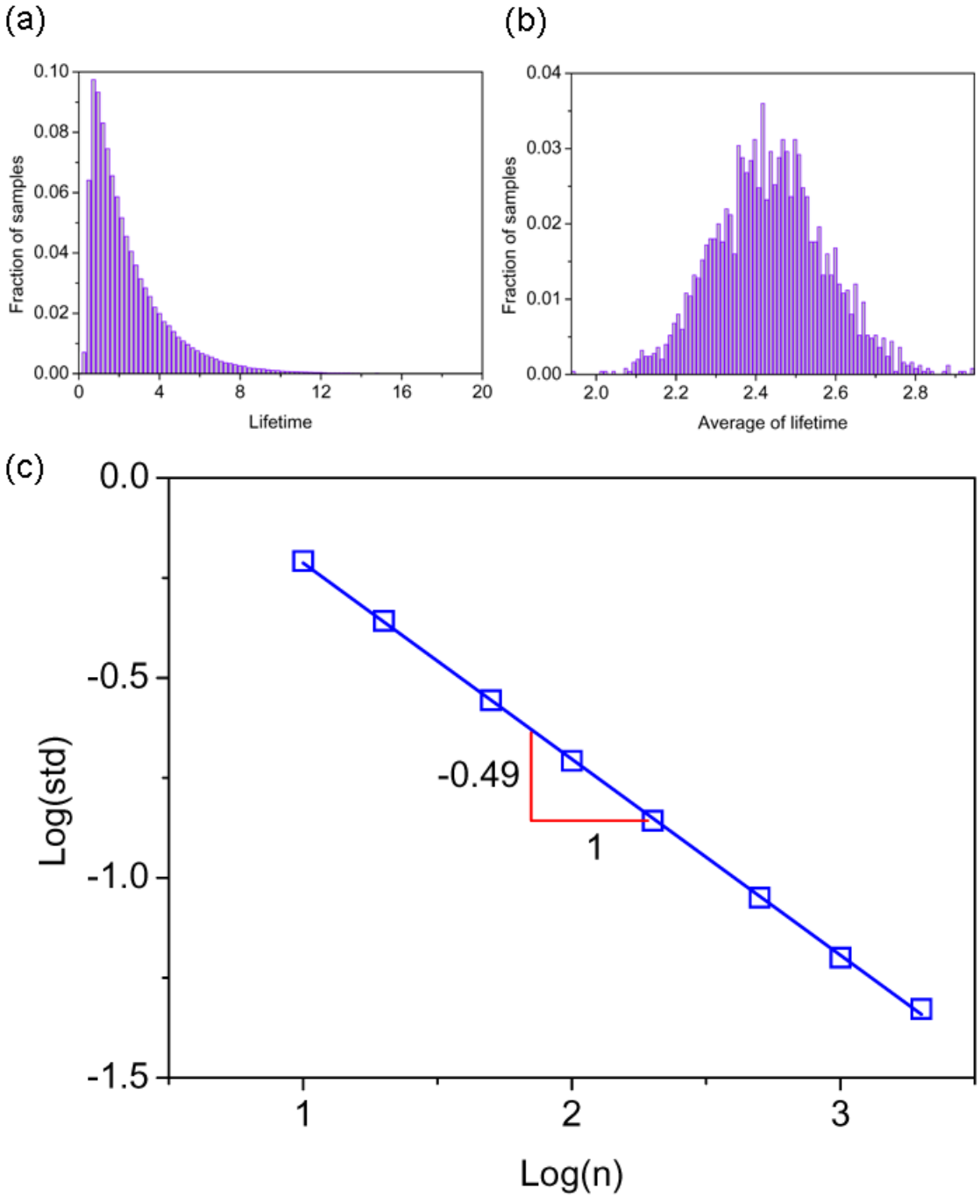

Figure 4.4: Histograms of (a) the cluster lifetime T and (b) the average of T ($n = 200$). (c) Standard deviation (std) of the average lifetime as a function of the sample number n.

Chapter 5

A single adhesion patch

5.1 Model description

The theoretical model under consideration is shown in Figure 5.1, where a cluster of receptor-ligand bonds establishes an adhesion patch of size $2a$ between two dissimilar elastic media under a remote force F [41]. Within the adhesion domain, a number of molecular bonds are fixed at an equal spacing of b, corresponding to a bond density of $\rho_{LR} = 1/b^2$. A slice of the system with out-of-plane thickness b is considered in a plane strain model. In this set-up, the total number of molecular bonds is $N_t = 2a/b$. All the bonds are closed initially and will undergo stochastic rupture and rebinding according to the prescribed rates in Equation (2.9). Each bond is modeled as a Hookean spring with stiffness k_{LR} and rest length l_b. Only specific adhesion via receptor-ligand linkages is considered and secondary non-specific interactions are ignored. One side of adhesion is an elastic medium mimicking the cytoskeleton of a cell and the other side represents an elastic substrate (ECM or another cell). The Young's modulus and Poisson's ratio are E_C, ν_C for the cell and E_S, ν_S for the substrate.

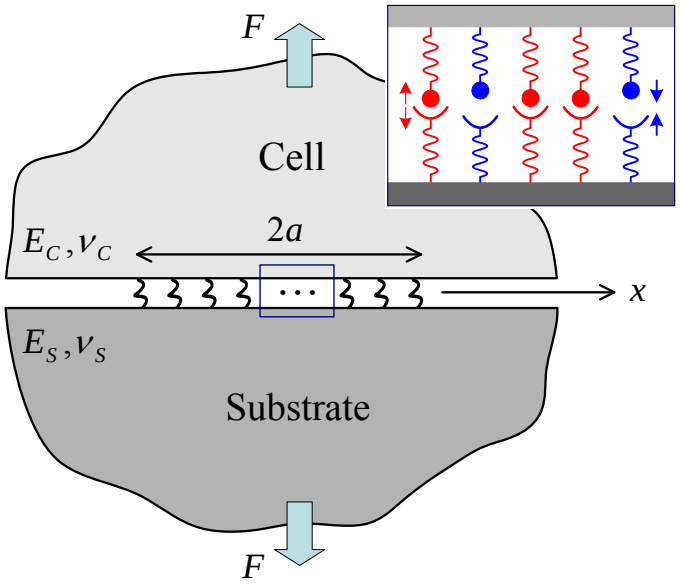

Figure 5.1: Schematic illustration of an idealized theoretical model of adhesion between two elastic bodies via a cluster of receptor-ligand bonds under a remote force F. The bond cluster has size $2a$. One side of adhesion is an elastic medium with Young's modulus E_C and Poisson's ratio ν_C mimicking cell body, and the other side is a substrate with different elastic properties E_S and ν_S.

5.2 Cluster strength and lifetime: size and modulus effects

We first simulate the lifetime of a focal adhesion cluster shown in Figure 5.1 which consists of 40 bonds under different levels of applied load. The spacing between neighboring bonds is set at $b = 32$ nm, corresponding to a bond density around $1000\,\mu\text{m}^{-2}$. We assign $E^* = 10\,\text{KPa}$ as the reduced elastic modulus of the cell and substrate. The receptor-ligand bond stiffness, k_{LR}, is taken to be $0.25\,\text{pN/nm}$ following an estimate for the fibronectin-integrin bond [39]. Under these parameters, the stress concentration index α is calculated to be about 16, which implies a severe stress concentration at the edges of adhesion. The force scale F_b is fixed at $4\,\text{pN}$ [20,21], and the half-width a_0 of each bond is taken as 5 nm [48]. We set $\gamma = 1$ for the factor of

rebinding rate [39,40] and $l_b = 11\,\text{nm}$ for the bond rest length [55]. These parameters are summarized in Table 5.1. We simulate the cluster lifetime T by imposing different levels of the applied load on the adhesion patch. Figure 5.2a plots some representative simulation trajectories for three different levels of the apparent stress, i.e. $F/2ab$. Reducing the applied load generally stabilizes the cluster and leads to longer cluster lifetime. The average lifetime over two hundred trajectories is plotted as a function of the apparent stress $F/2ab$ in Figure 5.2b. We see that the lifetime asymptotically approaches "infinity" as $F/2ab$ decreases to below a critical value. Load levels larger than this critical value dramatically decrease the average lifetime and cause the cluster to be unstable. We define the cluster strength $F_{cr}/2ab$ as the critical load level at which the cluster lifetime asymptotically approaches infinity. In numerically determining the cluster strength, we pick $T_\infty = 100$, i.e. 100-fold prolongation of the single bond lifetime at zero force ($1/k_0$). Once the average survival time of a cluster exceeds T_∞, we say that the cluster is stable under the corresponding load, and the critical load corresponding to T_∞ is defined as the cluster strength. We point out that the cluster strength based on this prescribed time scale depends on the selected value of T_∞, but the dependence is weak because the lifetime-load curves for molecular bond clusters generally exhibit very large slope near the critical load. We find that, at the critical load corresponding to $T_\infty = 100$ in Figure 5.2b, a further reduction of merely ~2% in load would double the lifetime. Therefore, we believe that a different selection of T_∞, say $T_\infty = 1000$, will only lead to a minor change in the predicted strength values.

Table 5.1: List of parameters used in the coupled Monte Carlo simulations of a single adhesion patch

Parameters	Values
Number of total bonds, N_t	2 – 100
Spacing between neighboring bonds, b (nm)	32
Focal adhesion size, $2a$ (μm)	0.064 – 3.2
Receptor-ligand bond density, ρ_{LR} (μm^{-2})	~1000
Single bond stiffness, k_{LR} (pN/nm)	0.25
Reduced elastic modulus, E^* (KPa)	1 – 1000
Factor of rebinding rate, γ	1 – 100
Rest length of bond, l_b (nm)	11
Force scale in bond dissociation, F_b (pN)	4
Radius of individual bonds, a_0 (nm)	5

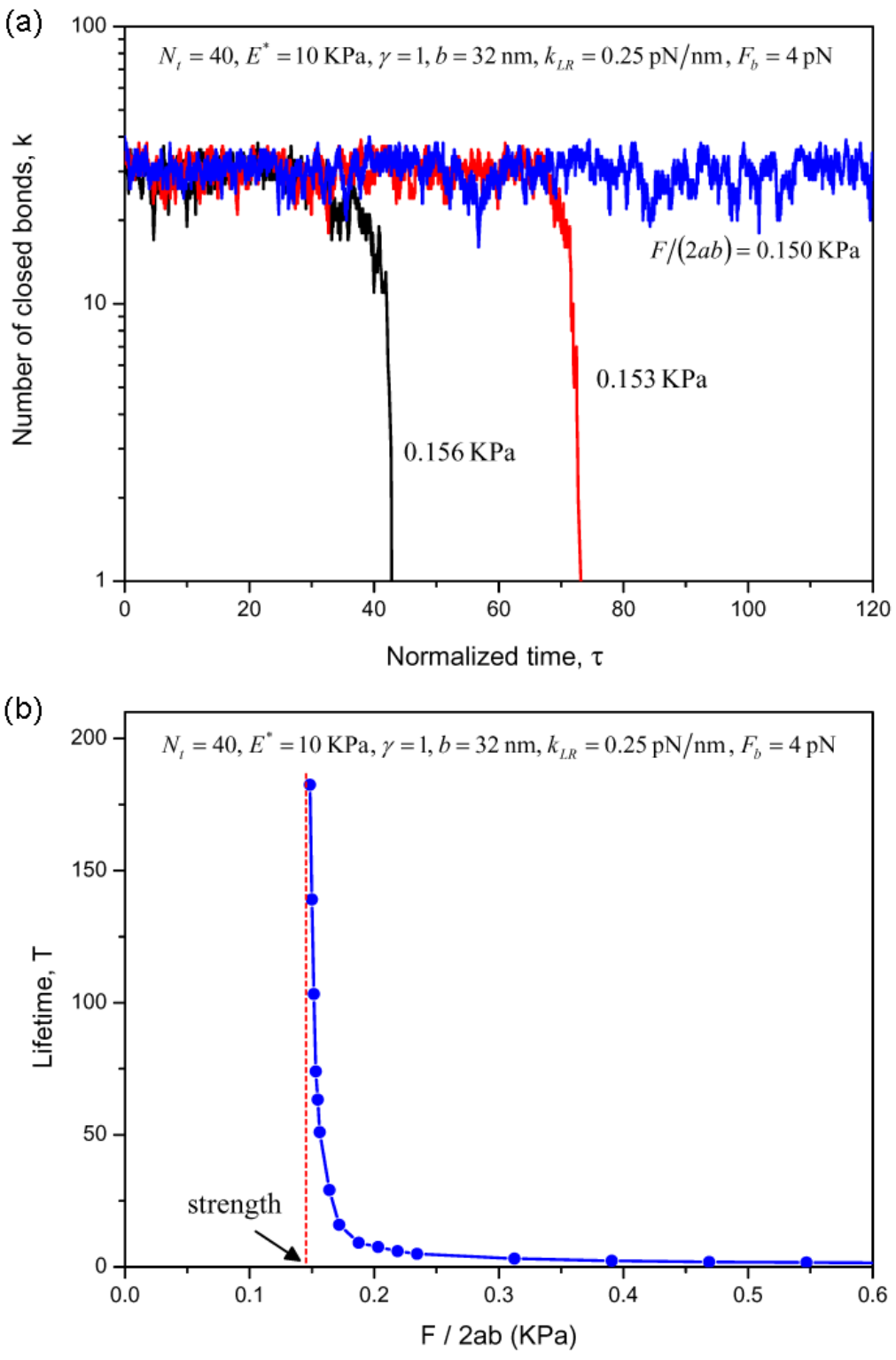

Figure 5.2: (a) Representative simulation trajectories of a molecular bond cluster with fixed size evolving under three different levels of applied load. (b) Average lifetime of the cluster as a function of the applied load. The lifetime asymptotically approaches infinity as the load reaches a critical value defined as the cluster strength.

To investigate the size effects on the cluster strength, we have performed a series of Monte Carlo simulations by varying the number of bonds from 2 to 100. For the chosen bond spacing $b = 32\,\text{nm}$, the adhesion domain under investigation has its size ranging from 64 nm to $3.2\,\mu\text{m}$. We consider different values of the reduced elastic modulus E^* between 1 KPa and 1 MPa. The rebinding rate factor γ is set to be 1.0. In the results drawn in Figure 5.3a, we observe that clusters smaller than 4 bonds possess limited lifetime even in the absence of the applied load, similar to the behavior of a single bond. Their strength values are therefore considered to be zero. Clusters larger than 4 bonds begin to exhibit long-term stability under a finite load due to the collective effects of clustering. At a fixed cluster size, increasing the reduced elastic modulus generally results in stronger and more stable adhesion. This can be understood from the point of view that high elastic modulus decreases the stress concentration index α toward the regime of uniform interfacial traction. At $E^* = 1\,\text{MPa}$, the cluster strength monotonically increases with the growing cluster size within the investigated size range, which is similar to the results based on the equal-load-sharing assumption considered by Erdmann and Schwarz [20,21], which essentially corresponds to a cluster of molecular bonds between two rigid bodies ($E^* = \infty$). The stress concentration index α is 4 for $N_t = 100$ and $E^* = 100\,\text{KPa}$, suggesting a moderate stress concentration near the patch edges. Our simulation results suggest that this extent of non-uniform force distribution has induced crack-like failure of the cluster, as reflected by the fact that the cluster strength decreases with increasing cluster size. The effects of stress concentration are more pronounced for lower values of the reduced elastic modulus, as indicated by the curves for $E^* = 10\,\text{KPa}$ and $E^* = 1\,\text{KPa}$ in Figure 5.3a.

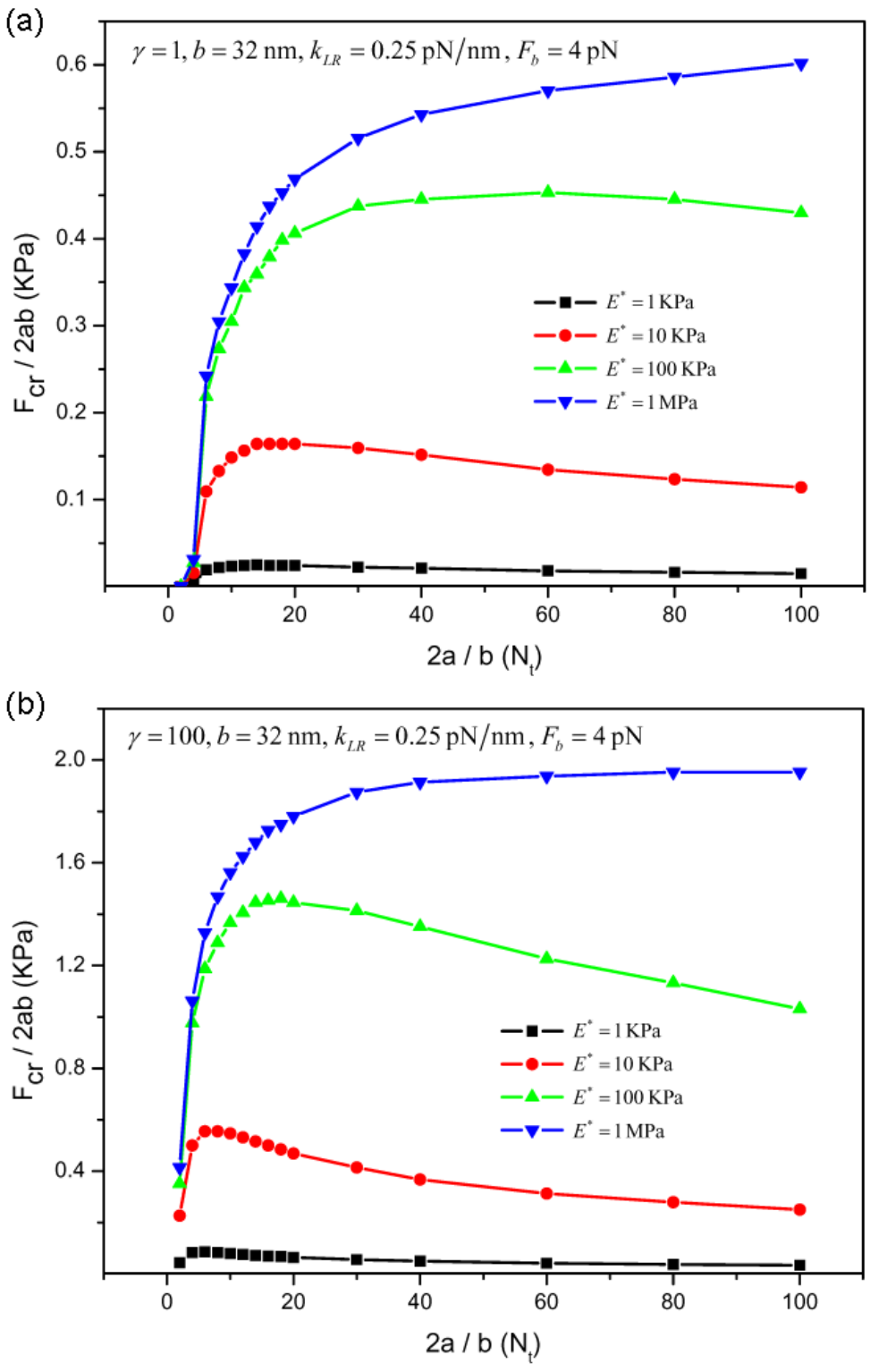

Figure 5.3: The strength of molecular bond cluster as a function of the cluster size N_t for different values of the reduced modulus E^* from 1 KPa to 1 MPa. The factor of rebinding rate, γ, is taken as (a) $\gamma = 1$ and (b) $\gamma = 100$.

In Figure 5.4, we plot the cluster lifetime T as a function of the cluster size N_t for different values of the normalized cell/substrate modulus $\kappa = E^* b / k_{LR}$. Here the applied load is represented by the nominal force sustained by individual bonds, f, which is an alternative form of the apparent stress $F/2ab$ discussed above because

$$\frac{F}{2ab} = \frac{f \cdot F_b}{b^2}. \tag{5.1}$$

The value of f is selected as 0.51 for the calculations shown in Figure 5.4a, 0.52 in 5.4b and 0.53 in 5.4c. In our Monte Carlo simulations, N_t is varied from 1 to 100, which covers adhesion clusters up to $3.2\,\mu\text{m}$ for the chosen bond spacing $b = 32\,\text{nm}$, and the normalized modulus $\kappa = E^* b / k_{LR}$ is from 1.28 to 1.28×10^4, corresponding to E^* values between 10 KPa and 100 MPa ($k_{LR} = 0.25\,\text{pN/nm}$). The prefactor of rebinding rate, γ, is fixed at 100. We observe that, for stiff cell/substrate with κ values larger than 1.28×10^3, the cluster lifetime T monotonically increases with growing cluster size N_t, which is also close to the analytical results for molecular clusters between rigid media ($\kappa = \infty$). However, for soft cell/substrate with κ values smaller than 1.28×10^2, with increasing cluster size N_t, T firstly increases due to the effects of bond cooperation, but eventually decreases due to strong stress concentration at the cluster edges.

At a fixed cluster size N_t, increasing the reduced elastic modulus E^* generally strengthens and stabilizes the clusters, which is consistent with the expected behavior from the stress concentration point of view based on the index α. For the range of E^* values discussed in our simulations, the cluster lifetime can change by more than 4 orders of magnitude dependent on the elasticity of the system.

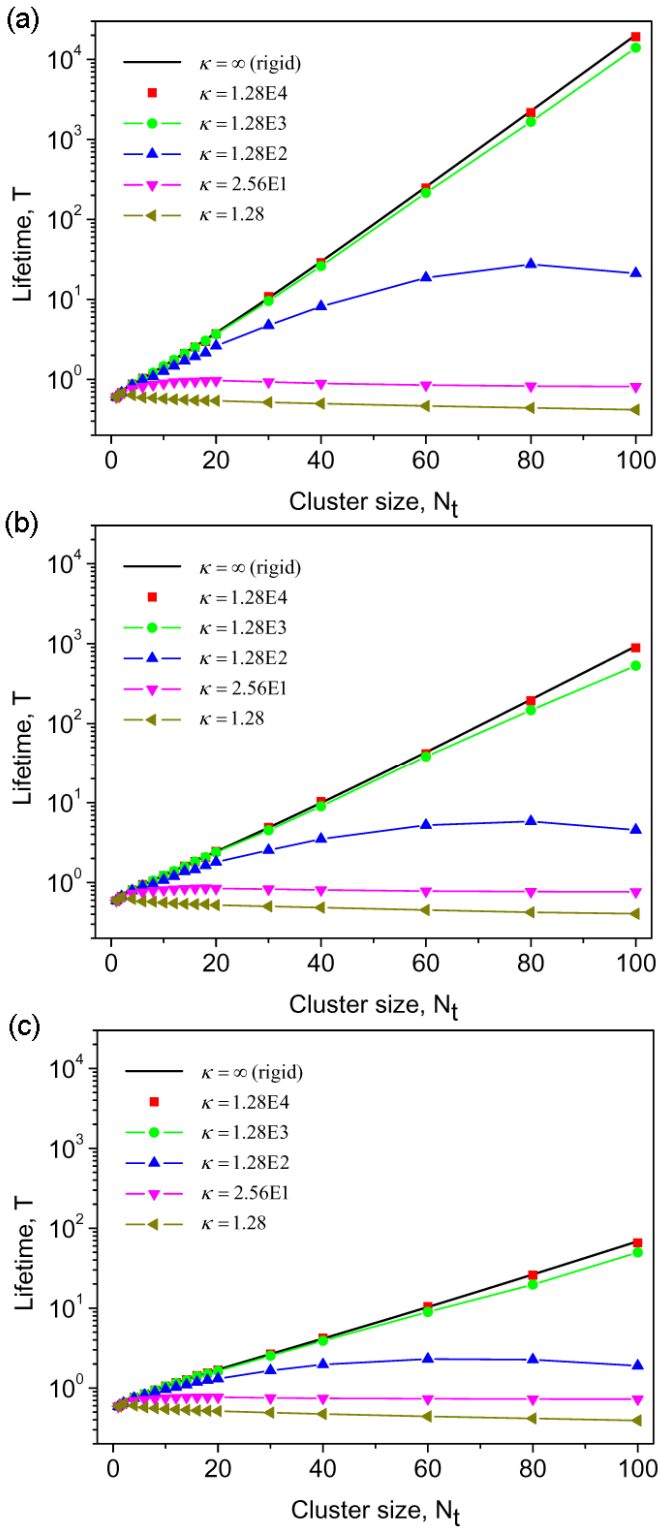

Figure 5.4: The lifetime T of molecular bond cluster as a function of the cluster size N_t for different values of the reduced modulus E^* ($\kappa = E^* b / k_{LR}$). (a) $f = 0.51$; (b) $f = 0.52$; (c) $f = 0.53$.

5.3 Influence of rebinding rate on cluster strength

We notice that the calculated strength values in Figure 5.3a are quite low under the selected parameters, e.g. ~0.4 KPa for $N_t = 100$, $E^* = 100$ KPa and $\gamma = 1$, corresponding to a load level of 0.4 pN per bond. In recognizing the exponential dependence of bond dissociation rate on the applied force, we expect that the rupture rate will be significantly enhanced at the adhesion edges by elevated stress level. This effect will be more pronounced especially at higher load levels at which the cluster strength should also become more sensitive to the reduced elastic modulus and adhesion size.

Higher rebinding rate makes the cluster to become stronger and therefore causes the cluster strength to be more sensitive to the reduced elastic modulus and adhesion size. To confirm this, we consider a different type of molecular bonds with higher affinity, $\gamma = 100$. All the other parameters remain the same as in the case of $\gamma = 1$. Figure 5.3b plots the cluster strength as a function of the adhesion size when the reduced elastic modulus is chosen between 1 KPa and 1 MPa. This selected rebinding rate provides a stronger stabilizing effect on the bond cluster and, as a result, clusters as small as 2 bonds can achieve long-term lifetime at a finite force. In this case, the bond strength is indeed more sensitive to the reduced elastic modulus of the system and to the adhesion size. At a fixed cluster size, increasing E^* tends to stabilize and strengthen the cluster by removing stress concentration from the adhesion edges. The cluster strength also shows strong size effects. For the curve corresponding to $E^* = 100$ KPa in Figure 5.3b, there is an optimal size around 20 bonds that gives rise to a maximum cluster strength. Clusters larger than this size are less stable because crack-like failure occurs due to large stress concentration near the adhesion edges. The curves for $E^* = 10$ KPa and $E^* = 1$ KPa show similar

behaviors with a maximum cluster strength at an optimal adhesion size. For the curve of $E^* = 1\,\text{MPa}$ in Figure 5.3b, including that in Figure 5.3a, our simulations did not capture an optimal size as we have limited our simulations to clusters smaller than 100 bonds. We believe that sufficiently large clusters will eventually encounter severe stress concentration and present catastrophic crack-like failure from their edges. The concept of an optimal adhesion size for the maximum cluster strength should be a general feature of molecular adhesion due to the statistical effects at small scale and crack-like failure at large scale. The effects of adhesion size and elastic modulus on the cluster strength can be explained based on the stress concentration index α: increasing adhesion size or decreasing elastic modulus tend to increase α toward the regime of crack-like stress concentration, hence reduce the stability and strength of the clusters.

5.4 Size window for stable adhesion

The maximum cluster strength at an optimal adhesion size serves as a critical threshold for stable adhesion. Stress levels higher than this value destabilize the clusters to the regime of limited lifetime for clusters of any size. For a non-zero applied load below the threshold, there exists a size window for stable adhesion. Molecular clusters within this size window have their strength values higher than the applied load, and clusters out of the window have their strength values lower than the load. Based on the definition of cluster strength, clusters within the size window can achieve long-term stability and clusters outside the window will have limited lifetime. It is therefore interesting to plot the cluster lifetime T as a function of the adhesion size at a fixed load, as shown in

Figure 5.5. We firstly replot in Figure 5.5a the curve of $E^* = 10$ KPa in Figure 5.3b for a closer examination of the size effect on cluster strength. In this calculation, we take an apparent stress of 0.53 KPa. Figure 5.5b plots some representative simulation trajectories for three cluster sizes under this fixed load. We see that a prolonged lifetime is only possible for clusters around 10 bonds. Smaller clusters are not stable because the number of bonds is insufficient to achieve long term stability and the behavior of the clusters is similar to a single bond. On the other hand, larger clusters are also limited in lifetime due to the elasticity-induced stress concentration which tends to focus the action on a small number of bonds near the adhesion edges. The average lifetime of molecular bond clusters is plotted in Figure 5.5c as a function of the adhesion size. The results clearly display a size window beyond which molecular clusters cannot achieve long-term stability under the present load. The corresponding results based on the assumption of equal load sharing would show a monotonously increasing cluster lifetime with growing cluster size. In contrast, our results show that a prolonged lifetime is only possible for clusters with intermediate size as soon as the cell/substrate elasticity is considered. The assumption of equal load sharing adopted by Erdmann and Schwarz [20,21] is approximately valid only for a limited range of elastic modulus and adhesion size, while non-uniform distributions of bond force and surface separation are a general rule. Small adhesion leads to single-molecule-like behavior due to the statistic effects while large adhesion also leads to single-molecule-like behavior due to the focusing effect of stress concentration which confines the bond rupture/dissociation events to a smaller number of bonds near the adhesion edges.

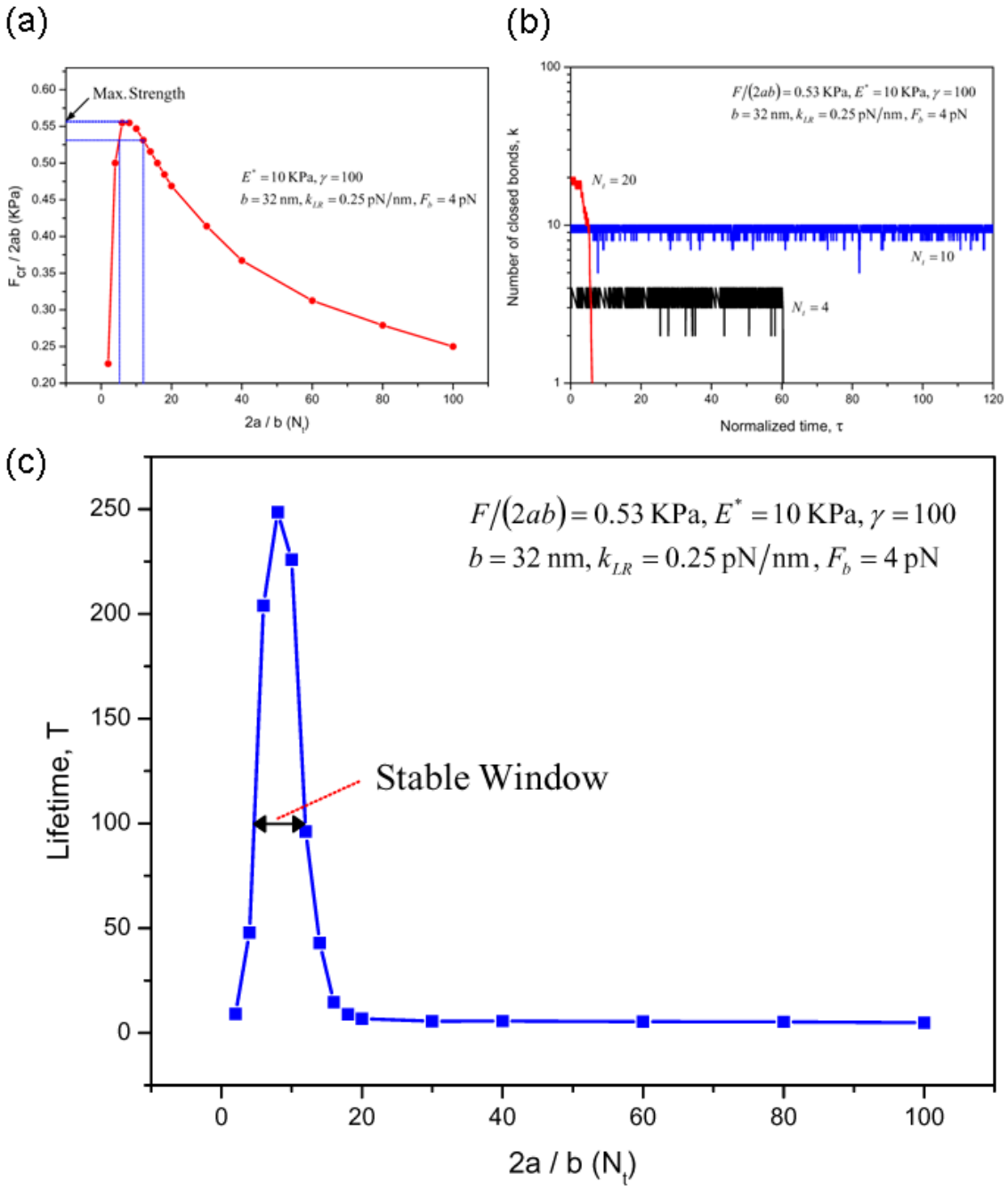

Figure 5.5: (a) The strength of molecular bond cluster as a function of the patch size N_t for $E^* = 10$ KP and $\gamma = 100$. (b) Representive simulation trajectories for three different cluster sizes under a fixed load of 0.53 KPa. (c) The lifetime T as a function of the adhesion size N_t at the fixed load. The results show a size window beyond which clusters cannot achieve long-term stability.

Although we do not expect that the highly idealized stochastic-elasticity model considered in this work can capture the complexity of real focal adhesions, it seems that our analysis still provides some feasible explanations for a range of experimental observations. First of all, our model shows that increasing the reduced elastic modulus of cell and substrate helps to stabilize multiple adhesion bonds by removing stress concentration from the adhesion domain. This is at least in qualitative agreement with the observations that stable and large FAs are only formed on sufficiently rigid substrates. The definition of the reduced elastic modulus in Equation (3.1) implies that very soft substrates will dominate over the property of cell in that crack-like interfacial traction will persist irrespective of the stiffness of cytoskeleton, which may prevent shortly lived focal complexes from maturing into large FAs. On hard substrates, the reduced elastic modulus tends to be dominated by the stiffness of cytoskeleton. This would allow the cell to actively control adhesion/de-adhesion via regulating cytoskeleton stiffness by the contractile forces in stress fibers connecting to an FA. Our model also provides a simple answer to the question why FAs usually fall into a narrow size range from a few hundred nm to a few microns. Small adhesions are unstable due to the statistical nature of molecular bonds. There exists a lower size limit for the transition from single-molecule-like behavior to stable cluster. However, the growth of adhesion patch ultimately leads to crack-like interfacial traction, hence an upper size exists. These results are all qualitatively consistent with relevant experimental observations. We conclude that rigid substrate, cytoskeleton stiffening via contractile forces and intermediate adhesion size should contribute to stable cell adhesion while soft substrate, cytoskeleton softening by dissolution of actin network and extreme adhesion size tend to destabilize cell adhesion.

5.5 Lifetime of bond clusters under initially uniform force distribution

So far we have discussed the lifetime and strength of molecular bond clusters under pre-existing stress concentration at the cluster edges. To exclude the effects of this initial non-uniform stress distribution within the cluster, we have performed a parallel study in which a uniform tensile stress P is applied directly along the interface. Instead of a remotely applied force F which tends to induce a non-uniform distribution of bond forces within the cluster, the uniformly applied stress P at the interface ensures that all the molecular bonds are subjected to equal force at the initial state, as modeled in Section 3.4. Figure 5.6 shows the cluster lifetime T as a function of the cluster size N_t for different values of the normalized modulus $\kappa = E^* b / k_{LR}$. We enforce the condition that $F = P \cdot 2ab$ so that the nominal force sustained by individual bonds is identical for the two cases. All the other parameters used in Figure 5.6 remain the same as those in Figure 5.4. By comparing the plots, we find that the molecular clusters generally have longer lifetime in the absence of pre-existing stress concentration. For very stiff cell/substrate with κ values higher that 1.28×10^3, both cases are closed to the analytical results for clusters between rigid media and the lifetime monotonically increases with growing cluster size. However, for very soft cell/substrate with κ values smaller than 25.6, the cluster lifetime T is reduced by several orders of magnitude and T firstly increases but eventually decreases with increasing cluster size. This size effect is less strong compared to that in Figure 5.4 because of the exclusion of pre-existing stress concentration. At a fixed cluster size N_t, increasing the reduced elastic modulus E^* is always favorable from a stability point of view.

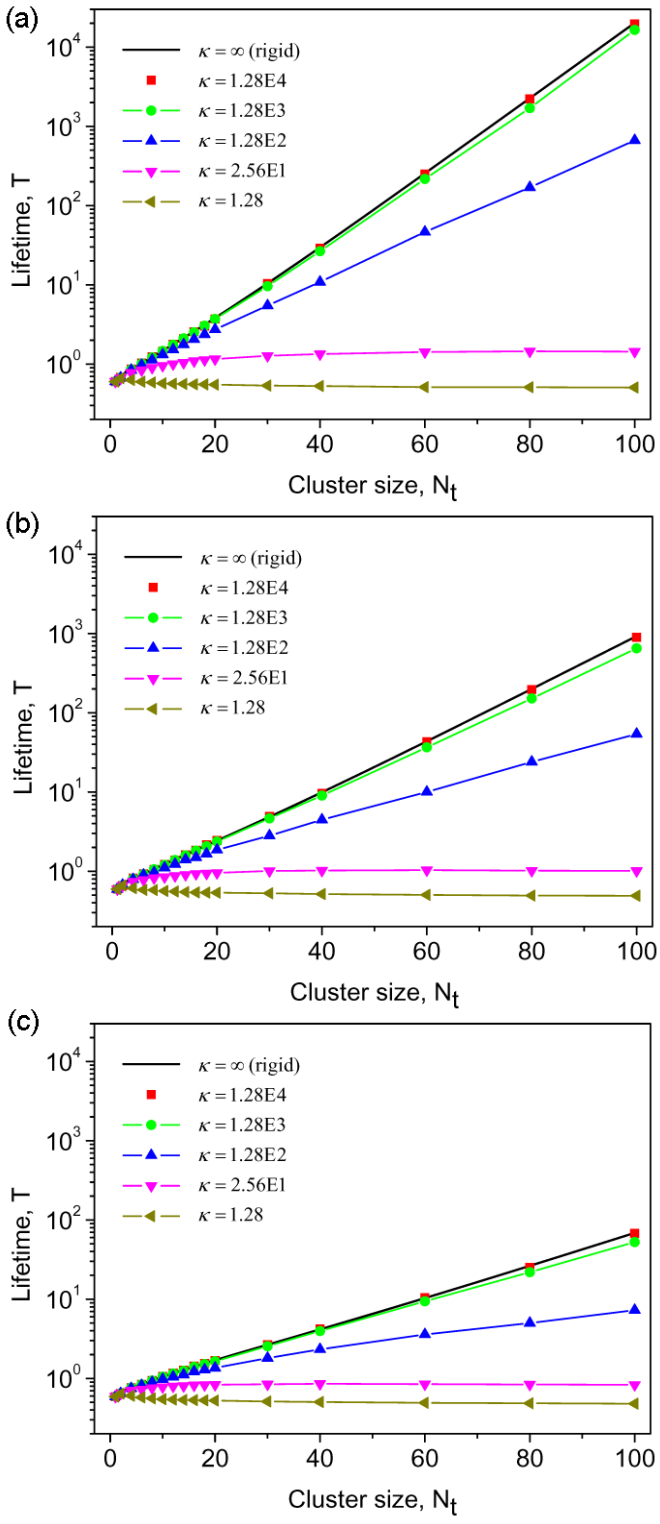

Figure 5.6: The cluster lifetime T as a function of the cluster size N_t for different values of the reduced modulus E^* ($\kappa = E^* b / k_{LR}$). The bond cluster is subjected to initially uniform force. (a) $f = 0.51$; (b) $f = 0.52$; (c) $f = 0.53$.

5.6 Upper and lower bounds of cluster lifetime

From previous simulations, we observe that molecular clusters become more and more stable as cell and ECM stiffen. In this sense, the lifetime of a cluster between rigid bodies, given by Equation (2.22), can be viewed as the upper bound of lifetime for a molecular cluster between elastic media, i.e.

$$T(N_t)=\sum_{k=1}^{N_t}\frac{1}{r_k}+\sum_{i=1}^{N_t-1}\sum_{j=i+1}^{N_t}\frac{\prod_{k=j-i}^{j-1}g_k}{\prod_{k=j-i}^{j}r_k}, \tag{5.2a}$$

$$r_k=k\exp\left(fN_t/k\right),\ g_k=\left(N_t-k\right)\cdot 2\gamma\sqrt{\frac{\beta}{\pi}}\frac{\exp\left(-\beta(\Delta-L_b)^2\right)}{\operatorname{erf}\left((\Delta-L_b)\sqrt{\beta}\right)+\operatorname{erf}\left(L_b\sqrt{\beta}\right)}. \tag{5.2b}$$

Note that the surface separation in Equation (5.2b) is computed by $\Delta=L_b+\frac{f\cdot N_t}{k}\frac{F_b}{k_{LR}b}$.

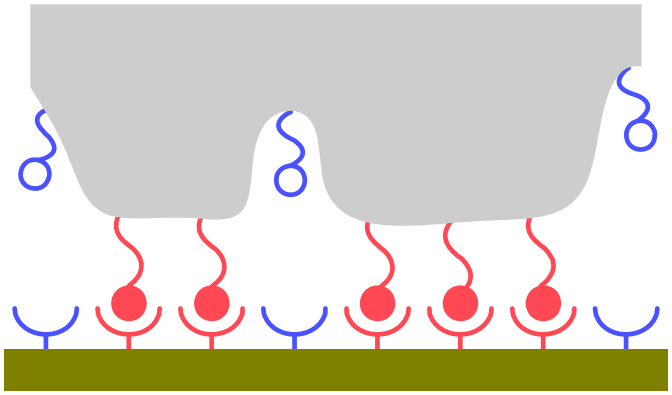

Figure 5.7: Schematic illustration of bond rupture in the absence of rebinding. Note the elastic recoil where open bonds locate.

The elastic deformation of cell and ECM reduces the cluster lifetime by two means: decreasing rebinding probability and increasing stress concentration. The rebinding, dependent on surface separation, is generally diminished due to the elastic recoil where

open bonds locate, as illustrated in Figure 5.7. For very soft cell/ECM, the surface separation at open bond locations is so large that rebinding becomes hardly possible. Disallowance of rebinding under equal load sharing in Equation (2.22) gives

$$T(N_t)=\sum_{k=1}^{N_t}\frac{1}{k\exp(fN_t/k)}. \tag{5.3}$$

For a molecular cluster between very soft cell and substrate ($E^*=10\,\text{kPa}$) under a load level of $f=0.51$, we see that Equation (5.3) in the absence of rebinding immediately drags T to the right order of magnitude (dashed line in Figure 5.8).

On the other hand, the cell/ECM elasticity also induces stress concentration within an adhesion cluster. For extremely soft cell/ECM, one can regard the failure of an adhesion cluster as the process that each bond sequentially breaks starting from the one at edges. We assume that the bond forces obey the following distribution:

$$f_i=\frac{f\cdot N_t}{k}\left(\frac{1}{2}(3c_f-3)X_i^2+\frac{1}{2}(3-c_f)\right),\quad X_i\in[-1,1], \tag{5.4}$$

where the prefactor $f\cdot N_t/k$ is the average force sustained by individual closed bonds, and c_f is the stress concentration factor at the cluster edges, which depends on the stress concentration index α in Figure 3.3. The k closed bonds are uniformly distributed within the adhesion domain $[-1,1]$, so that their coordinates are

$$X_i=\frac{2i}{k-1}-\frac{k+1}{k-1},\quad i\in[1,2,\cdots,k]. \tag{5.5}$$

Inserting Equation (5.5) into (5.4) gives all the bond forces within the adhesion domain. The cluster lifetime in the absence of rebinding is therefore

$$T(N_t) = \sum_{k=1}^{N_t} \frac{1}{r_k}, \tag{5.6a}$$

where the rupture rate

$$r_k = \sum_{i=1}^{k} e^{f_i} \tag{5.6b}$$

can be calculated with the bond forces in Equation (5.4). This provides a lower bound estimate of the lifetime for molecular clusters between very soft cell and substrate, as plotted by the solid line in Figure 5.8.

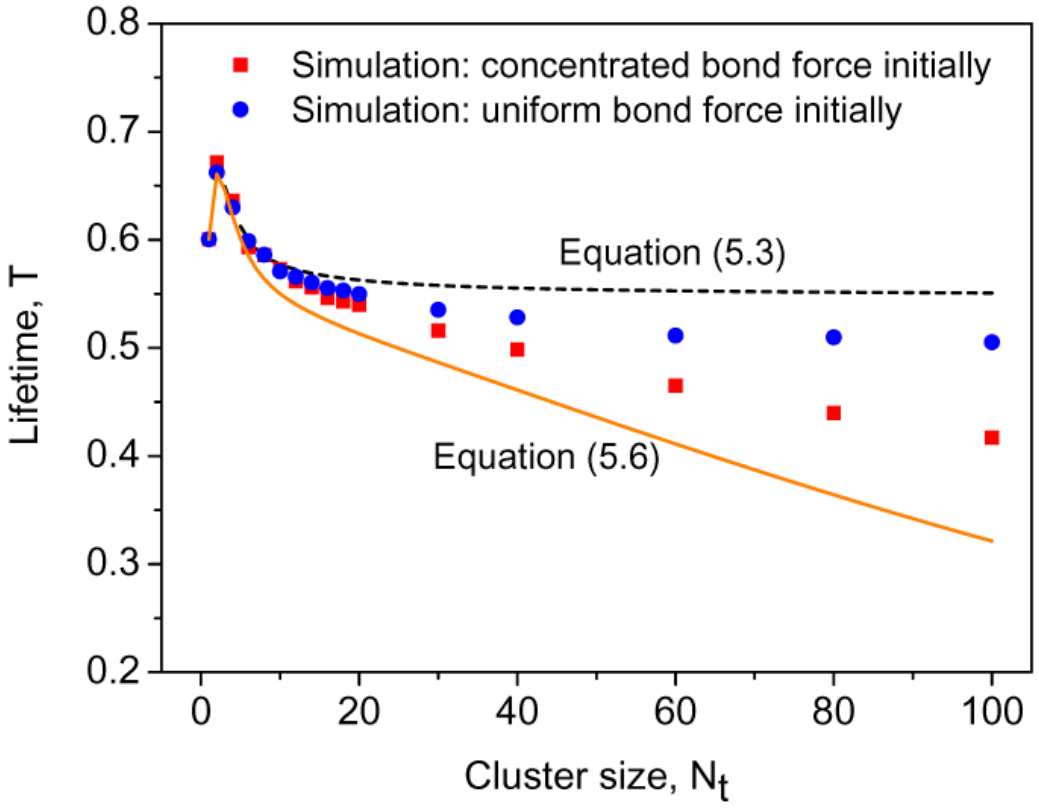

Figure 5.8: Lower bound estimate of the cluster lifetime compared to the simulation results for very soft cell and substrate ($E^* = 10$ KPa and $f = 0.51$).

Chapter 6

Periodic adhesion clusters

6.1 Model description

The system under investigation involves a periodic array of adhesion clusters of molecular bonds between two dissimilar elastic media subjected to a tensile stress σ_∞ applied at an inclined angle θ with respect to the cell-ECM interface, as shown in Figure 6.1. All the molecular bonds are closed at the initial state and they can statistically transit between open (broken) and closed (linked) states as described in Equation (2.9). Both cell and substrate are modeled as semi-infinite elastic media with Young's modulus and Poisson's ratio E_C, ν_C and E_S, ν_S, respectively. A reduced elastic modulus E^* is defined in Equation (3.1) according to the convention of contact mechanics. We consider the situation that the interfacial adhesion arises solely from the receptor-ligand bonds modeled as Gaussian chains having a finite stiffness k_{LR} and zero rest length. The bonds are grouped in adhesion clusters of size $2a$ which are periodically distributed at a period of $2c$ along the interface. Within each cluster, individual molecular bonds are uniformly distributed at a spacing of b, corresponding to a bond density of $\rho_{LR} = 1/b^2$. For

simplicity, we consider a slice of the system with out-of-plane thickness b, corresponding to the so-called plane strain problem in theory of elasticity. The apparent bond density along the entire interface is $\bar{\rho}_{LR} = a\rho_{LR}/c$.

We notice that the present problem can be considered a combination of the bond dynamics obeying the master equation [42] and the periodic crack model in interfacial fracture mechanics [56]. In the absence of molecular bonds, our model is reduced to a periodic array of cracks between two elastic media and in the limit of rigid media it is reduced to the type of cluster model discussed in Section 2.4.

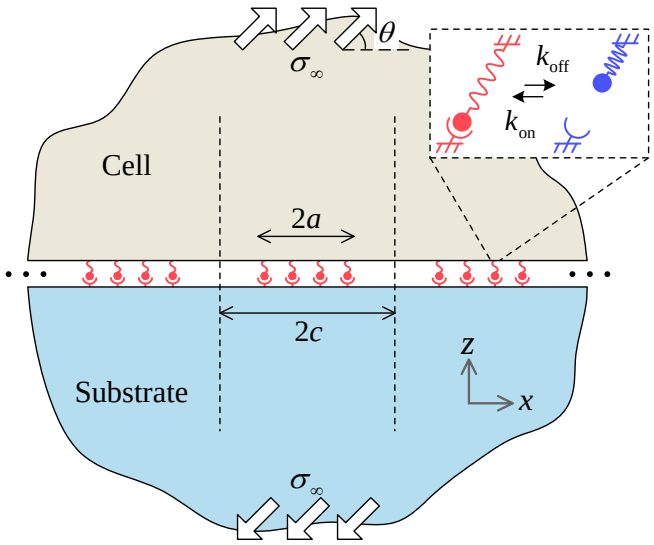

Figure 6.1: Schematic illustration of a periodic array of adhesion clusters between two dissimilar elastic media under an inclined tensile stress.

Due to the periodic nature of the problem, we focus our attention on one cluster and adopt a set of coordinates (x, z) with directions shown in Figure 6.1 and origin located at the center of the cluster. In the present plane strain model, the total number of bonds within the cluster is $N_t = 2a/b$.

The coupling between system elasticity and stochastic events starts at the initial state when all the bonds within the adhesion domain are assumed closed and the process proceeds until all the bonds become open. The total elapsed time T is recorded as the lifetime of the adhesion. The statistical average of lifetime is obtained from an average of 200 simulated trajectories. For relevant physical/biological parameters used in the simulation, we adopt the following typical values: $b = 32\,\text{nm}$, $c/a = 2$, $k_{LR} = 0.25\,\text{pN/nm}$, $F_b = 4\,\text{pN}$, $k_{\text{on}}^0/k_0 = 3200$ and $l_{\text{bind}} = 1\,\text{nm}$, unless stated otherwise.

6.2 Size window for stable adhesion influenced by cell/matrix stiffness

The lifetime T of the periodic clusters is shown in Figure 6.2 as a function of the cluster size N_t for different values of the reduced elastic modulus E^* between 1 KPa and 300 KPa. Here the loading angle θ is fixed at 45°. The simulation results indicate that there exists a "size window" for stable adhesion. In all cases, the traction distribution along the cell-ECM interface is non-uniform and the failure becomes increasingly crack-like at increasing cluster size. Very small clusters resemble single molecule behavior with limited lifetime and large clusters fail by stress concentration near the adhesion edges. Increasing the reduced elastic modulus tends to stabilize and strengthen the adhesion by alleviating stress concentration within the FA domain. We observe that the size window of stable adhesion shifts and broadens as the cell and substrate stiffen. This can be understood from the point of view that large values of E^* decreases the stress concentration index $\overline{\alpha}$ (in Chapter 3) toward the regime of uniform interfacial traction. The concept of a size window for stable adhesion is similar to our previous study on a

single cluster under normal tensile load and should be a general feature of molecular adhesion clusters between elastic media because stochastic effects are expected to dominate at small scales and crack-like failure dominates at large scales.

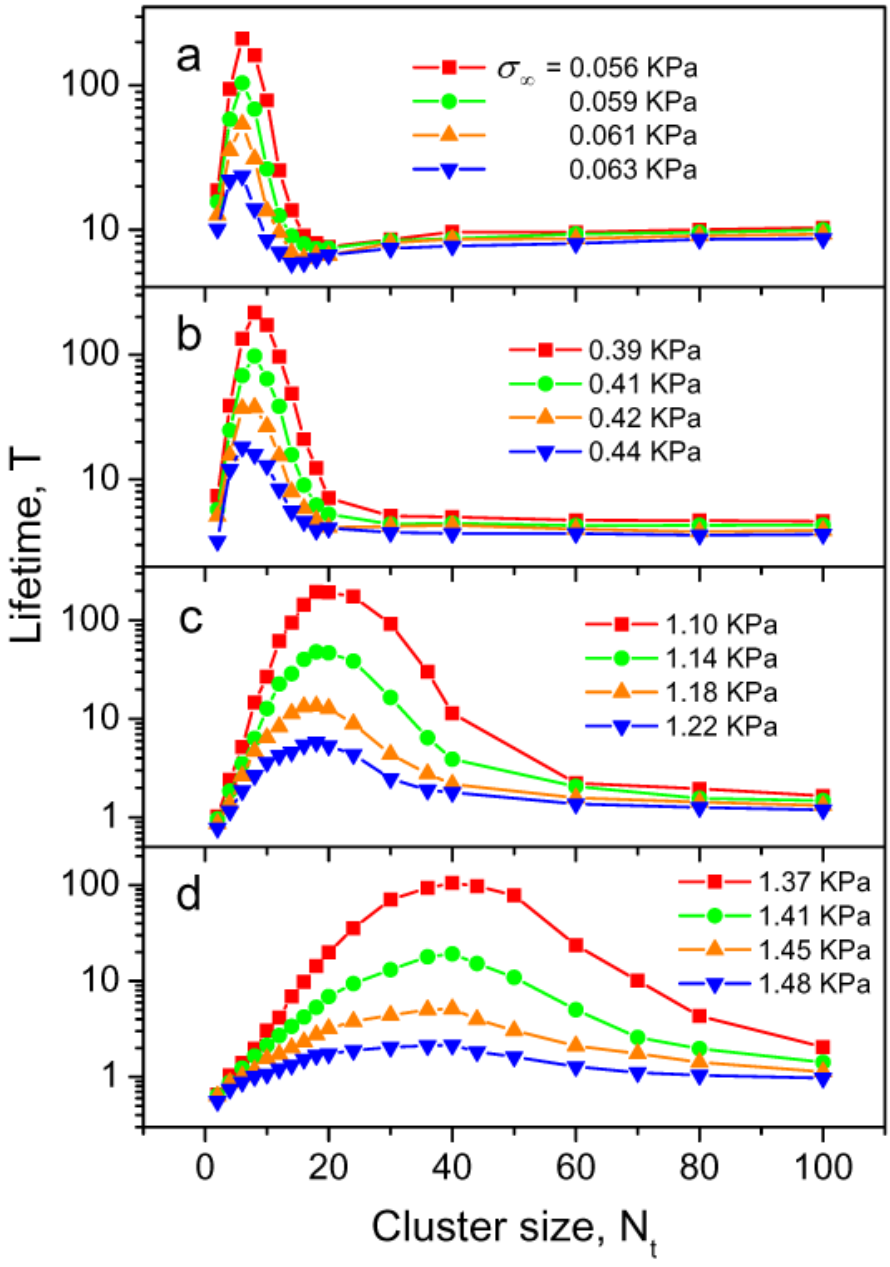

Figure 6.2: The lifetime T of periodic adhesion clusters as a function of the cluster size N_t for different values of the reduced modulus E^*. The pulling angle θ is fixed at 45°. The selected values of E^* are (a) 1 KPa; (b) 10 KPa; (c) 100 KPa; (d) 300 KPa.

6.3 Orientation-dependent strength and lifetime

Increasing the applied load eventually destabilizes the adhesion. For an example system with $N_t = 40$, $E^* = 10\,\mathrm{KPa}$ and $\theta = 45^\circ$, Figure 6.3a plots some representative simulation trajectories at three different stress levels. The average lifetime of two hundred simulated trajectories is plotted as a function of σ_∞ in Figure 6.3b. It is seen that the lifetime asymptotically approaches infinity as the applied stress is reduced to below a critical value. Stress levels larger than this critical value dramatically reduce the lifetime and destabilize the adhesion. This suggests that we can define the critical stress at which the cluster lifetime asymptotically approaches infinity as the adhesion strength. To investigate the dependence of adhesion strength on the pulling angle θ, we have further performed a series of Monte Carlo simulations by varying the value of θ. For a given magnitude of the applied stress, smaller pulling angles with respect to the cell-ECM interface lead to more stable adhesion. Figure 6.3c shows the adhesion strength as a function of θ for different reduced moduli E^* ranging from 1 KPa to 300 KPa. Here the cluster size N_t is fixed at 40 bonds. Stiffening cell and ECM decreases the stress concentration and therefore leads to dramatic increases in adhesion strength. Figure 6.3d shows the θ-dependence of the adhesion strength for different cluster sizes. Here E^* is fixed at 100 KPa. As the cluster size is increased from 6 to 20 bonds, the adhesion strength increases due to the collective effect of bond clustering. However, as the cluster size is further increased to 100 bonds, stress concentration effects dominate and cause the adhesion strength to decrease as a consequence of crack-like failure.

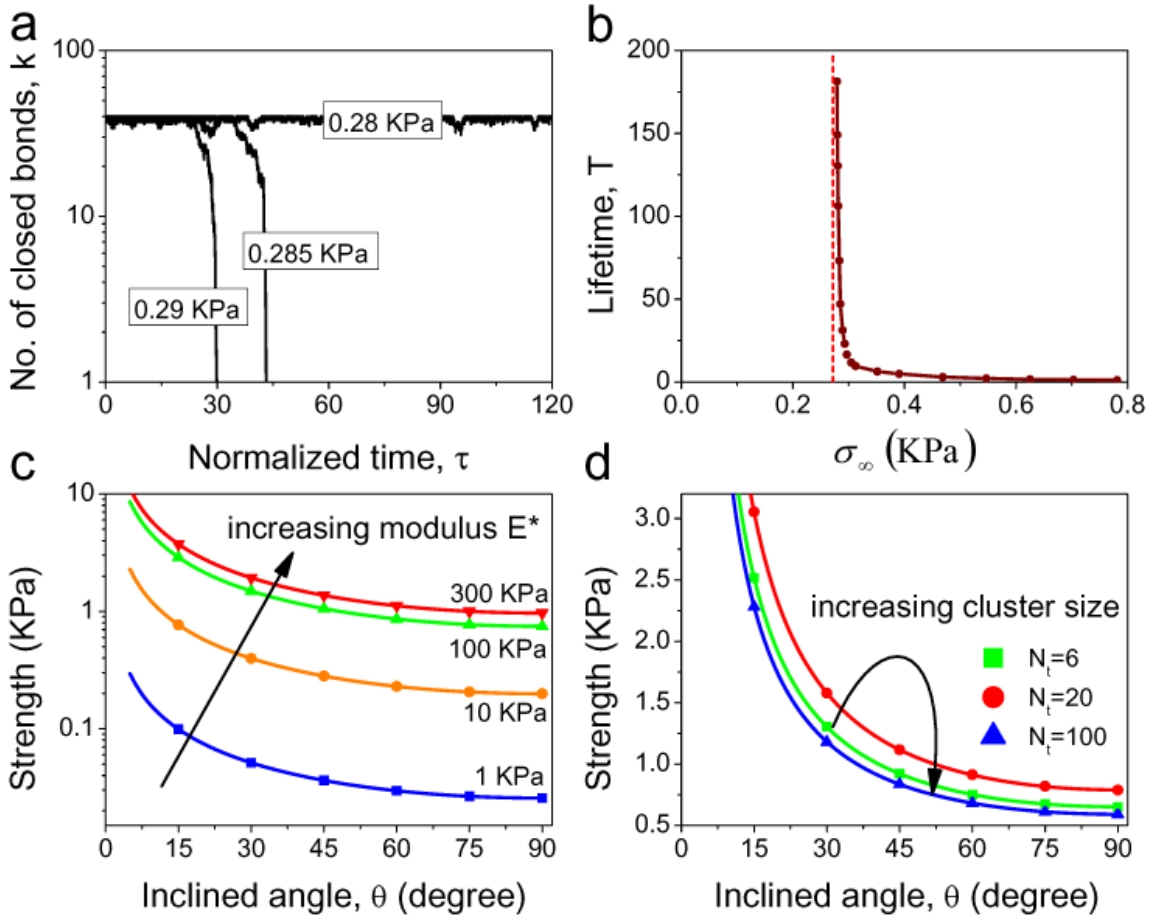

Figure 6.3: The strength of periodic adhesion clusters. (a) Representative simulation trajectories of the number of closed bonds k versus time τ at three selected stress levels ($N_t = 40$, $E^* = 10$ KPa and $\theta = 45^\circ$). (b) The adhesion lifetime T as a function of the applied stress σ_∞ . The lifetime asymptotically approaches infinity as the stress is reduced below a critical value which is defined as the adhesion strength ($N_t = 40$, $E^* = 10$ KPa and $\theta = 45^\circ$). (c) The adhesion strength as a function of the pulling angle θ for different values of the reduced modulus from 1 to 300 KPa ($N_t = 40$). (d) The adhesion strength as a function of the pulling angle θ for different values of the cluster size from 6 to 100 bonds ($E^* = 100$ KPa).

The lifetime T of the periodic cluster array is plotted as a function of the pulling angle θ at various stress levels in Figure 6.4. Here we fix $N_t = 40$ and $E^* = 10$ KPa in the calculations. We see that, for a given magnitude of the applied stress σ_∞ , decreasing θ

tends to stabilize the adhesion. In fact, the adhesion lifetime asymptotically approaches infinity as the pulling angle is reduced to below a critical threshold. This is especially interesting in view of the fact that cells generally flatten when they successfully adhere to a substrate and immediately suggests a regulation mechanism by which cells can switch between long- and short-lived adhesions by adjusting pulling directions around the critical angle.

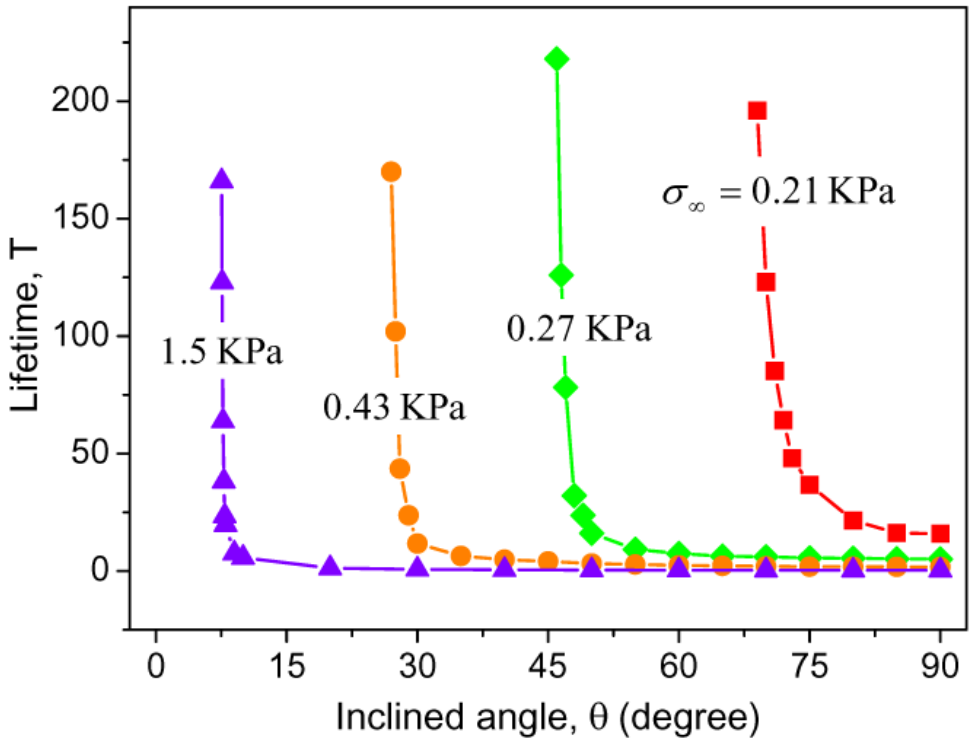

Figure 6.4: The lifetime T of periodic adhesion clusters as a function of the pulling angle θ at various levels of applied stress ($N_t = 40$ and $E^* = 10$ KPa).

6.4 Biological relevance

From the basic scaling parameter $\overline{\alpha}$ which governs the interfacial traction distribution and detailed Monte Carlo simulations, we observe that the adhesion size, substrate

rigidity, cytoskeleton stiffening and the direction of pulling forces all play important or critical roles in the stability of FAs. In particular, we have shown an elasticity-controlled transition between uniform and crack-like traction distributions along the cell-ECM interface. Although we do not expect that the present model can fully capture the complexity of real focal adhesions, it seems that the predictions from this model can provide possible explanations for a wide range of experimental observations and also suggest possible cytoskeletal mechanisms by which cells can control and regulate the growth and stability of FAs via contractility.

Our model suggests that the reason for FAs to lie in a narrow size range from a few hundred nanometers to a few microns might be that the growth of FAs eventually leads to crack-like delamination failure near the adhesion edges. From this point of view, the growth of FAs is self-limiting. Our analyses show that the optimal size window for stable adhesion is in the sub-micron to micron range, depending on the cell/substrate rigidity. This is also in qualitative agreement with experimental observations that stable and large FAs are only formed on sufficiently rigid substrates [25,26]. The fact that FAs on stiff substrates are more stable provides a potential driving force for cells to migrate toward stiffer part of the substrate. The effect of the reduced elastic modulus E^* on molecular adhesion implies that very soft substrates tend to diminsh the adaptive capability of cells in that crack-like interfacial traction would persist irrespective of the cytoskeleton stiffness, which may prevent short-lived FXs from maturing into stable FAs. On hard substrates, the reduced elastic modulus tends to be dominated by the stiffness of cytoskeleton. The cytoskeletal contractile forces can stiffen cytoskeleton by decreasing entropic elasticity of the actin network and therefore alleviate stress concentration at FAs

to achieve long-term stability. This is consistent with the experimental observations that cytoskeletal contractile forces are necessary to stabilize cell adhesion [30]. We also demonstrate the dependence of the adhesion lifetime and strength on the loading angle θ. Low-angle pulling dramatically increases the adhesion strength and lifetime. Therefore, spreading and flattening of a cell over a substrate result in low-angle pulling on FAs and therefore benefit stable adhesion. All these results are consistent with experimental observations and suggest multiple mechanisms by which cells can actively control adhesion and deadhesion by modulating the cytoskeletal contractility or adjusting the angle of stress fibers.

Generally speaking, rigid substrate, cytoskeleton stiffening, intermediate adhesion size and low-angle pulling are factors that contribute to stable cell adhesion whereas soft substrate, cytoskeleton softening by dissolution of actin network, extreme adhesion size and high-angle pulling are factors that tend to destabilize cell adhesion. Our model provides a unique guiding parameter $\overline{\alpha}$ to understand these phenomena.

6.5 Tension-induced growth of focal adhesions

Several key experiments have suggested that both mechanical forces and cell/ECM elasticity play an essential role in FA growth and maintenance. Some striking phenomena include: i) mature FAs are micron-size limited [22,23]; ii) FAs favor stiff substrates [25,26]; iii) tension is crucial for FA growth [32,33]. A number of theoretical studies have been performed to investigate how mechanical stimuli and cell/ECM properties affect the behaviors of cell adhesion. Deshpande et al. [57] have proposed a model of cellular contractility that accounts for dynamic reorganization of cytoskeleton. Bruinsma

[58] has described the regulation of cytoskeletal forces generated along actin filaments during the growth stage from initial contacts to focal complexes. Smith et al. [59] have showed force-induced adhesion strengthening by considering the thermodynamic interplay between elastic response of membrane, entropy of free receptors and enthalpy of bond formation.

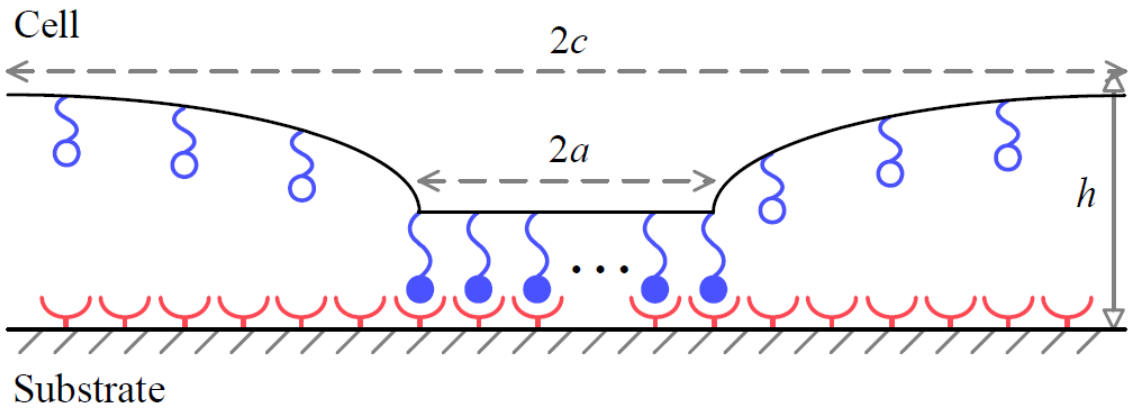

Figure 6.5: Schematic illustration of focal adhesion growth between two elastic bodies via clustering of receptor-ligand bonds.

In spite of these fascinating studies, the general physical mechanisms of FA dynamics and mechanosensitivity are still a subject of intense speculation and debate. Upon the stochastic-elasticity model which includes applied tension, cell/ECM elasticity, receptor-ligand binding/unbinding, we incorporate receptor diffusion in the same framework to investigate the assembly and growth of focal adhesions under tension [60]. Our results demonstrate tension-induced clustering of receptor molecules and growth of FAs consistent with experimental observations.

We study the behavior of an elastic cell-substrate system with an interfacial layer of molecular bonds under tension. As shown in Figure 6.5, the idealized model under

investigation involves one unit of a periodic array of adhesive molecular bond clusters between two dissimilar elastic media, where the adhesion is provided through specific interactions between receptors and ligands on opposite surfaces. One side of the adhesion is an elastic medium mimicking a cell body and the other side represents an elastic substrate (ECM or another cell). The initial cell-substrate separation is h.

Due to the periodic nature of the adhesion clusters, we focus our attention on one repeated domain with size $2c$ and adopt a discretized Cartesian lattice x_i along the interface with nodal spacing b chosen to be a receptor size (~10 nm) so that only one molecule can occupy a lattice site. The substrate is assumed to be fully coated with ligands. The system starts with an initial FA (size: $2a$) consisting of a dense cluster of closed receptor-ligand bonds at the center of the domain. Outside the cluster, we assume that there are sparsely distributed free receptors which can diffuse on the cell surface. The system is periodic and the domain is subjected to the zero flux (reflecting) condition at its boundaries. The closed bonds are modeled as Hookean springs with zero rest length and stiffness k_{LR} until rupture.

The approach described in Chapter 3 is used to determine the force on each closed bond as well as the interfacial separation at each open bond. For a bond location x_i within the adhesion domain, the displacement discontinuity induced by a bond at location x_j is given by the elastic Green's function as

$$\Delta u_z\left(x_i, x_j\right) = u_z^C - u_z^S = G_{ij} F_j, \tag{6.1}$$

where F_j is the force on bond at x_j and G_{ij} is given in Equation (3.32) for periodic case.

The geometrical relation of compatibility is

$$\sum_{j=1}^{k} G_{ij} F_j + h = \frac{F_i}{k_{LR}}, \tag{6.2}$$

which is used to solve for bond forces F_i of k closed bonds at given h. The interfacial separation between cell and substrate at x_i can be calculated as

$$\delta_i = \sum_{j=1}^{k} G_{ij} F_j + h. \tag{6.3}$$

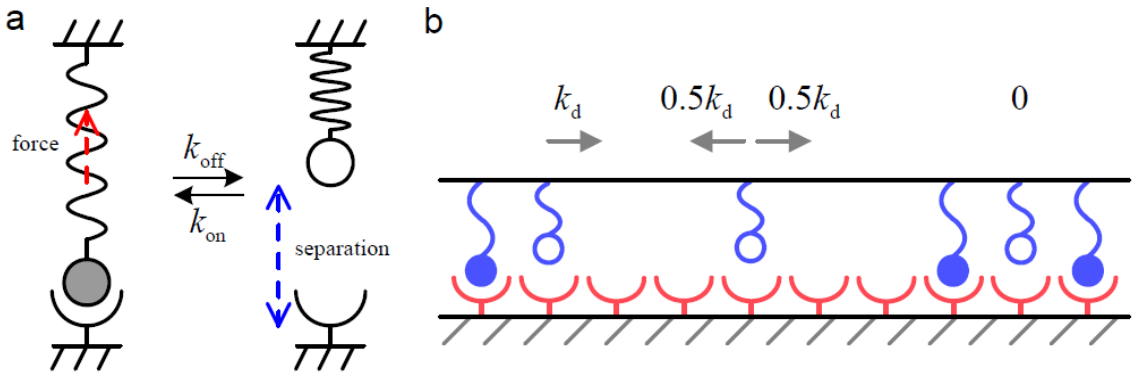

Figure 6.6: Stochastic reactions at the interface between cell and substrate. (a) Bond dissociation and association transiting between closed and open states. (b) Diffusion of open receptors.

A closed bond will rupture at rate $k_{off}(F_i)$ and an open one will rebind at rate $k_{on}(\delta_i)$ (Figure 6.6a), as described in Equations (2.2) and (2.8). On the other hand, if an open receptor is selected to undergo a diffusion event, the molecule will hop by a nodal spacing b in one of the possible directions with equal probability. Because receptor molecules are not allowed to occupy the same node due to volume exclusion effect, the diffusion hop will only be possible for those receptors that are not connected to ligands and have at least one neighboring node unoccupied, as illustrated in Figure 6.6b. The diffusion rate, k_d, and the intra-membrane diffusivity of receptors, D_0, through a random walk model are related by

$$k_{\mathrm{d}} = 2D_0 / b^2 , \tag{6.4}$$

which is assumed to be the same for all free receptors.

The relevant physical/biological parameters used in the simulations are listed in Table 6.1 unless stated otherwise. To understand how the adhesion domain will evolve under different values of h, let us first focus on the initial state. A focal adhesion consisting of 21 closed bonds are densely packed at the domain center and 20 free receptors are sparsely and uniformly distributed over the area outside the FA. Figure 6.7a shows the distributions of normalized bond force within the adhesion domain when h is 10 and 16 nm. Outside the FA, none of the receptors are subjected to any force because they are not bonded to ligands at this initial stage. Within the FA, the bond forces are highly non-uniform, as suggested by the stress concentration index in reference [41]. We also observe that the bond forces are small compared to the force scale F_b, and the resulting dissociation rate (normalized by k_0) will be ~1 as described in Equation (2.2). Figure 6.7b plots the distributions of normalized interfacial separation within the domain. Given the separation-dependent association rate in Equation (2.8), one expects that the dominant association will occur at those vacant ligand sites near FA edges. Figure 6.7c lists all the dissociation/association rates within the adhesion domain. We see that the association rates near FA edges win over dissociation rates so the number of closed bonds will grow. The competition between bond association near FA edges and receptor diffusion determines the pattern of receptor clustering and FA growth.

Table 6.1: Parameter list for the simulations of focal adhesion growth

Parameters	Values
Spacing between neighboring lattice nodes, b	10 nm
Size of adhesion domain, $2c/b$	220
Size of initial FA, $2a/b$	20
Initial number of closed bonds	21
Initial number of open receptors	20
Interfacial separation before deformation, h	10 nm, 16 nm
Reduced elastic modulus, E^*	10 KPa
Stiffness of single closed bond, k_{LR}	1 pN/nm
Force scale in bond dissociation, F_b	4 pN
Factor of bond association rate, k^0_{on}/k_0	3200
Binding radius of bond association, l_{bind}	1 nm
Diffusion rate, k_d/k_0	1000

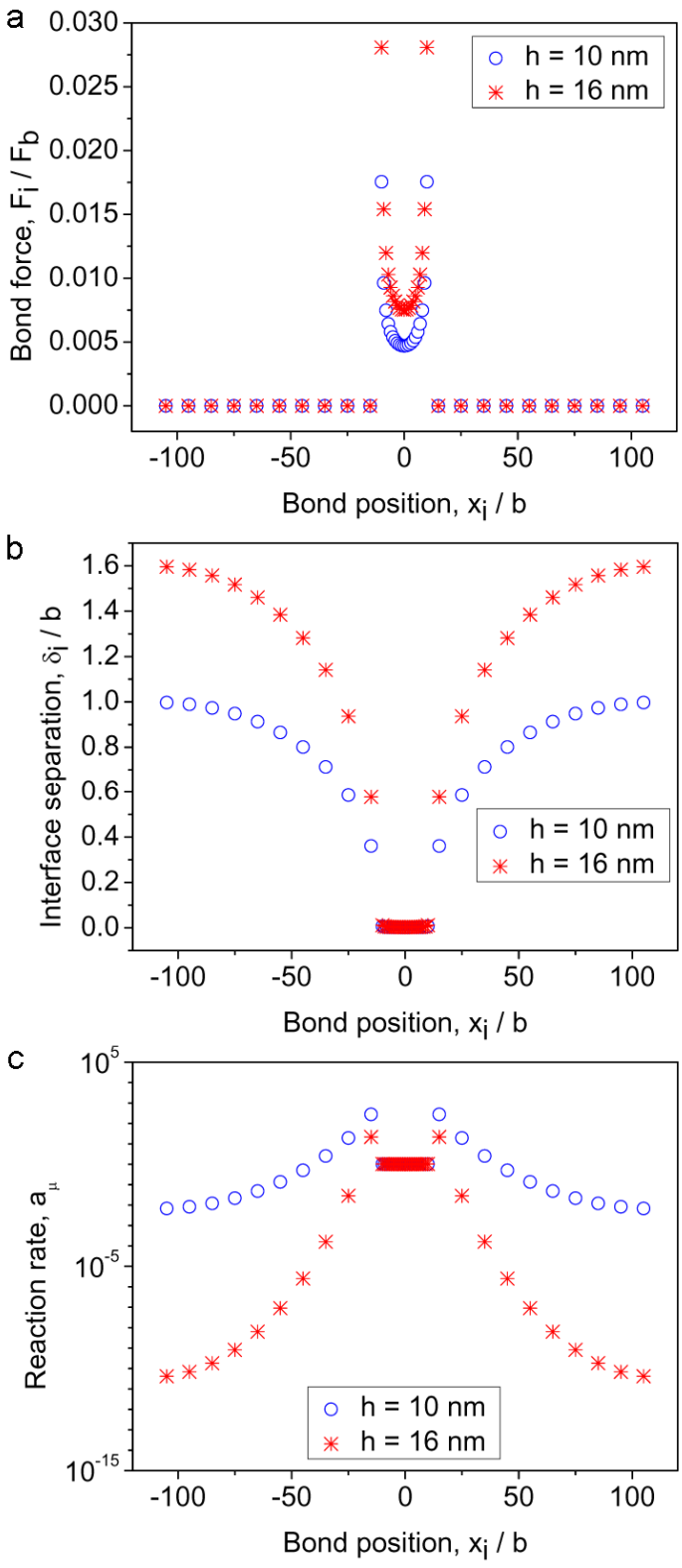

Figure 6.7: The distributions of (a) bond force, (b) interfacial separation and (c) reaction rate within the adhesion domain at initial state.

We may define an “association zone” near FA edges as the area where bond association wins over receptor diffusion. Roughly speaking, free receptors entering “association zone” tend to form closed bonds with the ligands on opposing substrate. The size of the “association zone” decreases as h increases. When h is small, the “association zone” is large, therefore molecular receptors will pack near FA edges and form closed bonds in a dispersed manner. There always exists a critical value of h at which the “association zone” is limited to 1 or 2 lattices in our model and receptors will tightly pack at FA edges site by site. The simulation snapshots in Figures 6.8a and 6.8b confirm this behavior. The clustered states during the stochastic evolution process are collected when h is 10 and 16 nm, respectively. Averaging the final cluster configuration over 200 independent trajectories gives the probabilities of observing a closed bond at the locations within the adhesion domain, as shown in Figures 6.8c and 6.8d. It is clear that the FA grows as h is increased from 10 nm to 16 nm.

These simulations are in qualitative agreement with the striking observations by Riveline and coworkers [32] that more force increases the size and density of focal adhesions. In their work, mechanical force was applied to dot-like adhesions at the cell edge using a micropipette. Mapping of fluorescence-tagged receptor molecules revealed that pulling led to local assembly of adhesion molecules and their development into larger focal contacts. Experiments by Balaban et al. [33] have also shown that the size of mature FAs is proportional to the local force, with force per unit area maintained near a constant value around 5.5 KPa irrespective of the cell type. It is encouraging that the prediction of our idealized model has the main feature consistent with these experiments.

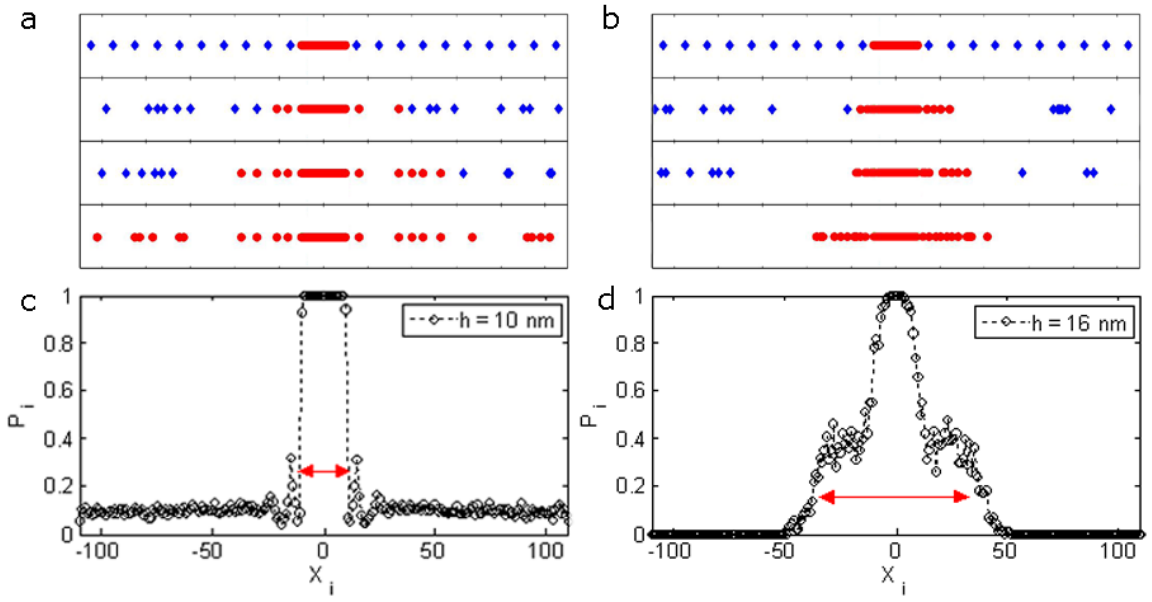

Figure 6.8: The snapshots of cluster state during stochastic evolution process for (a) $h = 10\,\mathrm{nm}$ and (b) $h = 16\,\mathrm{nm}$. The probabilities of observing a closed bond within the adhesion domain when (c) $h = 10\,\mathrm{nm}$ and (d) $h = 16\,\mathrm{nm}$.

In comparison with our previous work [41], the present model has incorporated intra-membrane diffusion of free receptors. We have demonstrated tension-induced clustering of receptor molecules and growth of focal adhesions through the stochastic interplay between receptor-ligand dissociation, association and open receptor diffusion in a Monte Carlo scheme.

Accurate in vitro measurements of bond stiffness, receptor diffusivity, interface deformation, etc. would be important in establishing the validity of a more systematic simulations. We believe that further computational simulation and experimental investigation can significantly improve our understanding of the complex processes involved in the growth of focal adhesions under forces.

Chapter 7

Wet adhesion

7.1 Overview of wet adhesion in biology

In contrast to most chapters in this thesis which are focused on exploring the coupling between stochastic rupture/rebinding processes and elasticity effects in cell-matrix adhesion, this chapter is dedicated to wet adhesion at the organism scale. The study of biological adhesion mechanisms in insects and lizards has a long history since it not only provides insights into biological systems but may also yield general principles employed in nature as inspiration and guidance for the development of biomimetic adhesive devices. Different hypotheses of bio-adhesion mechanisms, such as hooks, micro-suckers and electrostatic forces, have been proposed [61]. However, investigators have since rejected some of the mechanisms based on experiments or observations of a broad diversity of species.

At the organism scale, it has been concluded that van der Waals interactions (dry adhesion) and capillary interactions (wet adhesion) are the two main mechanisms attributable to biological attachments [62]. Dry adhesion is adopted by geckos, jumping spiders, etc. [63,64]. These animals have achieved superior attachment ability through

elaborate adhesive structures on their feet. Experimental investigations have revealed that the bio-adhesive structures are often finely-split and hierarchical. Theoretical studies based on contact mechanics have pointed out that splitting of a contact patch into fine sub-divided elements can result in enhancement of adhesion strength [65]. Furthermore, it has been suggested that the concept of flaw tolerance may be a general principle in biological systems [66–70]. It has been found that, in the presence of pre-existing flaws, the adhesion strength can be optimized by size reduction to nanoscale [66–68], gradient material design [69] and hierarchical energy dissipation [70].

Animals like beetles, blowflies and ants have not evolved the same attachment terminals as geckos [71–79]. They resort to another strategy which is based more on wet adhesion. When they attach to surfaces, some secretory fluid is produced and delivered to the bottom of the attachment pads. The fluid footprints left behind by the animals are simply the replica pattern of their adhesive pads [71]. Recent experiments with flies have confirmed the special mechanisms for the release of secretion to individual pads [78]. The evidence that the secretion is crucial for successful attachment is provided by observations that animals appear to lose their ability to adhere on surfaces after treatments to remove the secretion from their feet [79].

The present study aims to understand the underlying principles of fibrillar wet adhesion. The behavior of a liquid bridge connecting a fiber and a substrate is analyzed as a model problem. The fiber is quasi-statically pulled away from the substrate against the capillary force of the liquid bridge. We investigate how the liquid volume and contact angles alter the stress–separation behavior of the liquid bridge. The influences of the system's characteristic length scale on the adhesion strength and adhesion energy are of

special interest.

7.2 Model and analysis

The system to be investigated is described in Figure 7.1a. A solid fiber with a circular cross section and radius R is assumed to be in wet adhesion with a solid substrate through a liquid bridge. The contact angle of the liquid with the fiber surface is θ_1 and that with the substrate is θ_2. We make the following assumptions in the study: (i) the effect of gravity is assumed to be negligible at the size scale of individual fibers in a biological attachment system; (ii) the volume of the liquid is conserved; (iii) both fiber and substrate are rigid solids, and the fiber has a flat-ended tip [80].

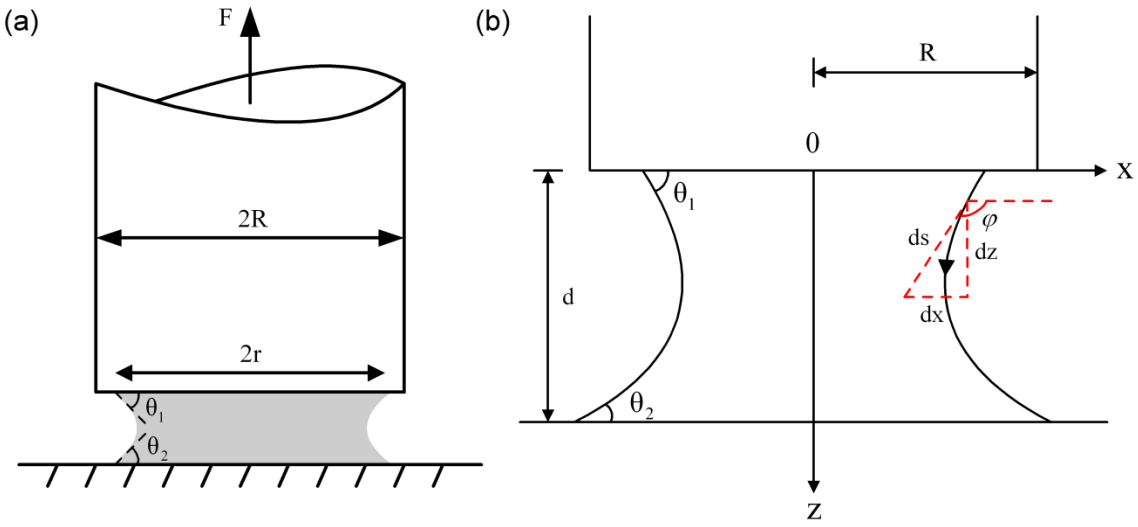

Figure 7.1: (a) The geometry of a flat-ended fiber adhering to a rigid substrate via a liquid bridge. (b) The coordinate system used in solving the Young–Laplace equation for the axisymmetric liquid profile between the fiber and substrate. The arrow on the liquid profile indicates the direction of increasing arc length.

There have been a number of similar theoretical studies on capillary adhesion due to

liquid bridges in the past. Orr et al. [81] considered a liquid bridge between a sphere and a plate and obtained analytical expressions for the bridge profile in terms of elliptic integrals. The results have been recently applied in a scheme to manipulate small objects via capillary interactions [82]. In our model, the substrate is infinite and the fiber tip has a finite size; the liquid volume is conserved such that the liquid bridge may shrink or expand as the fiber is pulled or pressed. A critical solid separation, below which the liquid periphery becomes pinned at the edge of the fiber, defines a transition point between contact angle dominated adhesion and fiber radius dominated adhesion. A similar transition has been considered previously for liquid bridges between two identical plates [83].

The total adhesive force acting on the fiber, F, has two components. One is induced by the pressure difference across the liquid–gas interface. The other arises from the axial component of liquid surface tension acting along the liquid periphery on the tip of the fiber. The sum of these forces can be written as [81]

$$F = -\pi r^2 \cdot \Delta P + 2\pi r \cdot \gamma \sin\theta_1, \tag{7.1}$$

where r is the radius of the wet area on the fiber tip, γ is the liquid surface tension (for this chapter only), and ΔP is the pressure difference inside and outside the meniscus, which is related to the local liquid profile by the Young–Laplace equation [84]

$$\Delta P = \gamma\left(\frac{1}{R_1} + \frac{1}{R_2}\right), \tag{7.2}$$

where R_1 and R_2 are the two local principal curvatures of the liquid profile. Since the effect of gravity is neglected in our study, ΔP is a constant within the meniscus and the liquid profile has the same mean curvature at any point.

Calculation of the adhesive force in Equation (7.1) requires the solution to liquid profile for given liquid volume, contact angles and fiber–substrate separation. A variable transformation changes the original Young–Laplace equation into the following system of ordinary differential equations with the arc length as the independent variable:

$$\frac{dx}{ds} = \cos\varphi\,,\ \frac{dz}{ds} = \sin\varphi\,,\ \frac{d\varphi}{ds} = \frac{\Delta P}{\gamma} - \frac{\sin\varphi}{x}\,, \tag{7.3}$$

where x and z are the coordinates of the axisymmetric liquid bridge, φ is the angle between the local tangent of liquid surface and the horizontal axis, and s is the arc length of the liquid profile, as indicated in Figure 7.1b.

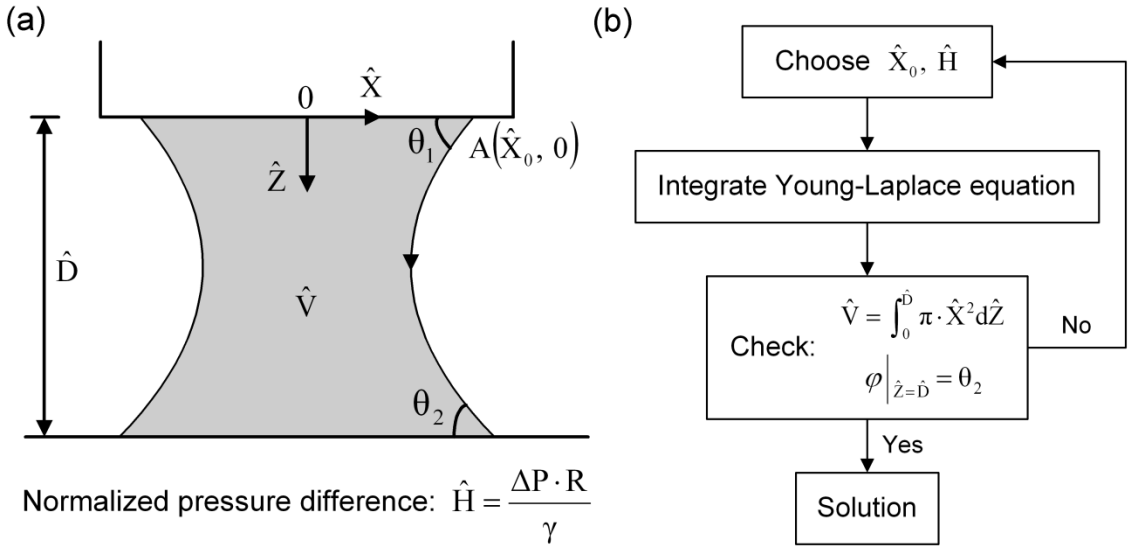

Figure 7.2: The numerical scheme to solve the Young-Laplace equation. (a) Initial guesses of $\hat{X}_0$, $\hat{H}$ and prescribed conditions of liquid volume and contact angles. (b) The iteration program to determine the solution.

With the following normalization by fiber radius R: $\hat{X} = x/R$, $\hat{Z} = z/R$, $\hat{S} = s/R$, the equation system can be rewritten as

$$\mathrm{d}\hat{X}/\mathrm{d}\hat{S} = \cos\varphi,\ \mathrm{d}\hat{Z}/\mathrm{d}\hat{S} = \sin\varphi,\ \mathrm{d}\varphi/\mathrm{d}\hat{S} = \hat{H} - \sin\varphi/\hat{X}\ , \tag{7.4}$$

where $\hat{H} = (\Delta P \cdot R)/\gamma$ is a dimensionless parameter measuring the pressure difference. For given values of non-dimensional liquid volume $\hat{V}$ (actual liquid volume normalized by R^3), contact angles θ_1 and θ_2, and non-dimensional fiber-substrate separation $\hat{D}$ (actual separation normalized by R), a unique liquid surface profile can be obtained by simultaneous integration of above equation system.

We treat Equation (7.4) as a typical initial value problem: *A* is assumed to be the point where the liquid profile meets the fiber tip, as indicated in Figure 7.2a. The initial values of point *A* are: $\hat{X}(0) = \hat{X}_0$, $\hat{Z}(0) = 0$, $\varphi(0) = \pi - \theta_1$. Initial guesses of the values of $\hat{X}_0$ and $\hat{H}$ are made at the start of integration. A numerical iteration scheme, as illustrated in Figure 7.2b, is adopted to determine $\hat{X}_0$ and $\hat{H}$ by two conditions. First, the calculated liquid volume should match the prescribed value $\hat{V}$, i.e.

$$\hat{V} = \int_0^{\hat{D}} \pi \cdot \hat{X}^2 \mathrm{d}\hat{Z}\ . \tag{7.5}$$

Also, the liquid profile should meet the substrate at the prescribed contact angle θ_2, i.e.

$$\varphi\big|_{\hat{Z}=\hat{D}} = \theta_2\ . \tag{7.6}$$

As soon as the values of $\hat{X}_0$ and $\hat{H}$ are determined, the adhesive force can be calculated as a function of the prescribed liquid volume $\hat{V}$, contact angles θ_1 and θ_2, and fiber-substrate separation $\hat{D}$ via the following expression:

$$F = \pi \gamma R\left(-\hat{H}\hat{X}_0^2 + 2\hat{X}_0 \sin\theta_1\right). \tag{7.7}$$

The corresponding adhesive stress is

$$\sigma = \frac{F}{\pi R^2} = \hat{\eta} \cdot \frac{\gamma}{R}, \tag{7.8}$$

where $\hat{\eta} = \left(-\hat{H}\hat{X}_0^2 + 2\hat{X}_0 \sin\theta_1\right)$ is a dimensionless coefficient. Obviously, $\hat{\eta}$ is also a function of liquid volume, contact angles and fiber-substrate separation. We define $\hat{\eta}^*$ to be the maximum value of $\hat{\eta}$ for all possible separations, which is a function of liquid volume and contact angles. The adhesion strength σ^*, corresponding to the maximum value of σ, can be expressed as

$$\sigma^* = \hat{\eta}^*\left(\hat{V}, \theta_1, \theta_2\right) \cdot \frac{\gamma}{R}, \tag{7.9}$$

which is proportional to liquid surface tension γ and depends on the non-dimensional liquid volume $\hat{V}$ and contact angles θ_1, θ_2. Interestingly, the wet adhesion strength is inversely proportional to the fiber radius R. Therefore, size reduction enhances not only dry [65,67], but also wet adhesion. We will discuss in the next section how the parameters $\hat{V}$, θ_1 and θ_2 influence and how size reduction optimizes the adhesion strength.

7.3 Stretching behavior of a liquid bridge

Consider a quasi-static separation of the liquid bridged fiber from the substrate. For typical parameter values, we take $\hat{V}$ to be 0.5, θ_1 and θ_2 to be zero, according to the

experimental data for beetles [71]. The curve in Figure 7.3 shows the non-dimensional adhesive stress acting on the fiber as a function of the non-dimensional fiber-substrate separation from equilibrium point until the liquid bridge breaks up. The equilibrium point is defined as the separation at which the total adhesive stress is zero. This equilibrium state exists because the finite size of the fiber restricts spreading and thinning of the liquid bridge.

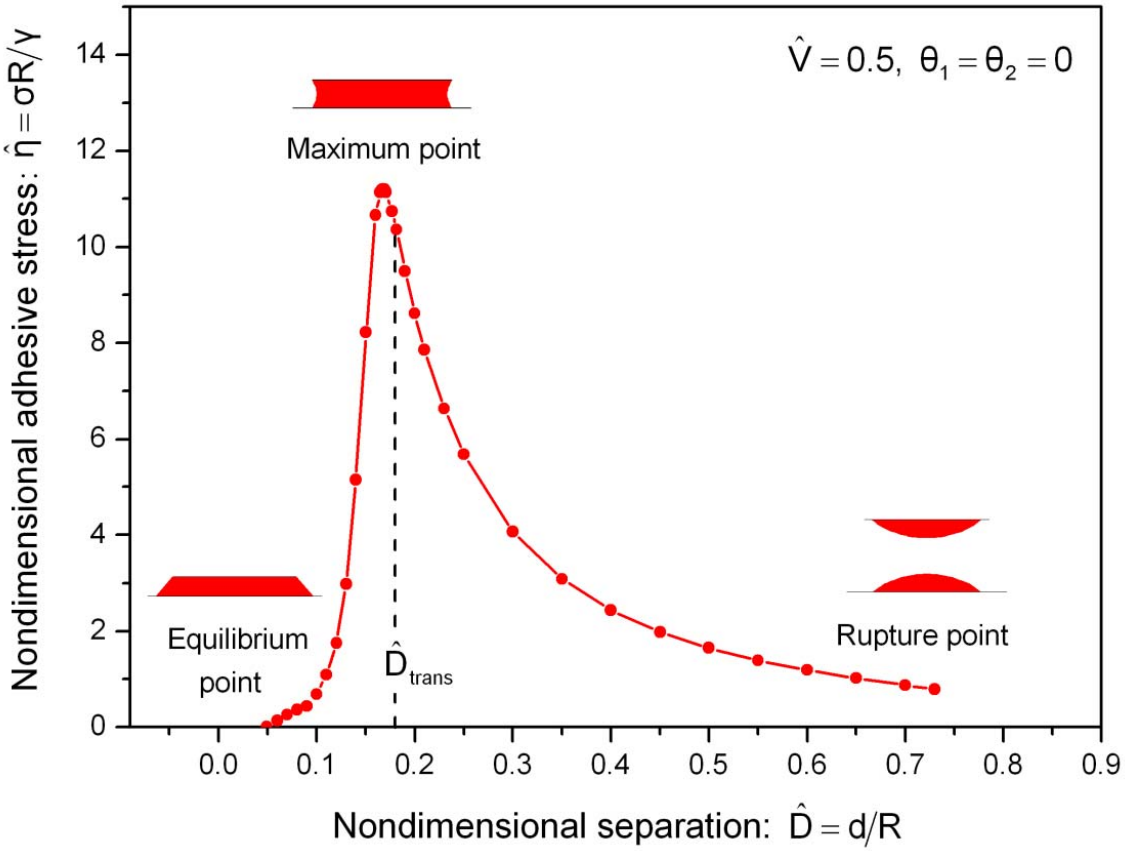

Figure 7.3: The quasi-static stress–separation curve of a liquid bridge with normalized liquid volume 0.5 and zero contact angles.

Figure 7.4 shows some snapshots of the equilibrium profiles of the liquid bridge for different fiber-substrate separations. When the separation is large, the liquid periphery

doesn't touch the circumference of the fiber, and the liquid meets both solid surfaces at the corresponding contact angles (Figure 7.4a). As the separation is reduced, the liquid spreads outward to conserve its volume. At a critical separation, the liquid reaches the edge of the fiber tip (Figure 7.4b). If the separation continues to decrease, the periphery of the liquid bridge becomes fixed at the edge of the fiber tip at angles different from the contact angle. Liquid periphery on the substrate is still free to spread at the contact angle (Figure 7.4c). The approaching is finally stopped at the equilibrium point when the total stress acting on the fiber becomes zero (Figure 7.4d). The separation at which the liquid starts to touch the circumferential edge of the fiber tip is a critical point (indicated as $\hat{D}_{\text{trans}}$ in Figure 7.3). The liquid configurations are said to be "angle-controlled" above this separation and "radius-controlled" below it. For "radius-controlled" configurations, the numerical iteration scheme in Section 7.2 is slightly modified as follows: $\hat{X}_0$ should now be fixed as unity; the angle at which the liquid meets the fiber and the parameter $\hat{H}$ should be looped to adjust the liquid profile to satisfy the conditions on liquid volume and contact angle on the substrate.

Above the equilibrium point, the stress acting on the fiber is always attractive. The "pulling" stress increases at the beginning until a maximum value and then decreases with continuous increase in the separation $\hat{D}$. The maximum adhesive stress, corresponding to the adhesion strength in Figure 7.3, occurs in the "radius-controlled" regime.

There exists a critical separation beyond which a stable liquid bridge no longer exists due to a breakage instability [85]. This critical separation is denoted as "rupture point" in Figure 7.3. Reading the maximum value of $\hat{\eta}$ in the stress-separation curve and referring

to Equation (7.9), we find that the adhesion strength for self-similar systems satisfying $\hat{V} = 0.5$ and $\theta_1 = \theta_2 = 0$ can be expressed as $\sigma^* = 11.2 \cdot \gamma / R$, where γ is the liquid surface tension and R is the fiber radius.

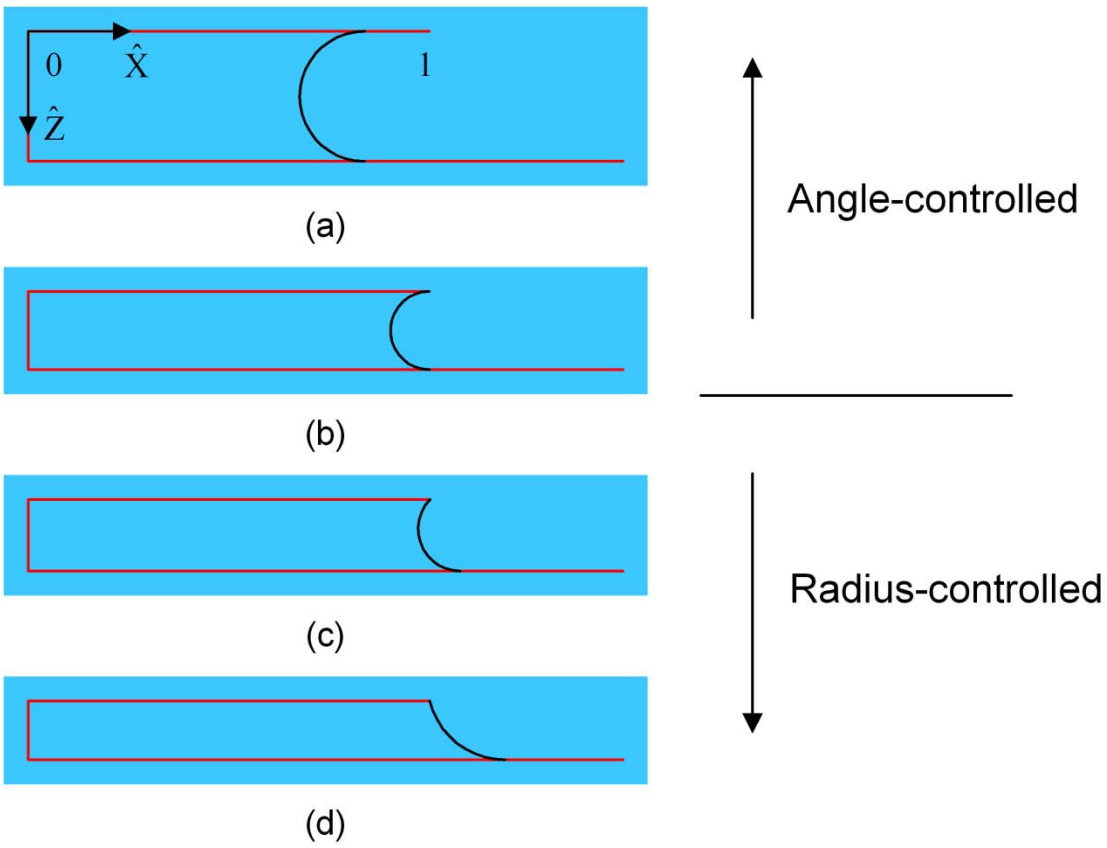

Figure 7.4: The snapshots of the liquid bridge profile at different separations between the fiber and substrate. The normalized liquid volume is 0.5 and both contact angles are taken to be zero.

7.4 Adhesion strength: influences of liquid volume and contact angles

Equation (7.9) shows that the dimensionless adhesion strength $\hat{\eta}^*$ depends on the values of liquid volume and contact angles. The influence of different contact angles are summarized in Figure 7.5. The dimensionless liquid volume is fixed at 0.5. Different

curves represent different values of θ_1 in the figure. We see that the dimensionless adhesion strength decreases when the substrate becomes more hydrophobic. Surprisingly, the curves for $\theta_1 = 0$ and $\theta_1 = 30^\circ$ overlap almost completely, indicating that slight changes of the fiber chemistry do not influence the adhesion strength when θ_1 is small. This is consistent with the observation that the maximum adhesive stress generally occurs in the "radius-controlled" regime so that the adhesion strength is dominated by the fiber radius, rather than the fiber contact angle.

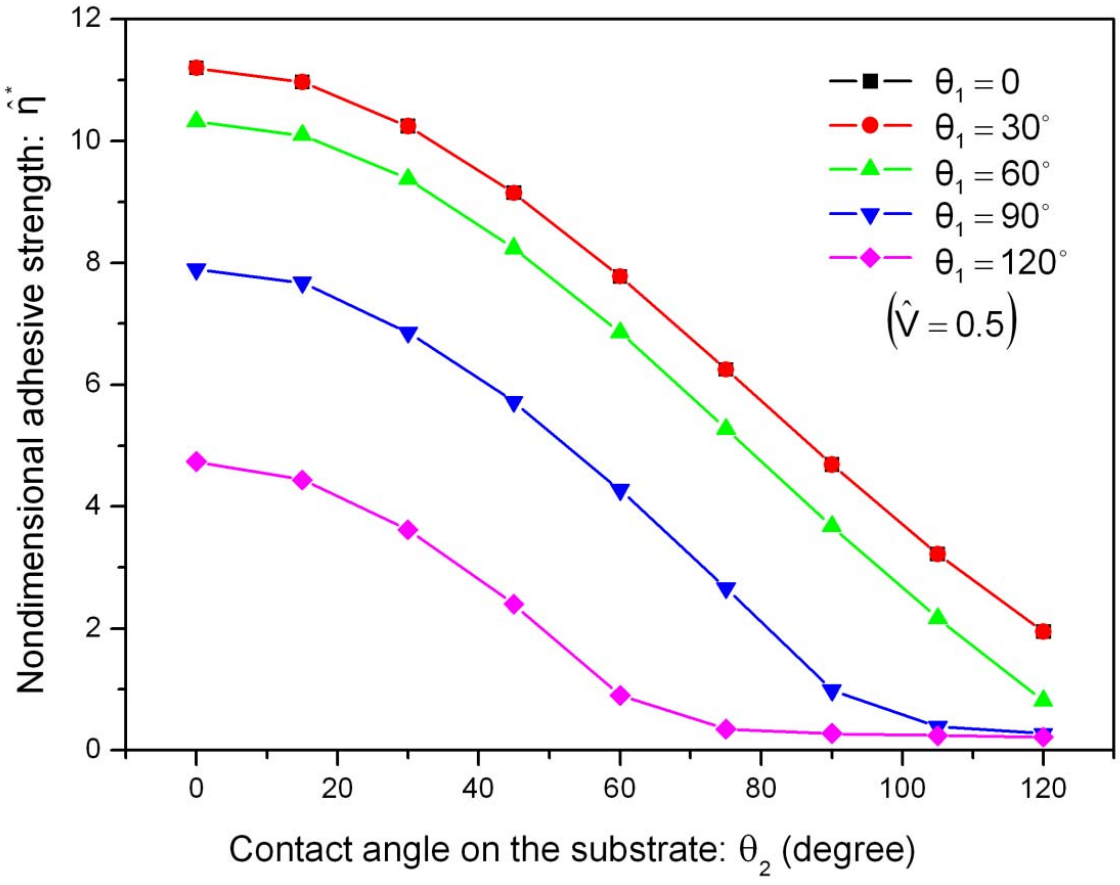

Figure 7.5: The normalized adhesion strength $\hat{\eta}^*$ as a function of the substrate contact angle θ_2 for different values of the fiber contact angle θ_1. The normalized liquid volume is taken to be 0.5.

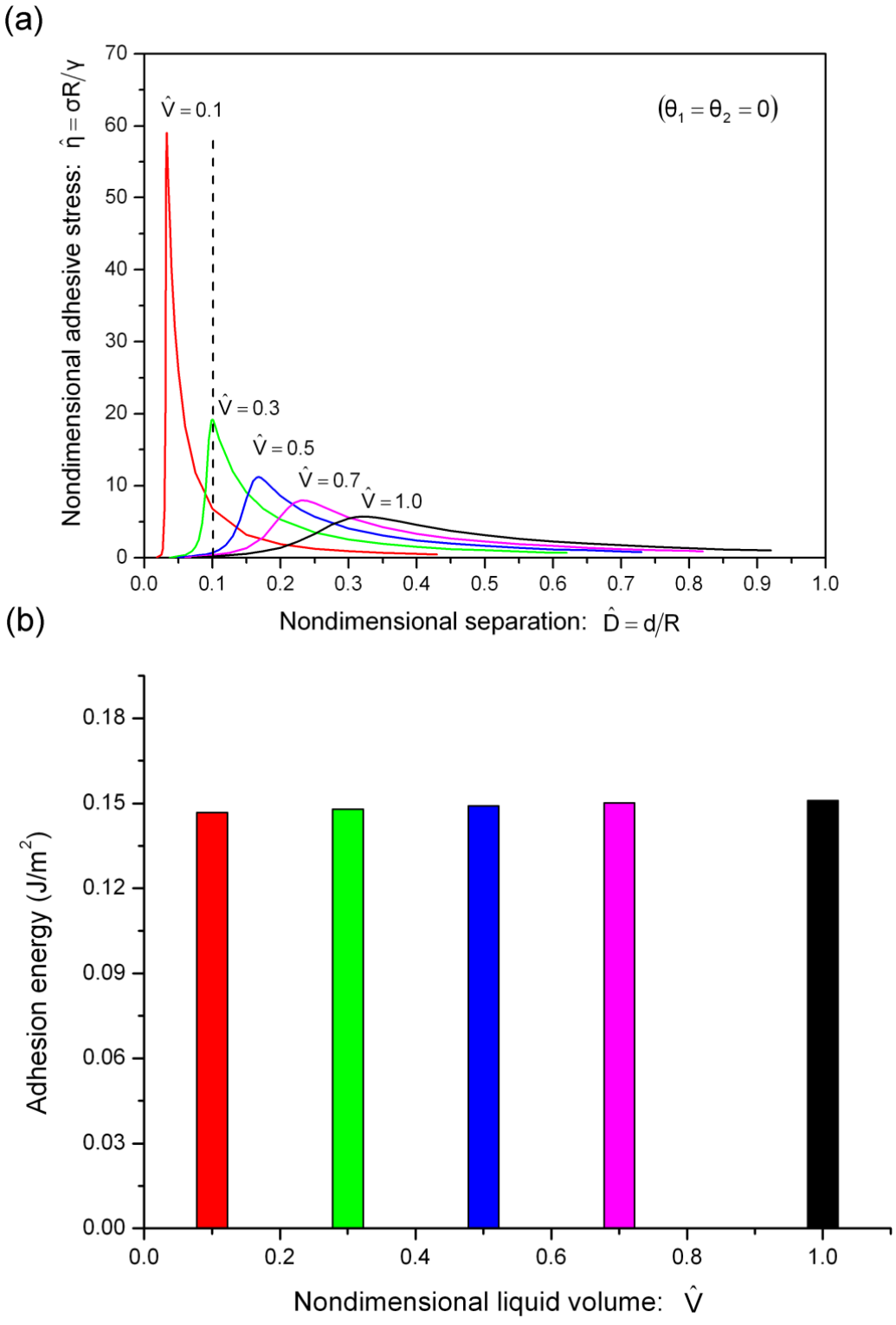

Figure 7.6: (a) The stress-separation curves for different values of the trapped liquid volume $\hat{V}$. Both contact angles are fixed at zero. (b) The values of adhesion energy integrated from the stress-separation curves for different values of $\hat{V}$.

Another observation is that, when θ_1 is relatively small, say 0-30 degrees, increasing substrate hydrophobicity does not bring catastrophic decrease of the adhesion strength. Even when $\theta_2 = 120^\circ$, in which case the liquid cannot spread well on the substrate, the adhesion strength is still about 20% of that when θ_2 is zero. This suggests that having a hydrophilic fiber tip with small θ_1 can help the system achieve successful adhesion to both hydrophilic and hydrophobic surfaces. This feature may be important from a robust point of view. Since insects cannot anticipate what kind of surfaces they are going to land, it would be safe for them to adopt a design which only requires the secretion to have small contact angles on their feet. This point is consistent with experimental results [78] where the researchers have only argued that the small contact angle ensures better secretion delivery. Besides this, our analysis shows that the small contact angles on animal foot pads also help to ensure successful adhesion on substrates with unknown properties.

Figure 7.6a shows the influence of different liquid volumes on the adhesion strength. The contact angles are fixed at zero. The results indicate that smaller liquid volume results in greater adhesion strength. Does this mean that insects should produce secretion as little as possible to their feet? That could be true only if both solids are perfectly smooth. However, actual solids always have roughness on their surfaces [86,87]. As the two rough solid surfaces approach each other, some of the asperities may get into contact and stop further approaching process. At this moment, there may still be a gap between the average planes of the surfaces, as shown in Figure 7.7. We define a minimum possible separation for the solids, $\hat{D}_{\min} = \delta / R$, where δ characterizes the surface fluctuation and R is the lateral size of the fiber. Assuming that the surface asperities

fluctuate at 10% of the lateral dimension of the fiber, we take $\hat{D}_{\min} = 0.1$, indicated by the dashed line in Figure 7.6a. Separations below this line are impossible because of the roughness on solid surfaces. We see that the stress-separation curve for $\hat{V} = 0.1$ cannot achieve its maximum value of adhesive stress, and $\hat{V} = 0.3$ is the appropriate liquid volume to maximize the adhesion strength. Recalling Equation (7.9), the expression of adhesion strength is calculated to be $\sigma^* = 19.1 \cdot \gamma / R$ for this case. An important conclusion is that, by considering a minimum possible separation for the solid surfaces, we can always find a lower bound of liquid volume to maximize the adhesion strength of the system.

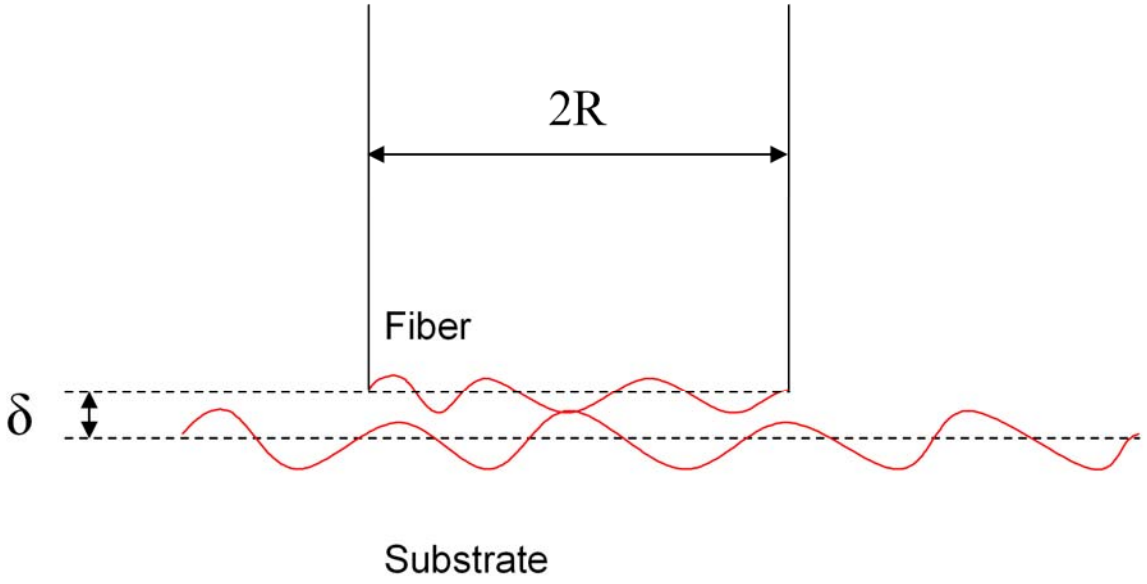

Figure 7.7: Schematic illustration of the minimum separation associated with the roughness fluctuation on solid surfaces.

7.5 Adhesion energy

The inverse scaling law of wet adhesion strength indicates that fibrillar structures with finely sized contact tips can result in strength enhancement in comparison with uniform

attachment pads. That is probably at least one of the reasons why animals have evolved setae array as their attachment devices. However, if an array of setae adhering to a substrate is considered, the breaking of adhesion may not be a simultaneous rupture of all fibers at once, but often a propagation of a crack-like flaw as illustrated in Figure 7.8. Therefore, it is also of interest to calculate the adhesion energy associated with wet adhesion. For our model, this adhesion energy is simply the integration of the adhesive stress along the entire range of fiber-substrate separation as

$$G = \int \sigma \, \mathrm{d}d \, . \tag{7.10}$$

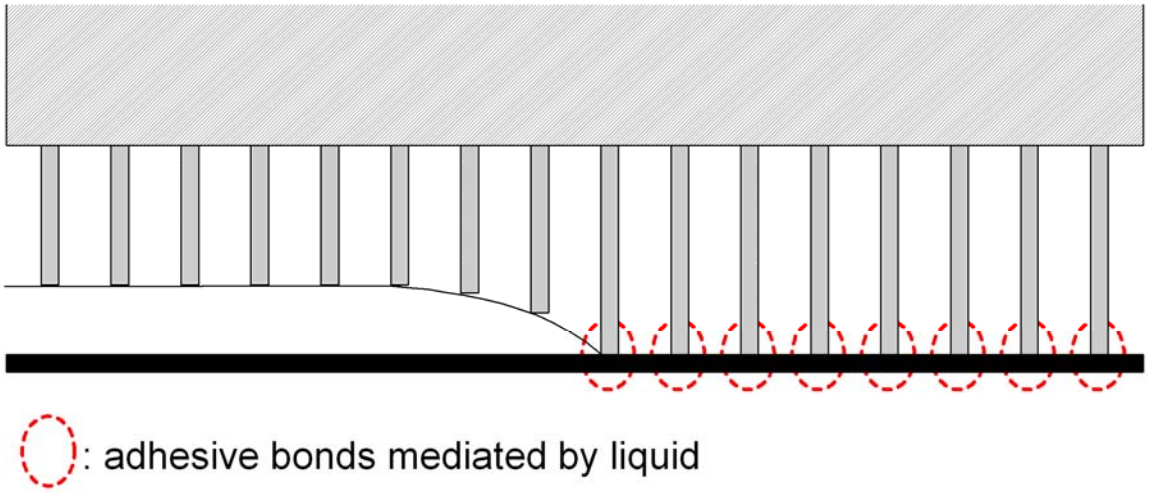

Figure 7.8: Schematic illustration of the detachment of a fiber array in wet adhesion with a substrate.

With the relations $d = \hat{D} \cdot R$, $\sigma = \hat{\eta} \cdot \gamma / R$, we have

$$G = \gamma \cdot \int \hat{\eta} \, \mathrm{d}\hat{D} \, . \tag{7.11}$$

The value of adhesion energy is exactly the area under the stress-separation curve multiplied by liquid surface tension γ. Self-similar systems with different R would have the same adhesion energy, i.e. adhesion energy does not have scaling effects. Figure 7.6b

shows the calculated values of adhesion energy for different liquid volumes when the contact angles are fixed at zero. The values are about 0.15 J/m^2. An interesting observation is that varying liquid volume also almost makes no difference to the adhesion energy.

7.6 Theoretical strength of wet adhesion

Recall that the total adhesion strength is composed of two components: the pressure difference inside and outside the liquid, and the axial component of surface tension acting along the liquid periphery on fiber tip. The portion contributed by pressure difference, denoted as $\left(P_{\text{out}} - P_{\text{in}}\right)$, is

$$P_{\text{out}} - P_{\text{in}} = \hat{\alpha} \cdot \sigma^{*}, \tag{7.12}$$

where $\alpha = \left(-\hat{H}\hat{X}_0^2\right) \Big/ \left(-\hat{H}\hat{X}_0^2 + 2\hat{X}_0 \sin\theta_1\right)$ referring to Equation (7.7). Thus, $\hat{\alpha}$ is determined once the liquid volume and contact angles are given. Substituting Equation (7.9) into (7.12), we get

$$P_{\text{in}} = P_{\text{out}} - \hat{\alpha} \cdot \hat{\eta}^{*} \cdot \frac{\gamma}{R}. \tag{7.13}$$

Here, P_{out} corresponds to the atmospheric pressure, which is about 0.1 MPa. We can readily see that reducing R may result in a negative pressure inside the liquid. It is known that a liquid subjected to negative pressure is metastable and cavitation failure occurs within the liquid as the negative pressure becomes large. The theory of tensile properties of liquids is well developed [88]. Homogenous nucleation theory has predicted that the cavitation is initiated by vapor bubbles produced spontaneously within the liquid.

However, experimental values of liquid tensile strength are smaller by one or two orders of magnitude than the predicted one, because homogenous nucleation is extremely rare and heterogeneous nucleation usually dominates in practice. Heterogeneous nucleation occurs due to pre-existing gas residues within the liquid or at the liquid/solid interface, and cavitation occurs when a critical negative pressure $P_{\text{cr}} = 2\gamma/a$ is reached, where γ is the liquid surface tension and a is the size of the gas residues. One can calculate that a bubble with radius of 100 nm has a critical negative pressure of 1.5 MPa.

Gas residues are unavoidable in wet adhesion due to liquid impurities and solid roughness, which leads to a theoretical negative pressure P_{th} that can be sustained by the liquid. The theoretical adhesion strength would be of the same order as P_{th}, according to Equation (7.12).

If the negative pressure exceeds P_{th}, the liquid itself would fail by cavitation. We see that there exists a critical length scale

$$R_{\text{cr}} = \hat{\alpha} \cdot \hat{\eta}^* \cdot \frac{\gamma}{P_{\text{out}} - P_{\text{th}}}, \tag{7.14}$$

which allows the pressure within the liquid to reach P_{th}. Below R_{cr}, the negative pressure cannot increase further since the liquid itself would fail. In Equation (7.14), both $\hat{\alpha}$ and $\hat{\eta}^*$ are functions of prescribed liquid volume and contact angles. For the sake of concreteness, we take $\hat{V} = 0.3$, $\theta_1 = \theta_2 = 0$, the values of $\hat{\alpha}$ and $\hat{\eta}^*$ are calculated to be 0.96 and 19.1, respectively. Substituting $\gamma = 0.073\,\text{N/m}$, $P_{\text{out}} = 0.1\,\text{MPa}$ and $P_{\text{th}} = -1.5\,\text{MPa}$ into Equation (7.14), we estimate R_{cr} to be about 0.8 μm. The value $P_{\text{th}} = -1.5\,\text{MPa}$ is selected because most experimental data measuring maximum negative

pressure in biological systems are of this order [89-91]. Therefore, we conclude that size reduction down to micron scale helps the wet adhesive system to achieve strength optimization.

7.7 Comparison with dry adhesion

We have investigated the adhesion strength and adhesion energy of wet adhesion. One may compare the results with those of dry adhesion. Previous study [67] has shown that size reduction to ~100 nm can help the system to achieve optimization of dry adhesion strength against shape induced stress singularity near the contact edge. For dry adhesion, the adhesion strength was estimated to be about 20 MPa based on van der Waals interaction.

In Section 7.6, we have estimated a value on the order of 1 MPa as the theoretical strength for wet adhesion. It is obvious that wet adhesion cannot compete with dry adhesion from the strength point of view. Also, wet adhesion also has the disadvantage of not being able to resist shear without dynamic slipping. On the other hand, wet adhesion can have a very long effective interaction range. The effective interaction range of dry adhesion is of the order of atomic scale, while that of wet adhesion is usually a fraction of fiber radius R, as indicated in Figures 7.3 and 7.6a. For example, if $R = 1\,\mu\text{m}$, the effective interaction range would be hundreds of nm. This long effective interaction range allows the wet adhesive systems to achieve considerable adhesion energy, as has been discussed in Section 7.5. Increasing liquid volume tends to increase the interaction range while decrease the adhesion strength. During pull-off, the strength of wet adhesion

may not be so strong, but the distance to break the bond can be very large. This behavior of liquid bridges is quite analogous to the concept of “long bonds, not strong bonds” proposed for thin elastic fibers adhering to a substrate [92].

Chapter 8

Concluding remarks

To understand the mechanics of focal contacts in cell-matrix adhesion, we have developed an idealized stochastic-elasticity model of two elastic bodies joining over adhesion clusters consisting of multiple molecular bonds. The model is aimed at a seamless unification of elastic descriptions of adhesive contact at large scale and statistical descriptions of single bond behavior at small scale. A series of Monte Carlo simulations have been conducted to investigate how the lifetime and strength of molecular bond clusters are influenced by adhesion size, bond rebinding rate, elastic stiffness of cell and substrate, as well as the loading direction. The main conclusions of the present work are summarized as following.

1) Coupled stochastic-elasticity equations have been used to model the stability and strength of molecular bond clusters joining two elastic bodies with spatially non-uniform bond traction and surface separation. A Monte Carlo based procedure has been employed to numerically solve the coupled stochastic-elasticity governing equations. In principle, the approach may be extended to other related problems such as leukocyte rolling and immunological synapse formation.

2) A dimensionless parameter, $\alpha = a\rho_{LR}k_{LR}\left(\left(1-\nu_C^2\right)/E_C + \left(1-\nu_S^2\right)/E_S\right)$ (for a single adhesion patch), has been identified as a controlling factor to determine how the interfacial traction is distributed within the adhesion domain. When α is small, the applied load is equally shared among the closed bonds and the cluster behavior is similar to those studied by Erdmann and Schwarz [20,21]. However, when α is large, a severe stress concentration occurs within the adhesion domain.

3) Our analysis shows that the reduced elastic modulus of the cell and substrate plays a critically important role in controlling the interfacial traction distribution and cluster stability. On very soft substrates, crack-like interfacial traction cannot be alleviated by cytoskeleton stiffening [27-29], which may prevent shortly lived focal complexes from maturing into stable FAs. On relatively stiff substrates, cells can actively control the cytoskeleton stiffness via their motor contractile machinery. In this case, cytoskeleton stiffening can alleviate stress concentration and allow the focal adhesions to achieve long-term stability. This is consistent with experimental observations that focal adhesions formed on stiff substrates are generally more stable than those on soft ones.

4) Adhesion size also plays an important role in controlling bond force distribution and cluster stability. Growing adhesion size ultimately leads to highly non-uniform interfacial traction, which tends to destabilize cluster adhesion via crack-like failure. Our analysis shows that the cluster lifetime is prolonged only within an optimal size window. The lower bound of the window is associated with the transition from a single-molecule-like behavior with finite lifetime to a statistically stable adhesion, while the upper bound is due to crack-like failure at large sizes.

5) We demonstrate the dependence of the adhesion lifetime and strength on the loading angle of applied tensile stress. Low-angle pulling dramatically increases the adhesion lifetime and strength. Therefore, cell spreading and flattening over a substrate result in low-angle pulling on FAs and benefit stable adhesion. This suggests a regulation mechanism by which cells can switch between long- and short-lived adhesions by adjusting pulling direction around a critical angle.

Some critical assumptions have been made in our model in mimicking focal contacts in cell-matrix adhesion. The present study on focal adhesions has been conducted from a mechanics point of view based on elasticity theory and stochastic binding/unbinding, while experiments are often focused on the biological roles of specific proteins in cell adhesion [93]. In our model, the cell is viewed as a compliant body with passive properties, and the active processes of the cytoskeleton that respond to either external forces or cellular contractility are neglected [57]. Moreover, we have limited ourselves to elastic systems in the sense that any bond association or dissociation is sensed instantly by the cell and substrate, while real biological cells could show much more complex nonlinear and viscoelastic constitutive behaviors. We have assumed immobile receptor-ligand bonds at the cell-substrate interface when discussing the lifetime and strength of molecular clusters. In reality, bond diffusion is likely to be important and should be incorporated in future research [94]. We have considered only a tensile load with all molecular bonds stretched in the same direction. In contrast, the loading conditions at focal adhesion sites can be much more complex. In spite of these limitations, it is encouraging that the predicted behaviors of such an idealized model are consistent with relevant experimental observations.

At the organism scale of biological adhesion, we have studied wet adhesion induced by a liquid bridge between a fiber and a solid surface, motivated by wet adhesive systems in biology. We have discussed the scaling effects of the fiber size for self-similar systems. The self-similarity is distinguished by two parameters: the liquid volume and the contact angles between liquid and solids. The following conclusions can be made:

6) An inverse scaling law of wet adhesion strength σ^* has been obtained for the self-similar fiber-liquid-substrate systems, $\sigma^* = \hat{\eta}^*\left(\hat{V}, \theta_1, \theta_2\right) \cdot \gamma / R$, where $\hat{\eta}^*$ is a numerical coefficient depending on the prescribed system parameters, γ is the liquid surface tension and R is the radius of the fiber.

7) It is always possible to maximize $\hat{\eta}^*$ by selecting appropriate liquid volume and small contact angles. The liquid volume maximizing $\hat{\eta}^*$ is associated with the undulation magnitude of solid roughness. Small contact angle on the fiber is helpful to achieve successful adhesion to both hydrophilic and hydrophobic surfaces.

8) Size reduction helps to enhance wet adhesion strength until it reaches the theoretical limit of spontaneous cavitation failure of a liquid under large negative pressure. There exists a critical length scale, below which the adhesion strength cannot be further improved since the liquid itself would fail. Reducing fiber size R down to this scale results in the optimal adhesion strength.

9) Wet adhesion by capillary interactions is relatively weak and cannot resist shear under static loading. On the other hand, wet adhesion is relatively long-ranged in contrast to dry adhesion. The long effective interaction range helps wet adhesive systems to achieve considerable adhesion energy.

Finally, we point out the critical assumptions made in this part of research. We have assumed that the liquid bridge meets the two solids at definitive contact angles and the liquid surface tension remains constant when the fiber radius varies. While it is known that these assumptions may fail when the droplet size is on the order of several nanometers [95-97], in our analysis the adhesion strength already saturates at the theoretical tensile strength of liquid when the characteristic size of the liquid bridge is on the order of a micrometer. We have adopted a liquid bridge model of pure wet adhesion. The solids are assumed rigid and there is no solid-solid contact occurring in the attachment. In contrast, the materials of biological attachment systems are usually quite flexible [98] and can elastically deform themselves to achieve large dry contact areas with the substrate. The existence of liquid is expected to promote this process. Further studies will be aimed at combined dry/wet adhesion models. Also, we have assumed quasi-static pull-off in calculating the adhesion strength and adhesion energy, ignoring the rate dependent factors such as fluid viscosity. In contrast, the secretions of insects are usually viscous [99]. Some insects even have more complex secretions that consist of two kinds of adhesive fluids with different chemical compositions [100]. The roles of such special designs in wet adhesion are of great interest.

Appendix A

Solving singular integral equations

Consider the integral equation governing the traction distribution within a single adhesion patch of molecular bonds,

$$\frac{\partial \sigma(x)}{\partial x} = \frac{2\alpha}{\pi} \int_{-1}^{1} \frac{\sigma(s)\mathrm{d}s}{x-s}, \quad |x| \le 1, \tag{A.1}$$

together with the condition of global force balance

$$\int_{-1}^{1} \sigma(s)\mathrm{d}s = 2. \tag{A.2}$$

The solution to the interfacial traction is either uniform or singular for limiting values of α. For intermediate range $0 < \alpha < \infty$, one has to solve the above equations numerically.

Assume that the solution can be represented by a polynomial as

$$\sigma(x) = \sum_{j=0}^{N} C_j x^j \ . \tag{A.3}$$

Equation (A.1) becomes

$$\frac{\partial \sigma(x)}{\partial x} = \sum_{j=1}^{N} C_j \cdot j x^{j-1} = \frac{2\alpha}{\pi} \sum_{j=0}^{N} C_j \int_{-1}^{1} \frac{s^j}{x-s}\mathrm{d}s \ . \tag{A.4}$$

Equation (A.2) becomes

$$\begin{aligned}&\sum_{i=0}^{N} C_i \int_{-1}^{1} s^i \mathrm{d}s = 2C_0 + \frac{2}{3}C_2 + \frac{2}{5}C_4 + \frac{2}{7}C_6 + \cdots = 2 \\ &\Rightarrow C_0 = 1 - \frac{1}{3}C_2 - \frac{1}{5}C_4 - \frac{1}{7}C_6 - \cdots\end{aligned} . \tag{A.5}$$

For a given point x_i within the adhesion domain, Equation (A.4) can be rearranged into

$$\sum_{j=1}^{N} C_j \left(j x_i^{j-1} - \frac{2\alpha}{\pi} \int_{-1}^{1} \frac{s^j}{x_i - s} \mathrm{d}s \right) - C_0 \frac{2\alpha}{\pi} \int_{-1}^{1} \frac{1}{x_i - s} \mathrm{d}s = 0 . \tag{A.6}$$

Combining Equations (A.5) and (A.6) gives

$$\begin{aligned}&\sum_{j=1}^{N} C_j \left(j x_i^{j-1} - \frac{2\alpha}{\pi} \int_{-1}^{1} \frac{s^j}{x_i - s} \mathrm{d}s \right) - \frac{2\alpha}{\pi} \int_{-1}^{1} \frac{1}{x_i - s} \mathrm{d}s \left(1 - \frac{1}{3}C_2 - \frac{1}{5}C_4 - \frac{1}{7}C_6 - \cdots \right) = 0 \\ &\Rightarrow \sum_{j=1}^{N} C_j \left(j x_i^{j-1} - \frac{2\alpha}{\pi} \int_{-1}^{1} \frac{s^j}{x_i - s} \mathrm{d}s \right) + \frac{2\alpha}{\pi} \int_{-1}^{1} \frac{1}{x_i - s} \mathrm{d}s \left(\frac{1}{3}C_2 + \frac{1}{5}C_4 + \frac{1}{7}C_6 + \cdots \right) = \frac{2\alpha}{\pi} \int_{-1}^{1} \frac{1}{x_i - s} \mathrm{d}s\end{aligned} . \tag{A.7}$$

To solve for N unknowns, $C_i \left(i = 1, 2, \cdots, N \right)$, one needs to pick up N different points within $[-1, 1]$. The collocation points x_i are chosen to be the zeros of the N^{th} Legendre polynomial of the second kind, $P_N(x)$, so that the singular integrals with Cauchy-type kernel in Equation (A.7) can be evaluated. For example,

$$\int_{-1}^{1} s^j \frac{1}{x_i - s} \mathrm{d}s = \sum_{k=1}^{N} w_k s_k^j \frac{1}{x_i - s_k} , \tag{A.8}$$

where s_k and w_k are the Gauss-Legendre integration points and the corresponding weights [101]. The last unknown C_0 can be obtained by Equation (A.5).

The singular integral equations of periodic adhesion clusters, Equations (3.14) and (3.16) in the main text, can be solved in a similar way.

Appendix B

Governing equations of periodic adhesion clusters

The general equation of a bi-material adhesion (or contact) problem is

$$\frac{\partial \Delta u_x}{\partial x} = \frac{2}{\pi}\frac{1}{E^*}\int_{-\infty}^{\infty}\frac{q(s)}{x-s}\mathrm{d}s + \frac{2D}{E^*}p(x), \tag{B.1a}$$

$$\frac{\partial \Delta u_z}{\partial x} = \frac{2}{\pi}\frac{1}{E^*}\int_{-\infty}^{\infty}\frac{p(s)}{x-s}\mathrm{d}s - \frac{2D}{E^*}q(x). \tag{B.1b}$$

Suppose that the load is applied far from the interface,

$$\tau(x) = q(x), \tag{B.2a}$$

$$\sigma(x) = p(x), \tag{B.2b}$$

where $\tau(x)$ and $\sigma(x)$ are the tangential and normal components of the traction within molecular bonds. Considering the compatibility condition at the interface

$$\frac{\partial \tau(x)}{\partial x} = \rho_{LR}k_{LR}\frac{\partial \Delta u_x}{\partial x}, \tag{B.3a}$$

$$\frac{\partial \sigma(x)}{\partial x} = \rho_{LR}k_{LR}\frac{\partial \Delta u_z}{\partial x}, \tag{B.3b}$$

one obtain

$$\frac{\partial \tau(x)}{\partial x} = \frac{\rho_{LR} k_{LR}}{E^*}\left(\frac{2}{\pi}\int_{-\infty}^{\infty}\frac{\tau(s)}{x-s}\mathrm{d}s + 2D\sigma(x)\right), \tag{B.4a}$$

$$\frac{\partial \sigma(x)}{\partial x} = \frac{\rho_{LR} k_{LR}}{E^*}\left(\frac{2}{\pi}\int_{-\infty}^{\infty}\frac{\sigma(s)}{x-s}\mathrm{d}s - 2D\tau(x)\right). \tag{B.4b}$$

If the bond tractions, $\tau(x)$ and $\sigma(x)$, are of size $2a$ and are periodically distributed at a period of $2c$ ($c > a$) along the interface,

$$\begin{aligned}\int_{-\infty}^{\infty}\frac{\sigma(s)}{x-s}\mathrm{d}s &= \sum_{n=-\infty}^{\infty}\int_{-a}^{a}\frac{\sigma(s)}{(x-2cn)-s}\mathrm{d}s \\ &= \int_{-a}^{a}\sigma(s)\sum_{n=-\infty}^{\infty}\frac{1}{(x-2cn)-s}\mathrm{d}s \\ &= \frac{1}{2c}\int_{-a}^{a}\sigma(s)\sum_{n=-\infty}^{\infty}\frac{1}{(x-s)/2c-n}\mathrm{d}s\end{aligned} \quad . \tag{B.5}$$

Now we need to evaluate the series $\sum_{n=-\infty}^{\infty}\frac{1}{(x-s)/2c-n}$. Let $X = (x-s)/2c$, one can show that

$$\sum_{n=-\infty}^{\infty}\frac{1}{(x-s)/2c-n} = \sum_{n=-\infty}^{\infty}\frac{1}{X-n} = \pi\cot(\pi X). \tag{B.6}$$

Proof:

$$\sin(\pi X) = C\prod_{n=-\infty}^{\infty}(X-n)$$

$$\log(\sin(\pi X)) = \log C + \sum_{n=-\infty}^{\infty}\log(X-n)$$

$$\pi\frac{\cos(\pi X)}{\sin(\pi X)} = \pi\cot(\pi X) = \sum_{n=-\infty}^{\infty}\frac{1}{X-n}$$

Therefore, the governing equation becomes

$$\frac{\partial \tau(x)}{\partial x} = \frac{\rho_{LR} k_{LR}}{E^*}\left(\frac{1}{c}\int_{-a}^{a} \tau(s)\cot\left(\frac{\pi(x-s)}{2c}\right)\mathrm{d}s + 2D\sigma(x)\right), \tag{B.7a}$$

$$\frac{\partial \sigma(x)}{\partial x} = \frac{\rho_{LR} k_{LR}}{E^*}\left(\frac{1}{c}\int_{-a}^{a} \sigma(s)\cot\left(\frac{\pi(x-s)}{2c}\right)\mathrm{d}s - 2D\tau(x)\right). \tag{B.7b}$$

We normalize the coordinate x by a,

$$\frac{\partial \tau(\hat{x})}{\partial \hat{x}} = \frac{\rho_{LR} k_{LR} a}{E^*}\left(\frac{1}{\hat{c}}\int_{-1}^{1} \tau(\hat{s})\cot\left(\frac{\pi(\hat{x}-\hat{s})}{2\hat{c}}\right)\mathrm{d}\hat{s} + 2D\sigma(\hat{x})\right), \tag{B.8a}$$

$$\frac{\partial \sigma(\hat{x})}{\partial \hat{x}} = \frac{\rho_{LR} k_{LR} a}{E^*}\left(\frac{1}{\hat{c}}\int_{-1}^{1} \sigma(\hat{s})\cot\left(\frac{\pi(\hat{x}-\hat{s})}{2\hat{c}}\right)\mathrm{d}\hat{s} - 2D\tau(\hat{x})\right), \tag{B.8b}$$

where $\hat{c} = c/a$. Taking $D = 0$ leads to

$$\frac{\partial \tau(\hat{x})}{\partial \hat{x}} = \overline{\alpha}\int_{-1}^{1} \tau(\hat{s})\cot\left(\frac{\pi(\hat{x}-\hat{s})}{2\hat{c}}\right)\mathrm{d}\hat{s}, \tag{B.9a}$$

$$\frac{\partial \sigma(\hat{x})}{\partial \hat{x}} = \overline{\alpha}\int_{-1}^{1} \sigma(\hat{s})\cot\left(\frac{\pi(\hat{x}-\hat{s})}{2\hat{c}}\right)\mathrm{d}\hat{s}, \tag{B.9b}$$

where

$$\overline{\alpha} = a\overline{\rho}_{LR} k_{LR}\left(\frac{1-\nu_C^2}{E_C} + \frac{1-\nu_S^2}{E_S}\right). \tag{B.10}$$

Here $\overline{\rho}_{LR}$ is the apparent bond density of the interface defined by the relation $c\overline{\rho}_{LR} = a\rho_{LR}$.

Bibliography

[1] Chen X, Gumbiner BM. Crosstalk between different adhesion molecules. Curr. Opin. Cell Biol. 2006;18:572.

[2] Alberts B, Johnson A, Lewis J, Raff M, Roberts K, Walter P. Molecular Biology of the Cell. New York: Garland Science, 2002.

[3] Bershadsky AD, Balaban NQ, Geiger B. Adhesion-dependent cell mechanosensitivity. Annu. Rev. Cell Dev. Biol. 2003;19:677.

[4] Bell GI. Models for specific adhesion of cells to cells. Science 1978;200:618.

[5] Evans EA. Detailed mechanics of membrane-membrane adhesion and separation .1. Continuum of molecular cross-bridges. Biophys. J. 1985;48:175.

[6] Dembo M, Torney DC, Saxman K, Hammer D. The reaction-limited kinetics of membrane-to-surface adhesion and detachment. Proc. R. Soc. Lond. Ser. B-Biol. Sci. 1988;234:55.

[7] Freund LB, Lin Y. The role of binder mobility in spontaneous adhesive contact and implications for cell adhesion. J. Mech. Phys. Solids 2004;52:2455.

[8] Shenoy VB, Freund LB. Growth and shape stabillity of a biological membrane adhesion complex in the diffusion-mediated regime. Proc. Natl. Acad. Sci. U. S. A. 2005;102:3213.

[9] Gao HJ, Shi WD, Freund LB. Mechanics of receptor-mediated endocytosis. Proc. Natl. Acad. Sci. U. S. A. 2005;102:9469.

[10] Zaidel-Bar R, Ballestrem C, Kam Z, Geiger B. Early molecular events in the assembly of matrix adhesions at the leading edge of migrating cells. J. Cell Sci. 2003;116:4605.

[11] Leckband D, Israelachvili J. Intermolecular forces in biology. Q. Rev. Biophys. 2001;34:105.

[12] Florin EL, Moy VT, Gaub HE. Adhesion forces between individual ligand-receptor pairs. Science 1994;264:415.

[13] Alon R, Hammer DA, Springer TA. Lifetime of the P-selectin-carbohydrate bond and its response to tensile force in hydrodynamic flow. Nature 1995;374:539.

[14] Merkel R, Nassoy P, Leung A, Ritchie K, Evans E. Energy landscapes of receptor-ligand bonds explored with dynamic force spectroscopy. Nature 1999;397:50.

[15] Evans E, Ritchie K. Dynamic strength of molecular adhesion bonds. Biophys. J. 1997;72:1541.

[16] Freund LB. Characterizing the resistance generated by a molecular bond as it is forcibly separated. Proc. Natl. Acad. Sci. U. S. A. 2009;106:8818.

[17] Evans E. Probing the relation between force - Lifetime - and chemistry in single molecular bonds. Annu. Rev. Biophys. Biomolec. Struct. 2001;30:105.

[18] Evans EA, Calderwood DA. Forces and bond dynamics in cell adhesion. Science 2007;316:1148.

[19] Seifert U. Rupture of multiple parallel molecular bonds under dynamic loading. Phys. Rev. Lett. 2000;84:2750.

[20] Erdmann T, Schwarz US. Stability of adhesion clusters under constant force. Phys. Rev. Lett. 2004;92:4.

[21] Erdmann T, Schwarz US. Stochastic dynamics of adhesion clusters under shared constant force and with rebinding. J. Chem. Phys. 2004;121:8997.

[22] Zamir E, Katz M, Posen Y, Erez N, Yamada KM, Katz BZ, Lin S, Lin DC, Bershadsky A, Kam Z, Geiger B. Dynamics and segregation of cell-matrix adhesions in cultured fibroblasts. Nat. Cell Biol. 2000;2:191.

[23] Zaidel-Bar R, Cohen M, Addadi L, Geiger B. Hierarchical assembly of cell-matrix adhesion complexes. Portland Press, 2004. p.416.

[24] Lin Y, Freund LB. Optimum size of a molecular bond cluster in adhesion. Phys. Rev. E 2008;78:6.

[25] Pelham RJ, Wang YL. Cell locomotion and focal adhesions are regulated by substrate flexibility. Proc. Natl. Acad. Sci. U. S. A. 1997;94:13661.

[26] Lo CM, Wang HB, Dembo M, Wang YL. Cell movement is guided by the rigidity of the substrate. Biophys. J. 2000;79:144.

[27] Discher DE, Janmey P, Wang YL. Tissue cells feel and respond to the stiffness of their substrate. Science 2005;310:1139.

[28] Gardel ML, Shin JH, MacKintosh FC, Mahadevan L, Matsudaira P, Weitz DA. Elastic Behavior of cross-linked and bundled actin networks. Science 2004;304:1301.

[29] Storm C, Pastore JJ, MacKintosh FC, Lubensky TC, Janmey PA. Nonlinear elasticity in biological gels. Nature 2005;435:191.

[30] Totsukawa G, Wu Y, Sasaki Y, Hartshorne DJ, Yamakita Y, Yamashiro S, Matsumura F. Distinct roles of MLCK and ROCK in the regulation of membrane protrusions and focal adhesion dynamics during cell migration of fibroblasts. J. Cell Biol. 2004;164:427.

[31] Bershadsky A, Kozlov M, Geiger B. Adhesion-mediated mechanosensitivity: a time to experiment, and a time to theorize. Curr. Opin. Cell Biol. 2006;18:472.

[32] Riveline D, Zamir E, Balaban NQ, Schwarz US, Ishizaki T, Narumiya S, Kam Z, Geiger B, Bershadsky AD. Focal contacts as mechanosensors: Externally applied local mechanical force induces growth of focal contacts by an mDia1-dependent and ROCK-independent mechanism. J. Cell Biol. 2001;153:1175.

[33] Balaban NQ, Schwarz US, Riveline D, Goichberg P, Tzur G, Sabanay I, Mahalu D, Safran S, Bershadsky A, Addadi L, Geiger B. Force and focal adhesion assembly: a close relationship studied using elastic micropatterned substrates. Nat. Cell Biol. 2001;3:466.

[34] Chang KC, Tees DFJ, Hammer DA. The state diagram for cell adhesion under flow: Leukocyte rolling and firm adhesion. Proc. Natl. Acad. Sci. U. S. A. 2000;97:11262.

[35] Schwarz US, Alon R. L-selectin-mediated leukocyte tethering in shear flow is controlled by multiple contacts and cytoskeletal anchorage facilitating fast rebinding events. Proc. Natl. Acad. Sci. U. S. A. 2004;101:6940.

[36] Qi SY, Groves JT, Chakraborty AK. Synaptic pattern formation during cellular recognition. Proc. Natl. Acad. Sci. U. S. A. 2001;98:6548.

[37] Weikl TR, Lipowsky R. Pattern formation during T-cell adhesion. Biophys. J. 2004;87:3665.

[38] Hanggi P, Talkner P, Borkovec M. Reaction-rate theory - 50 years after Kramers. Rev. Mod. Phys. 1990;62:251.

[39] Erdmann T, Schwarz US. Bistability of cell-matrix adhesions resulting from nonlinear receptor-ligand dynamics. Biophys. J. 2006;91:L60.

[40] Erdmann T, Schwarz US. Impact of receptor-ligand distance on adhesion cluster stability. Eur. Phys. J. E 2007;22:123.

[41] Qian J, Wang J, Gao H. Lifetime and strength of adhesive molecular bond clusters between elastic media. Langmuir 2008;24:1262.

[42] van Kampen NG. Stochastic Processes in Physics and Chemistry. Amsterdam: Elsevier Science, 1992.

[43] Goel NS, Richter-Dyn N. Stochastic Models in Biology. New York: Academic Press, 1974.

[44] Johnson KL. Contact Mechanics. Cambridge: Cambridge University Press, 1985.

[45] Dundurs J. Mathematical Theory of Dislocations. New York: American Society of Mechanical Engineers, 1969.

[46] Hutchinson JW, Suo Z. Mixed-mode cracking in layered materials. Advances in Applied Mechanics, Vol 29, vol. 29. San Diego: Academic Press Inc, 1992. p.63.

[47] Tada H, Paris PC, Irwin GR. The Stress Analysis of Cracks Handbook. New York: American Society of Mechanical Engineers, 2000.

[48] Arnold M, Cavalcanti-Adam EA, Glass R, Blummel J, Eck W, Kantlehner M, Kessler H, Spatz JP. Activation of integrin function by nanopatterned adhesive interfaces. ChemPhysChem 2004;5:383.

[49] Gao HJ, Chen SH. Flaw tolerance in a thin strip under tension. J. Appl. Mech.-Trans. ASME 2005;72:732.

[50] Gillespie DT. General method for numerically simulating stochastic time evolution of coupled chemical-reactions. J. Comput. Phys. 1976;22:403.

[51] Gillespie DT. Exact stochastic simulation of coupled chemical-reactions. J. Phys. Chem. 1977;81:2340.

[52] Long M, Goldsmith HL, Tees DFJ, Zhu C. Probabilistic modeling of shear-induced formation and breakage of doublets cross-linked by receptor-ligand bonds. Biophys. J. 1999;76:1112.

[53] Tees DFJ, Coenen O, Goldsmith HL. Interaction forces between red-cells agglutinated by antibody. 4. Time and force dependence of break-up. Biophys. J. 1993;65:1318.

[54] Tijms H. Understanding Probability: Chance Rules in Everyday Life. Cambridge: Cambridge University Press, 2004.

[55] Zuckerman DM, Bruinsma RF. Vesicle-vesicle adhesion by mobile lock-and-key molecules: Debye-Huckel theory and Monte Carlo simulation. Phys. Rev. E 1998;57:964.

[56] Rice JR. In: Liebowitz H, editor. Fracture: an Advanced Treatise. New York: Academic Press, 1968. p.191.

[57] Deshpande VS, McMeeking RM, Evans AG. A bio-chemo-mechanical model for cell contractility. Proc. Natl. Acad. Sci. U. S. A. 2006;103:14015.

[58] Bruinsma R. Theory of force regulation by Nascent adhesion sites. Biophys. J. 2005;89:87.

[59] Smith AS, Sengupta K, Goennenwein S, Seifert U, Sackmann E. Force-induced growth of adhesion domains is controlled by receptor mobility. Proc. Natl. Acad. Sci. U. S. A. 2008;105:6906.

[60] Qian J, Wang J, Gao H. Tension-induced growth of focal adhesions at cell-substrate interface. The Proceedings of IUTAM Symposium on Cellular, Molecular and Tissue Mechanics, in press.

[61] Stork NE. Experimental analysis of adhesion of Chrysolina Polita (Chrysomelidae: Coleoptera) on a variety of surfaces. The Journal of Experimental Biology 1980;88:91.

[62] Walker G. Adhesion to smooth surfaces by insects – a review. Int J Adhesion and Adhesives 1993;13(1):3.

[63] Autumn K et al. Evidence for van der Waals adhesion in gecko setae. Proc Natl Acad Sci USA 2002;99(19):12252.

[64] Kesel AB, Martin A, Seidl T. Adhesion measurements on the attachment devices of the jumping spider Evarcha arcuata. The Journal of Experimental Biology 2003;206:2733.

[65] Arzt E, Gorb S, Spolenak R. From micro to nano contacts in biological attachment devices. Proc Natl Acad Sci USA 2003;100(19):10603.

[66] Gao H, Ji B, Jaeger IL, Arzt E, Fratzl P. Materials become insensitive to flaws at nanoscale: Lessons from nature. Proc Natl Acad Sci USA 2003;100(10):5597.

[67] Gao H, Yao H. Shape insensitive optimal adhesion of nanoscale fibrillar structures. Proc Natl Acad Sci USA 2004;101(21):7851.

[68] Gao H, Ji B, Buehler MJ, Yao H. Flaw tolerant bulk and surface nanostructures of biological systems. Mechanics and Chemistry of Biosystems 2004;1(1):37.

[69] Gao H, Wang X, Yao H, Gorb S, Arzt E. Mechanics of hierarchical adhesion structures of geckos. Mechanics of Materials 2005;37:275.

[70] Yao HM, Gao HJ. Mechanical principles of robust and releasable adhesion of gecko. J. Adhes. Sci. Technol. 2007;21:1185.

[71] Eisner T, Aneshansley DJ. Defense by foot adhesion in a beetle (Hemisphaerota cyanea). Proc Natl Acad Sci USA 2000;97(12):6568.

[72] Jiao Y, Gorb S, Scherge M. Adhesion measured on the attachment pads of Tettigonia Viridissima (Orthoptera, Insecta). The Journal of Experimental Biology 2000;203:1887.

[73] Federle W, Baumgartner W, Hölldobler B. Biomechanics of ant adhesive pads: Frictional forces are rate- and temperature-dependent. The Journal of Experimental Biology 2004;206:67.

[74] Lees AD, Hardie J. The organs of adhesion in the aphid Megoura Viciae. The Journal of Experimental Biology 1988;136:209.

[75] Walker G, Yule AB, Ratcliffe J. The adhesive organ of the blowfly, Calliphora vomitoria: A functional approach (Diptera: Calliphoridae). J Zool Lond 1985;205:297.

[76] Emerson SB, Diehl D. Toe pad morphology and mechanisms of sticking in frogs. Biological Journal of the Linnean Society 1980;13:199.

[77] Ba-Omar TA, Downie JR, Barnes WJP. Development of adhesive toe-pads in the tree-frog (Phyllomedusa trinitatis). J Zool Lond 2000;250:267.

[78] Gorb S. The design of the fly adhesive pad: Distal tenent setae are adapted to the delivery of an adhesive secretion. Proc R Soc Lond B 1998;265:747.

[79] Dixon AFG, Croghan PC, Gowing RP. The mechanism by which aphids adhere to smooth surfaces. The Journal of Experimental Biology 1990;152:243.

[80] Qian J, Gao HJ. Scaling effects of wet adhesion in biological attachment systems. Acta Biomater. 2006;2:51.

[81] Orr FM, Scriven LE, Rivas AP. Pendular rings between solids: Meniscus properties and capillary force. Journal of Fluid Mechanics 1975;67:723.

[82] Obata KJ, Motokada T, Saito S, Takahashi K. A scheme for micro-manipulation based on capillary force. Journal of Fluid Mechanics 2004;498:113.

[83] Fortes MA. Axisymmetric liquid bridges between parallel plates. Journal of Colloid and Interface Science 1982;88(2):338.

[84] Adamson AW. Physical Chemistry of Surfaces. John Wiley & Sons Inc, 1976.

[85] Paddy JF, Petre G, Rusu CG, Gamero J, Wozniak G. The shape, stability and breakage of pendant liquid bridges. Journal of Fluid Mechanics 1997;352:177.

[86] Zilberman S, Persson BNJ. Adhesion between elastic bodies with rough surfaces. Solid State Communications 2002;123(3-4):173.

[87] Rabinovich YI, Adler JJ, Esayanur MS, Ata A, Singh RK, Moudgil BM. Capillary forces between surfaces with nanoscale roughness. Advances in Colloid and Interface Science 2002;96:213.

[88] Steudle E. The cohesion-tension mechanism and the acquisition of water by plant roots. Annu Rev Plant Physiol Plant Mol Biol 2001;52:847.

[89] Holbrook NM, Burns MJ, Field CB. Negative xylem pressures in plants: A test of the balancing pressure technique. Science 1995;270:1193.

[90] Koch GW, Sillett SC, Jennings GM, Davis SD. The limits to tree height. Nature 2004;428:851.

[91] Smith AM. Cephalopod sucker design and the physical limits to negative pressure. The Journal of Experimental Biology 1996;199:949.

[92] Persson BNJ. On the mechanism of adhesion in biological systems. Journal of Chemical Physics 2003;118(16):7614.

[93] Small JV, Geiger B, Kaverina I, Bershadsky A. How do microtubules guide migrating cells? Nat. Rev. Mol. Cell Biol. 2002;3:957.

[94] Wang JZ, Gao HJ. Clustering instability in adhesive contact between elastic solids via diffusive molecular bonds. J. Mech. Phys. Solids 2008;56:251.

[95] de Gennes PG. Wetting: Statics and dynamics. Review of Modern Physics 1985;57(3):827.

[96] Johnson AE. Analysis of the Young equation and use of the Kelvin equation in calculating the Gibbs excess. Colloids and Surfaces A 2002;202:33.

[97] Digilov R. Kelvin equation for meniscuses of nanosize dimensions. Langmuir 2000;16:1424.

[98] Niederegger S, Gorb S, Jiao Y. Contact behavior of tenent setae in attachment pads of the blowfly Calliphora vicina (Diptera, Calliphoridae). J Comp Physiol A 2002;187:961.

[99] Vötsch W, Nicholson G, Müller R, Stierhof YD, Gorb S, Schwarz U. Chemical composition of the attachment pad secretion of the locust Locusta migratoria. Insect Biochemistry and Molecular Biology 2002;32:1605.

[100] Federle W, Riehle M, Curtis ASG, Full RJ. An integrative study of insect adhesion: Mechanics and wet adhesion of pretarsal pads in ants. Integr Comp Biol 2002;42:1100.

[101] Erdogan F, Gupta GD, Cook TS. Numerical solution of singular integral equations. In: Sih GC, editor. Mechanics of Fracture. Noordhoff, 1973. p.368.